IMPEDANCE SPECTROSCOPY: THE INFLUENCE OF SURFACE HETEROGENEITY AND APPLICATION TO CORROSION MONITORING OF BRIDGE TENDONS

By

CHRISTOPHER L. ALEXANDER

A DISSERTATION PRESENTED TO THE GRADUATE SCHOOL
OF THE UNIVERSITY OF FLORIDA IN PARTIAL FULFILLMENT
OF THE REQUIREMENTS FOR THE DEGREE OF
DOCTOR OF PHILOSOPHY

UNIVERSITY OF FLORIDA

2017

ACKNOWLEDGMENTS

I gratefully acknowledge financial support from the Florida Department of Transportation (Contract BDV31-977-35, Ronald Simmons, technical monitor). The opinions and findings in this dissertation are those of the author and not necessarily those of the funding agency. I would like to thank my adviser, Mark Orazem for his continued mentorship and support. I would also like to thank Bernard Tribollet and Vincent Vivier for their assistance as well as my research group for their support and guidance.

TABLE OF CONTENTS

page

CHAPTER

LIST OF TABLES

LIST OF FIGURES

LIST OF SYMBOLS

Roman

A	adsorption impedance parameter, $\Omega^{-1}s^{-1}cm^{-2}$
B	adsorption impedance parameter, s^{-1}
C	capacitance, F/cm^2 or F (1F = 1C/V)
C_{dl}	double-layer capacitance, F/cm^2 or F (1F = 1C/V)
c_{i}	volumetric concentration of species i, mol/cm^3
f	frequency, $f = \omega/2\pi$, Hz
F	Faraday's constant, 96,487 C/equiv
f_r	roughness factor, true surface area/geometric area
$\imath_0$	exchange current density, mA/cm^2
i_{F}	faradaic current density, mA/cm^2
K	dimensionless frequency associated with a disk electrode
L	inductance, H ($1H$ = 1Vs^2/C)
l_c	characteristic length, cm
P	period of a square-wave radial distribution
ϕ	electrolyte potential, V
Q	CPE coefficient , $s^{\alpha}/\Omega cm^2$
R	resistance, Ωcm^2 or Ω (1Ω = 1Vs/C)
r	radial coordinate , cm
r_0	radius of a disk electrode , $s^{\alpha}/\Omega cm^2$
R	universal gas constant, 8.3143 J/mol K
R_{e}	ohmic resistance, Ωcm^2 or Ω (1Ω = 1Vs/C)
R_{p}	polarization resistance, Ωcm^2 or Ω (1Ω = 1Vs/C)
R_{t}	charge-transfer resistance, Ωcm^2 or Ω (1Ω = 1Vs/C)
T	temperature, K
V	perturbation potential, V

Z	global impedance, Ωcm^2
z	local impedance, Ωcm^2
Z_0	global interfacial impedance, Ωcm^2
Z_{ads}	adsorption impedance, Ωcm^2
Z_{e}	global ohmic impedance, Ωcm^2
Z_{F}	faradaic impedance, Ωcm^2

Greek

α	exponential parameter for a CPE
Γ	maximum surface coverage, mol/cm^2
γ	surface coverage, mol/cm^2
κ	conductivity, S/cm
φ	phase angle, degree
ρ	resistivity, Ωcm
ω	angular frequency, rad/s

General Notation

$\text{Im}\{X\}$	imaginary part of X
$\text{Re}\{X\}$	real part of X
$\overline{X}$	steady-state or time-averaged part of $X(t)$
$\overline{z}$	complex conjugate of a complex number z, $\bar{z} = z_r - z_j$ of $X(t)$
$\langle X \rangle$	surface-averaged value of X
$\tilde{X}$	oscillating part of $X(t)$

Subscripts

a	pertaining to anodic reactions
c	pertaining to cathodic reactions
j	imaginary
r	real

Abstract of Dissertation Presented to the Graduate School
of the University of Florida in Partial Fulfillment of the
Requirements for the Degree of Doctor of Philosophy

IMPEDANCE SPECTROSCOPY: THE INFLUENCE OF SURFACE HETEROGENEITY AND APPLICATION TO CORROSION MONITORING OF BRIDGE TENDONS

By

Christopher L. Alexander

May 2017

Chair: Mark E. Orazem
Major: Chemical Engineering

An indirect impedance technique is proposed as a way to detect corrosion within external post-tensioned bridge tendons. Non-destructive techniques are needed to determine the integrity of the steel without having to break open the tendon. The indirect impedance aims to extract the impedance of the steel-grout interface from the impedance measured at the surface of the grout. However, the electrode configuration required for the indirect impedance measurement yields geometry-induced frequency dispersion. Therefore, the biggest obstacle in the application of this technique is the lack of a reliable way of interpreting the data. Bench-top experiments were performed on fabricated tendons with and without induced corrosion to show that the indirect impedance was sensitive to the properties of the steel and grout interface. Finite-element models were used to simulate the indirect impedance and determine how the geometry of the unusual electrode configuration influences the impedance.

Frequency dispersion may also be a result of surface heterogeneity of the electrode. The influence of surface heterogeneity on impedance measurements was explored to determine if surface distributions could provide a physical explanation for frequency dispersion observed experimentally as Constant Phase Elements(CPE). Finite-element models were used to simulate the impedance response of electrodes with surface roughness, a distribution of capacitance, and a distribution of reactivity. Similar to the geometry

induced frequency dispersion observed for a disk electrode, surface roughness and a distribution of capacitance caused frequency dispersion at high frequencies and could be defined in terms of a characteristic length. As the characteristic length decreases, the frequency dispersion shifts to higher frequencies. The characteristic length for surface roughness was based on the period and the roughness factor. The characteristic length for a distribution of capacitance was the period of the distribution. A distribution of reactivity associated with a single step reaction did not cause frequency dispersion; however, when a two step reaction coupled by an adsorbed intermediate was considered, frequency dispersion occurred at both low and high frequencies.

CHAPTER 1
INTRODUCTION

Electrochemical impedance spectroscopy (EIS) is an experimental characterization method that may be used to assess the physical processes that occur at the interface of an electrode and an electrolyte. While measuring the impedance of an electrochemical system is relatively trivial, interpreting the results can be complicated by the presence of frequency dispersion. Frequency dispersion is sometimes an unavoidable aspect of impedance measurements and has multiple contributing factors such as geometry, surface heterogeneity, homogeneous reactions, as well as anomalous diffusion processes.

Work presented in this dissertation is focused on 2 projects. In the first part, EIS was used to establish a way of detecting corrosion in external post-tensioned bridge tendons which are used in segmentally constructed bridges. One of the major applications of EIS is to determine the polarization resistance of a metal liquid interface which is inversely related to the corrosion rate. EIS has been applied to assess the corrosive state of steel within concrete. Deterioration of Americas infrastructure has cost billions of dollars a year to mitigate. 11 percent of the nations bridges have been deemed structurally deficient while another 13 percent are functionally obsolete. Corrosion of steel within bridges has been one of the major contributing factors. Post tensioned tendons consist of helically wound 7-wire pre-stressing steel strands that are surrounded by a cementitious grout contained within a High Density Polyethylene (HDPE) duct. The grout provides an alkaline environment to prevent the steel from corroding, and the duct prevents the intrusion of aggressive contaminants. Despite these preventative measures, there have been many cases in which corrosion has still occurred. The current method of ensuring that the steel contained within tendons is not corroding is to cut through the tendon and visually inspect the steel. A nondestructive alternative is to use an indirect impedance measurement to assess the properties of steel contained within the grout without a direct connection to the steel. By measuring the impedance using an array of 4 electrodes on the surface of the grout, the properties of the steel may be sampled. However, extracting the true impedance of the steel from the impedance of the whole system is difficult. The major obstacle to commercialization of this technique is determining a way to account for the frequency dispersion caused by the geometry of the measurement.

In the second part, work was done to establish an understanding of what factors contribute to frequency dispersion in EIS measurements and to uncover the physical origin of the constant-phase element (CPE).This dissertation addresses frequency dispersion due to geometry as well as surface heterogeneity. Jorcin et al. used local impedance spectroscopy to show that frequency dispersion can arise from surface or normal distributions of time constants. The frequency dispersion associated with a distribution of time constants normal to the electrode surface is well established; whereas, the frequency dispersion associated with a surface distribution is not well understood. Hirschorn et al.[24, 25] showed that a power–law distribution of resistivity through a film yields CPE behavior. The power–law–model approach has been used successfully to extract a film capacitance and associated parameters for a variety of systems, including oxides on steel,[58] human skin,[58, 74] and polymer coatings.[48, 52]

In terms of surface distributions, Brug et al. [12] developed an expression for the capacitance extracted from a CPE caused by a surface distribution of capacitance. Córdoba-Torres et al. [15] showed that the Brug model explained the correlation observed between CPE parameters α and Q for two experimental conditions: the corrosion of polycrystalline iron and the deposition of $CaCO_3$ scale on gold electrodes. The results were attributed to a distribution of time constants associated with surface heterogeneity. The exact nature of the surface heterogeneity was not identified. In subsequent work, Córdoba-Torres et al. [16] suggested that the CPE behavior results from energetic distributions rather than geometric heterogeneity or roughness.

In this dissertation, a brief history and review of electrochemical impedance spectroscopy will be presented in Chapter 2 along with a description of how frequency dispersion can complicate data interpretation. Background knowledge on external post-tensioned tendons and corrosion mechanisms of steel in concrete will be presented in Chapter 3. A proof of concept for an indirect impedance spectroscopy method to detect corrosion in post-tensioned bridge tendons will be presented in Chapter 4. An experimental proof of concept for indirect impedance measurements will be presented in Chapter 5. Experimental results of field applications of the indirect impedance technique will be presented in Chapter 6. The influence of surface roughness, a distribution of capacitance, and a distribution of charge-transfer resistance will be presented in Chapters 7, 8, and 9 respectively. Wu et al. showed that the geometry of a disk electrode embedded within an insulating plane with reactions involving adsorbed intermediates causes frequency dispersion at low frequencies. Chapter 10 will present the influence of heterogeneous reactions rates associated with reactions coupled by an adsorbed intermediate. Conclusions of this work are provided in Chapter 11. Suggestions for future work will be presented in Chapter 12.

CHAPTER 2
ELECTROCHEMICAL IMPEDANCE SPECTROSCOPY

Electrochemical impedance spectroscopy is a powerful experimental technique that may be used to study interfacial phenomena such as charging, electrochemical reactions, and diffusion processes. The interface is interrogated with an application of a sinusoidal perturbation of either potential or current as is shown in Figure 2-1 The input signal shown is a potential perturbation as a function of time. The perturbation may be imposed in addition to a steady state value of potential $\overline{V}$ which allows the modulation of potential at different points along the polarization curve. The response is monitored usually with the use of a reference electrode to help reduce the ohmic effect and isolate the impedance of the working electrode electrolyte interface. If the input signal is potential then the response will be current. The magnitude of the time-domain response signal will always be less than the magnitude of the input signal indicating the resistive properties of the interface and if there are any capacitive features the response signal will lag the input signal by a time of Δt. The magnitude of the impedance is calculated as the ratio of the magnitude of the input and the output signals and the phase is calculated as $2\pi\Delta t/T$, where T represents the period of the input signal. The real and imaginary parts of the impedance are functions of the phase and magnitude expressed as

$$Z_r = |Z(\omega)|\cos(\varphi) \tag{2–1}$$

and

$$Z_j = |Z(\omega)|\sin(\varphi) \tag{2–2}$$

respectively and the total complex impedance is the sum of the two parts.

2.1 Graphical Representation

The impedance is measured over a range of frequencies and is traditionally plotted in Nyquist or Bode format. An example of the impedance of a resistor and capacitor in parallel is shown in Figure 2-2 in Nyquist format. The Nyquist format displays the

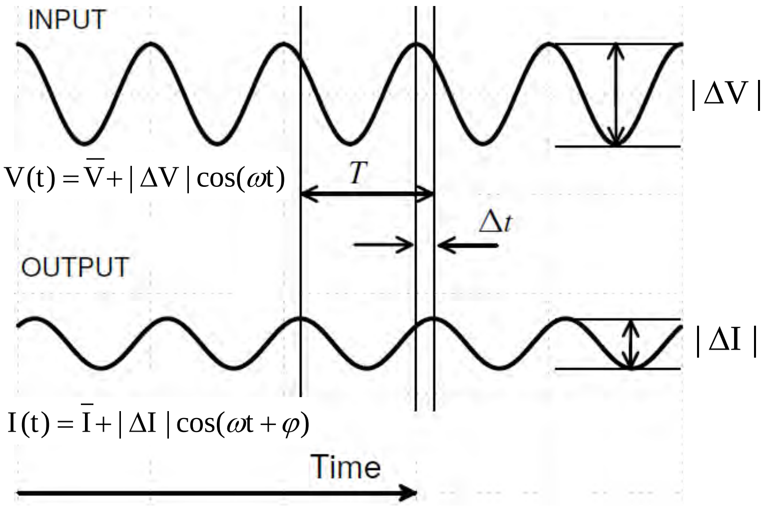

Figure 2-1. Schematic representation of the calculation of the transfer function for a sinusoidal input at frequency ω. The time lag between the two signals is Δt and the period of the signals is T.[57]

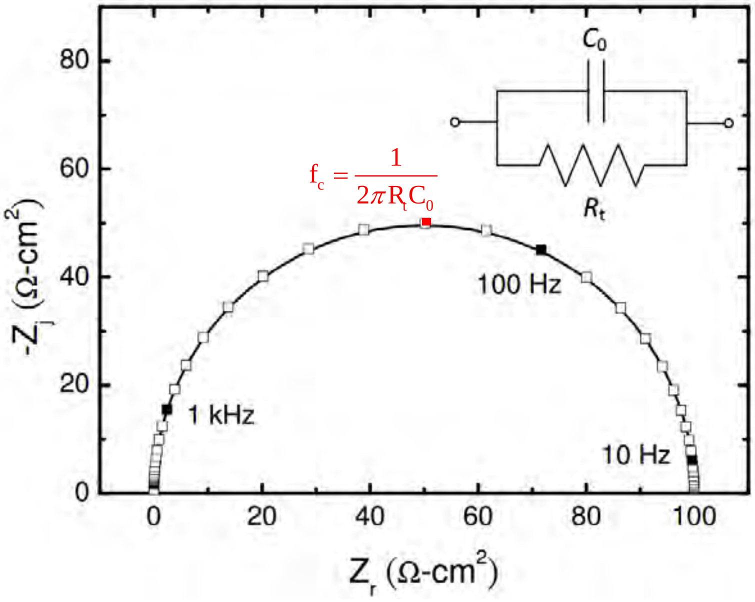

Figure 2-2. Impedance of a resistor and capacitor in parallel in Nyquist format.[57]

negative of the imaginary part of the impedance as a function of the real part. The real part of the impedance is normally associated with resistive properties of the system and the imaginary part is representative of inductive or capacitive features. For this circuit, the low frequency limit of the impedance is equal to the resistance R_t. The capacitance may be determined from the characteristic frequency which is located at the peak of the semi-circle. One of the disadvantages of the Nyquist representation is that some features may be lost at high frequencies.

The Bode format displays the phase and the magnitude of the impedance each as a function of the logarithm of the frequency which has the advantage of showing the frequency dependence of the system. The phase may be calculated from the real and imaginary parts of the impedance as $\tan^{-1}(Z_j/Z_r)$. However, in cases where there is a large ohmic resistance, the Bode representation is misconceiving at higher frequencies. An ohmic resistance corrected phase angle may be calculated as $\varphi_{adj} = \tan^{-1}(Z_j/(Z_r - R_e))$ which provides a more accurate representation of the system.

2.2 Analysis & Interpretation

Information obtained from impedance measurements may include, but, is not limited to the interfacial capacitance, kinetic parameters associated with electrochemical reactions across the interface, as well as diffusion parameters. The Kramers-Kronig relations are often used to test for consistency between the real and imaginary parts to ensure the conditions of linearity, stability, and causality were adhered to. Equivalent circuits incorporating elements such as resistors, capacitors, and diffusion elements are often used to fit the results and extract physically meaningful parameters. There are often multiple equivalent circuits that may fit the data which complicates the interpretation. An alternative is to fit the impedance with a mathematical model which accounts for the expected physics of the system under study.

2.3 Frequency Dispersion

In most cases, the impedance data can not be fit using a circuit composed of frequency-independent parameters such as resistors and capacitors due to the presence of frequency dispersion. Constant-phase elements (CPE) are often used in place of capacitors to account for the frequency dispersion. The earliest account of the constant-phase element was presented by Hugo Fricke in 1932.[22] Under the assumption that the capacitance was frequency dependent, he realized that the capacitance could be expressed as a function of the frequency raised to a power such that $C = f(\omega^{-\alpha})$. The impedance of a CPE may be expressed as

$$Z_{CPE} = \frac{1}{(j\omega)^{\alpha} Q} \tag{2–3}$$

where when $\alpha = 1$, Q represents the interfacial capacitance, and when $\alpha < 1$ the physical meaning of Q is not clear. However, many physical sources of frequency dispersion have been identified in electrochemical systems including cell geometry, normal distributions of resistivity, diffusion of species, and porous electrodes. Other proposed sources of frequency dispersion include surface heterogeneity and the coupling of charging and faradaic currents. The background for the influence of geometry, a normal distribution of time constants, and surface heterogeneity on impedance measurements is presented below.

2.3.1 Geometry Effect

The electrochemical impedance may be considered to be composed of two parts including an interfacial component and an ohmic component. The interfacial impedance is associated with the kinetic and charging properties of the interface and the ohmic component is representative of the electrolyte conductivity. In an electrochemical cell in which the current distribution is uniform across the electrode surface, the solution resistance is in series to the interfacial impedance such that the interfacial impedance may be determined simply by subtracting out the ohmic resistance. However, in cases where the current distribution is nonuniform across the electrode surface, frequency dispersion occurs making the separation of the ohmic effect and the interfacial impedance much more complicated.

For a disk electrode embedded within an insulating plane with the counter electrode located infinitely far away from the working electrode, the ohmic resistance may be expressed as $R = 1/4\kappa r_0$.[50] A dimensionless frequency based on the radius of the disk, r_0, as well as the ratio of the electrolyte conductivity and the double layer capacitance, C_0/κ, may be expressed as

$$K = \frac{\omega C_0 r_0}{\kappa} \tag{2–4}$$

such that frequency dispersion is induced at $K \geq 1$. The characteristic frequency associated with the frequency dispersion is then

$$f_c = \frac{\kappa}{2\pi C_0 r_0} \tag{2–5}$$

where as the radius of the disk increases the frequency dispersion occurs in a lower frequency range.

Newman accounted for the frequency dispersion caused by the geometry of the disk electrode by expressing the impedance as $R_{\text{e,eff}} + \frac{1}{j\omega C_{0,\text{eff}}}$ in which $R_{\text{e,eff}}$ and $C_{0,\text{eff}}$ were frequency dependent terms. Huang et al. used finite element models to simulate the impedance of a blocking disk electrode and showed that the ohmic contribution is actually a complex term with real and imaginary parts in which the overall impedance may be expressed as $Z = Z_{\text{e}} + Z_0$. At frequencies below $K = 1$, Z_{e} behaves as a pure resistor. As the geometry-induced frequency dispersion appears only at high frequencies,[28] the influence of geometry cannot provide an explanation for CPE behavior that may extend over many decades of frequency for blocking electrodes. One physical explanation for a complex ohmic impedance is the radial component of the local current density becoming a function of the radial location. For instance, the local current density on a disk electrode has a radial component which is dependent on the radial position and also decreases with axial position.[10] A recessed electrode, which has a uniform local current density does not have a radial component and therefore the ohmic contribution to the impedance is a pure resistance.

2.3.2 Normal Distribution

Some metals, when placed in alkaline media, form a protective oxide layer several nanometers in thickness which prevents corrosion of the underlying metal. The passive layer varies in resistivity in the direction normal to the electrode surface with the most resistive region being closest to the electrode. Hirschorn et al.[24, 25] showed that a power law distribution of resistivity normal to the surface of an electrode causes constant-phase element behavior over a broad range of frequencies. A mathematical expression was formulated which allows the estimation of the film thickness form the parameters of the CPE and also relates the parameters of the CPE to an effective capacitance.

2.3.3 Surface Heterogeneity

In early experiments on solid electrodes, micro–scale surface roughness was believed to contribute to frequency dispersion in electrochemical measurements. [19] Borisova and Ershler were the first to observe that roughness influenced electrochemical measurements.[11] They found that the extent of frequency dispersion was reduced by melting a metal electrode and letting it cool to form into a droplet, suggesting that the smoother surface led to a more ideal response.

Following the development of fractal theory,[43] there was an attempt to correlate the fractal dimensions of the surface to the CPE exponent α.[45, 55] Fractal geometry was shown to cause frequency dispersion, however a correlation between the fractal dimension and variance from ideality could not be found. Kant et al. [31, 36, 37, 38, 70] used a formalism described in reference [32] to describe the influence of fractal roughness on impedance response, but their mathematical approach did not provide information on the frequency dispersion associated with CPE behavior. Similarly, the Debye-Falkenhagen treatment of the electrical double layer by Singh and Kant revealed only low-frequency influence of roughness on impedance response.[67] Pajkossy showed experimentally that annealing can reduce the degree of frequency dispersion, even though the roughness of the surface remained the same, and thereby concluded that the frequency dispersion cannot be due to the geometric effect solely but may also have a contribution of atomic–scale heterogeneities.[60] Jänsch et al. [29] used experiments on three gold electrodes with different surface structure and roughness to show that CPE behavior could not be attributed to electrode roughness. Emmanuel used an analytic–continuation method to calculate the impedance of a 2D Hull cell and simulated the effect of a linear distribution of solution resistance assuming a uniform capacitance.[20] The results of his work showed that frequency dispersion occurred at high frequencies while the calculations yielded ideal behavior at low frequencies.

Another proposed cause of frequency dispersion is the surface distribution of capacitance [41]. Brug et al. developed a formula which relates the parameters of the CPE to an effective double layer capacitance [12]. They postulated that the distribution was due to a variation in capacitance across the electrode surface. In 1978, Leek and Hampson [41] calculated the frequency dispersion using a circuit element ladder with different capacitance values per surface area of electrode. They concluded that surface heterogeneity was an important factor contributing to frequency dispersion. In 1992, Pajkossy and Nyikos [61] used a self-similar capacitance distribution to show that frequency dispersion in the form of constant–phase–element behavior cannot be explained by a capacitance distribution since the CPE behavior is only observed for physically impossible variations in capacitance. Also in 1992, Kurtkya and de Levie [39] conducted numerical simulations to explain that the frequency dispersion due to nonuniform capacitance is caused by the shift of the current lines with frequency from locations of high impedance to locations of low impedance.

While much has been done to determine the factors contributing to frequency dispersion in impedance measurements, there is still a lack of understanding of the physical significance of constant phase element behavior over a large range of frequencies when a surface film is not present. The most current proposed explanation is a surface distribution of time constants. To either confirm or reject this hypothesis, finite element simulations were performed on disk electrodes incorporating various forms of surface heterogeneity. The results are presented in later chapters for the influence of roughness, a distribution of capacitance, as well as a distribution of reactivity. The influence of coupled charging and faradaic currents will also be explored.

CHAPTER 3
CORROSION PROBLEMS IN EXTERNAL BRIDGE TENDONS

Bridge tendons incorporating high strength steel strands are used in segmental bridge construction to link concrete segments together which form the bridge span. Corrosion of the steel within the tendons poses a major threat to the structural integrity of a bridge. A brief description of segmental bridge construction is presented as well as background on post-tensioning.

3.1 Precast Segmentally Constructed Bridges

Precast segmental bridges are constructed by connecting precast concrete members to form the span of the bridge between piers or columns which hold the span up. The term precast means that the concrete segments are built prior to being set in place. The segments act as puzzle pieces which greatly expedites the construction time. The segments are fastened together with the use of longitudinal post-tensioned tendons. Two classifications of tendons may be used, including external and internal tendons. Internal tendons are placed within the concrete segments through holes which are pre-formed into the concrete segments. External tendons are usually placed within the inner openings of the segments but are external to the concrete. The tendons consist of multiple 7-wire pre-stressing strands contained within a High-density Polyethylene (HDPE) duct. They run continuously through deviator blocks which help form the profile of the tendon. The tendons may either be bonded or unbonded meaning grout is used to fill the space between the duct and the steel (bonded) or is left empty (unbonded). The tendons are called post-tensioned because after they are in place the steel within the tendon is pulled into tension using a high strength jack shown. Stretching the steel strands forces the concrete segments into compression. Concrete is a brittle material that cracks under tension but can withstand large compressive forces without any structural damage. Therefore, steel reinforcement is used to withstand any tensile forces the structure may experience. However, for the tensile load to be transferred to the steel under normal or unstressed reinforcment, the concrete has to crack first. By stressing the steel within the tendons and forcing the concrete into compression, the tensile forces are transferred to the steel prior to the concrete cracking which greatly improves the durability of the bridge and allows for longer bridge spans. The ends of the tendons are anchored down at bulkheads and stressed after which the duct is filled with cementitious grout.[75] The alkaline grout is intended to provide protection against corrosion but, due to, possible voids in the grout and areas of improper mixing, cases of severe corrosion have occurred.

3.2 Corrosion Issues in Post-tensioning Systems

Despite the use of grout to prevent corrosion, there have been many cases in which corrosion has still occurred. Some of the causes of corrosion within post-tensioned tendons include voids in the grout, grout bleed water, cracks in the duct, and grout segregation. Voids in the grout can be caused by the adsorption of bleed water and grout segregation is usually caused by improper grout mixing procedures (Rafols 2013).

Since post-tensioning technology is still relatively new, these problems were not evident until the 1980s. The first instance occurred in 1980 when the southern outer roof of the Berlin Congress Hall collapsed 23 years after it was constructed.[1] Soon thereafter, two bridges were found with similar serious corrosion issues – the Taf Fawr Bridge on A470 in Wales, England and the Angel Road Bridge on the A406 North Circular in London, England.[64] Ultimately, the Taf Fawr Bridge was demolished in 1986 while the Angel Road Bridge was significantly retrofitted in 1982. In 1985, the single-span segmental post-tensioned Ynys-y-Gwas Bridge in Wales collapsed as a result of corrosion of longitudinal tendons at its segmented joints. This structure was only 32 years old, and there had been no previous indication of distress prior to collapse.[76] In 1992, the British Department of Transportation conducted a study on these corrosion issues and concluded that there was no method that could guarantee complete corrosion prevention. Later that year, post-tensioned bridges were effectively banned in the United Kingdom.[42]

The United Kingdom was not the only country with post-tensioned bridge issues. The post-tensioned Melle Bridge, which was built in Belgium in 1956, collapsed in 1992. In this instance, the bridge had been inspected, load tested, re-waterproofed, declared adequate, and just restored to service two years prior to its collapse.[1] More recently, the Saint Stefano Bridge in Italy[65] and the Lowes Motor Speedway footbridge in North Carolina[13] collapsed due to similar corrosion-related failures.

Corrosion in post-tensioned bridges is a major concern in Florida as well. The first reported post-tensioned corrosion issue was at the 18-year old Niles Channel Bridge in the Keys.[66],[2] Similar issues were reported at the 7-year old Mid Bay Bridge in the Western Panhandle [17], [75] and the 15-year old Sunshine Skyway Bridge in Tampa.[2] A number of studies were commissioned by the Florida Department of Transportation (FDOT) to address these issues. An important conclusion from the study related to the Mid Bay Bridge was that a non-destructive technique for testing corrosion and corrosion-risk in these post-tensioned members was required.

3.3 Methods of Corrosion Detection in Bridge Tendons

In 2006, FDOT and researchers at the University of Florida tried to develop a non–destructive technique for corrosion detection in post-tensioned members.[46] The study hinged on finding air-voids and/or entrained water in the grout matrix because these variables have been shown to lead to corrosion. A number of methods were used in this study including ground penetrating radar, impact echo, ultrasonic sound waves, and gamma-ray spectroscopy.

Results from this study indicate that, of these methods, only gamma-ray spectroscopy showed any real promise as a possible solution. However, spectroscopy results were preliminary (at best), and were based only on a limited number of laboratory-prepared samples. Furthermore, field-implementation of such a system appeared to be unlikely since it hinged upon using an HPGe detector which required liquid nitrogen (at 77K; -196oC;

-321oF). While investigators from the previous study recommended designing a better gamma-ray detector, specifics about exactly how this was to be done were never addressed.

The Federal Highway Administration identified main magnetic flux as a possible nondestructive method for external tendons which is still in need of development [23]. High powered magnets are used to induce a static magnetic field in the tendon and the magnetic flux, which is a function of steel cross-sectional area is monitored to detect fractures [72]. Ultrasonic tomography has been used to detect voids within the internal tendons by sending ultrasound waves and measuring the time for them to be transmitted. Differences in the density of media lead to longer transmission times.[44] While these methods are useful in identifying problem areas, only electrochemical techniques such as impedance spectroscopy can yield actual corrosion rates.

In application to reinforced concrete, many methods have been developed to estimate the corrosion rate of the embedded steel. The most notable of these techniques is the Linear Polarization Resistance (LPR) method in which a small over-potential is applied to the reinforcing steel and the current response is monitored. The polarization resistance of the steel is estimated by dividing the potential by the current response. With the relationship,

$$i_{corr} = B/A * R_{\mathrm{p}} \tag{3–1}$$

developed by Stern and Geary the steel polarization resistance, R_p, is used to estimate the corrosion rate based on the Tafel slope, B. However, the inherent assumption is that the corrosion reaction follows Tafel kinetics. Also, the LPR method requires a connection to the steel to polarize it but in reinforced structures access to the steel can only be provided by cutting through the concrete.

To avoid this, research has been done to develop a way to indirectly polarize the steel without an electrical connection. An indirect method has been explored in which an electric field is applied to the surface of the concrete and the induced current pulse indirectly polarizes the steel.[8] An alternative to the pulse method is electrochemical

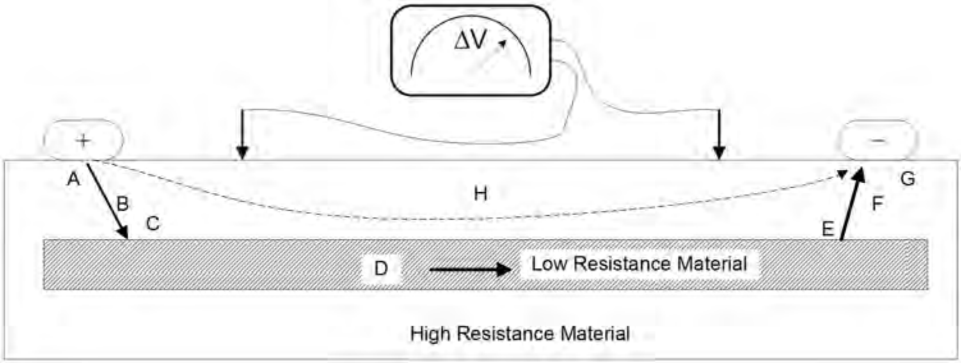

Figure 3-1. Schematic representation showing the current paths for a highly conductive strand embedded in a more resistive material. A) interfacial impedance at the positive electrode; B) ohmic resistance and dielectric response of the resistive material between the positive electrode and the strand; C) interfacial impedance at the surface of the strand; D) ohmic resistance of the strand; E) interfacial impedance at the surface of the strand; F) ohmic resistance and dielectric response of the resistive material between the negative electrode and the strand; and G) interfacial impedance at the negative electrode. The letter H signifies the ohmic resistance or dielectric response of the resistive material between the positive and negative electrodes.

impedance spectroscopy, which uses a sinusoidal current or potential perturbation applied to the concrete surface at a range of frequencies to indirectly polarize the steel. [33, 47] Monteiro et al. [47] reported using indirect impedance spectroscopy to determine the location and the condition of steel rebar within concrete slabs. They were able to qualitatively determine that the measured surface impedance was a function of the corrosion state of the steel as well as the resistance of the concrete.[47]

3.4 Indirect Impedance Spectroscopy

The indirect impedance technique requires a 4 electrode array consisting of a working and counter electrode (outer two electrodes of the array) and two reference electrodes(inner two electrodes of the array). A schematic representation of the indirect impedance measurement is shown in Figure 3-1 An ac perturbation is applied between the working and counter electrodes and the reference electrodes measure the potential response. The current follows the path of least resistance between the working and counter electrodeḊepending on the geometry of the specimen and the frequency of the perturbation, a certain fraction of the current will go solely through the grout while the rest will enter the steel. Therefore the steel is indirectly polarized due to the ac perturbation at the surface. The electrical impedance measured between the positive and negative contacts is influenced by the interfacial impedance at the positive electrode (A); the resistivity of the material between the positive electrode and the strand (B); the interfacial impedance at the surface of the strand (C and E); the ohmic resistance of the strand (D); the resistivity of the material between the positive electrode and the strand (F); and the interfacial impedance at the negative electrode (G). The current that flows only through the resistive material will be influenced by the resistivity of the material between the positive and negative electrodes (H). Use of a four-electrode configuration for potential measurement (indicated in Figure 3-1 by arrows connected to a voltmeter) eliminates the influence of the interfacial impedances at the positive and negative electrodes. The four-point probe configuration causes the impedance response to reflect the condition of the grout and the strand without the confounding influence of the current injection points.

One of the complications in the application of the indirect impedance technique to post-tensioned tendons is the difficulty in extracting the impedance of the steel and grout interface. An equation to estimate the polarization resistance of the steel from the resistance of the electrolyte and the resistance of the cell measured with the steel present was proposed. The equation was derived based on the assumption that the current ran parallel to the steel. Andrade et al. [7, 9] used results of finite element models to propose an analogue circuit that accounts for the polarization behavior of the steel and the properties of the mortar in which the steel is embedded. They determined that since a portion of the current goes through the concrete in parallel to the steel and another portion travels through the grout and then enters the steel, the concrete resistance has both a parallel and series component. However, they were not able to determine the exact circuit to fully describe the indirect method. Keddam et al.[33]

showed that at low frequencies (i.e., the d.c. limit) the current flows parallel to the steel; whereas, at high frequencies, the current enters the steel perpendicularly. They found that the zero-frequency limit of the impedance scaled by the resistivity of the grout is a function of the polarization resistance, similarly scaled by the resistivity of the grout. This relationship is independent of the grout resistivity for a defined geometry and electrode configuration.

The disadvantage of using equivalent circuits is the inability to account for the effects of nonuniform current distribution and ill-defined geometries. Huang et al.[28] showed that the impedance of a disk electrode is influenced by the geometry of the disk at high frequencies. The ohmic contribution to the impedance becomes complex at high frequencies due to the nonuniform current distribution. Therefore the use of equivalent circuits to fit the impedance of disk electrodes is only valid below a characteristic frequency dependent on the radius of the disk. The nonuniform current distribution of an indirect impedance measurement may cause similar issues.

The objective of our research is to use indirect impedance to monitor the integrity of the steel as well as the grout. To do this, the appropriate electrode configurations and spacing per tendon geometry will need to be determined. Also, the appropriate electrode materials and contact schemes to the grout as well as the appropriate frequency range and perturbation mode to use will need to be determined. The other major objective is to develop a means of interpreting the indirect impedance response and determine from that measurement if the steel is corroding.

CHAPTER 4
PROOF OF CONCEPT FOR CORROSION DETECTION USING INDIRECT IMPEDANCE

A proof of concept was established for using indirect impedance spectroscopy to detect the existence of corrosion in post-tensioned tendons. This development was supported by a combination of bench-top experiments performed on disk electrodes in grout and synthetic tendons. This work showed that indirect impedance can be used to observe differences in the impedance and differentiate between active and passive steel. Sensitivity to localized corrosion was found to be greatest when a current injection electrode is positioned directly above the corroding metal.

4.1 Conventional 3-electrode Configuration

Conventional impedance experiments were conducted with a disk electrode embedded in grout to determine the impedance behavior of the steel within the environment of the grout. The impedance was analyzed with mathematical models which include physical parameters to describe the behavior of the steel and grout interface.

One of the necessary parameters needed to develop a reliable interpretation technique of the indirect impedance is the impedance of the steel and grout interface in locations of passive and actively corroding steel. Cells configured with 3 electrodes were made of small plastic cylinders containing grout as the electrolyte and the impedance was measured across the steel and grout interface. A 3-in rod of steel was cut from the king wire of the steel strand and was inserted into the grout as shown in Figure 4-1. Heat shrink tubing and duct-tape was used to insulate the sides of the steel rod such that only the cross section of the rod was exposed to the grout in the form of a disk electrode within an insulating plane. A stainless–steel wire mesh was used as the counter electrode and a solid Ag–AgCl electrode was used as the reference.

Four cells were made and two of them were forced to corrode. A schematic of the impressed current technique is presented in Figure 4-2. A constant 20-V potential was applied between the steel rod and the stainless steel mesh for 1 week. The impedance was

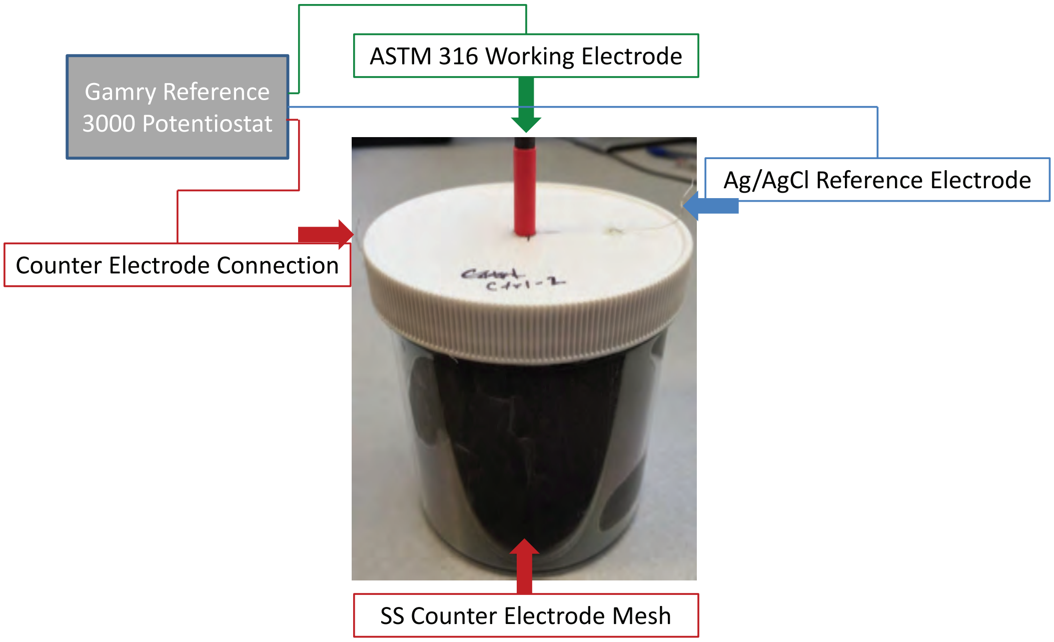

Figure 4-1. Schematic showing the conventional 3–electrode impedance measurement on a cylindrical electrochemical cell in which the electrolyte is grout and the working electrode is a coupon of the steel strand.

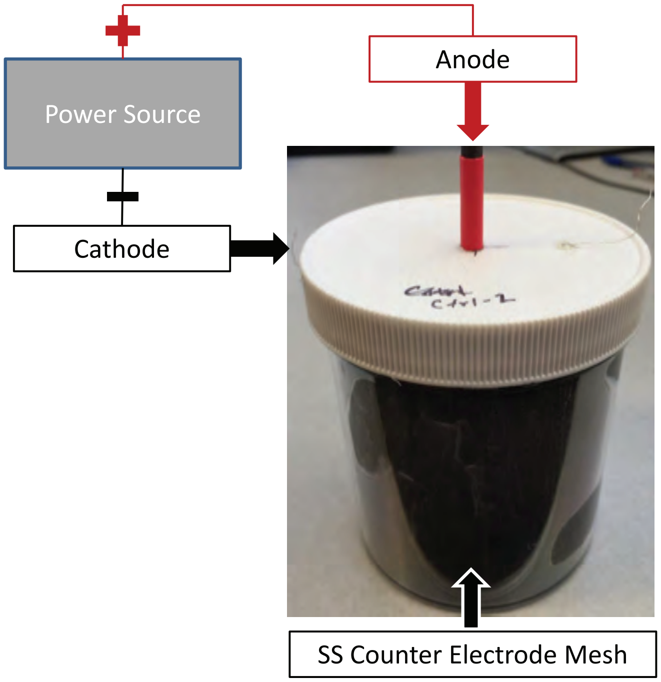

Figure 4-2. Schematic showing the impressed current technique for a cylindrical electrochemical cell in which the electrolyte is grout and the working electrode is a coupon of the steel strand.

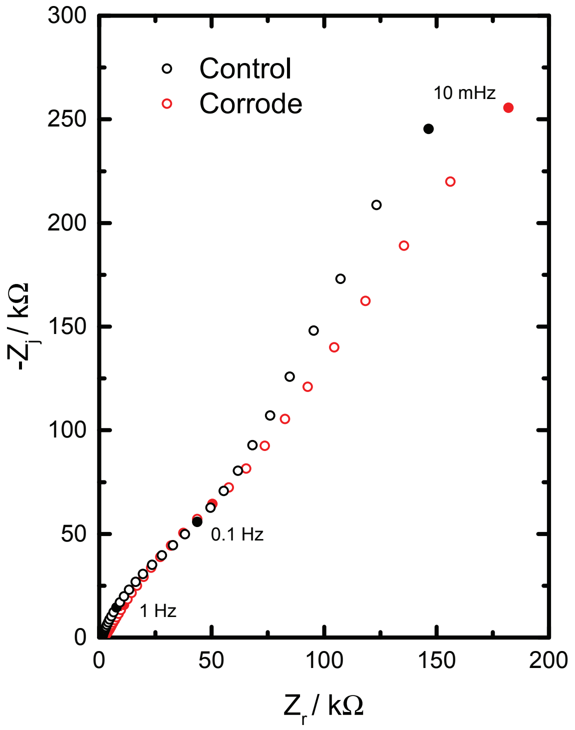

Figure 4-3. Conventional 3–electrode impedance of a steel disk electrode in grout before one of the specimens (corroded) was forced to corrode.

measured before and after the application of the impressed current. The impedance results of two of the specimens are presented in Figure 4-3 in which one is labeled as the control and the other is the to-be-corroded specimen. The results should be representative of the impedance of the steel and grout interface. The impedance was measured at frequencies between 500 Hz and 10 mHz. At high frequencies there is a depressed capacitive arc followed by a straight line at an angle at lower frequencies. The-high frequency behavior in both cases is almost identical while the slope of the impedance is slightly larger for the control specimen.

The impedance of a corroding specimen is compared to the control case in Figure 4-4. After forcing one of the specimens to corrode, the impedance decreased drastically. The ohmic resistance of the corroded specimen increased which can be explained by the reduction of water that occurs due to the cathodic reaction which increases the resistivity. The impedance of the control specimen did not change significantly. The figure inset

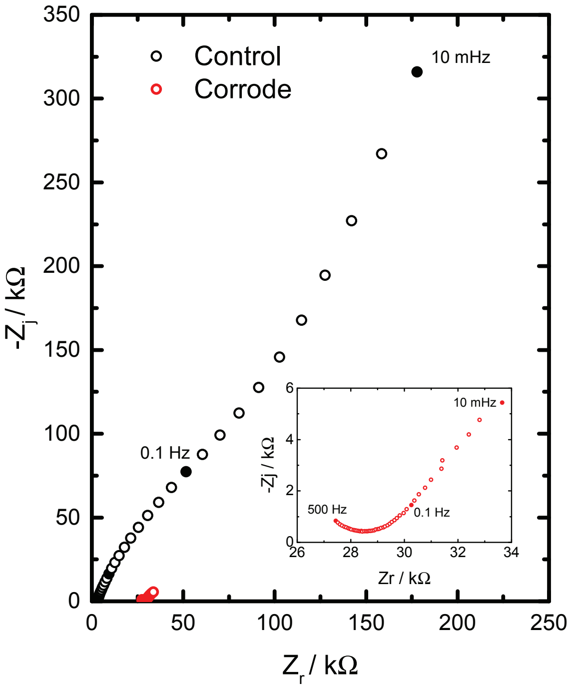

Figure 4-4. Conventional 3–electrode impedance of a steel disk electrode in grout after one of the specimens (corroded) was forced to corrode.

shows a magnified view of the corroded specimen impedance which contains a high frequency tail and a small capacitive arc at lower frequencies. The magnitude of the impedance decreased by a factor of 50 after forcing corrosion.

The steel rods from the control and corroded specimens were removed to view the steel surface. Images of the steel surface are presented in Figure 4-5. The control case, Figure 4-5A, has a shiny surface and areas of residual grout which have adhered to the surface. The corroded case shown in Figure 4-5B has reddish-brown corrosion product similar to what was observed on the steel removed from the tendons after the induced corrosion. In this case the corrosion is much more uniform and advanced.

4.2 Regression Fit

An equivalent circuit model was developed to fit the impedance results of the 3-electrode measurements to build an understanding of the impedance of the steel and grout interface. The equivalent circuit is based upon a physical model of the interface which is presented in Figure 4-6. We have assumed the interface comprises a porous film

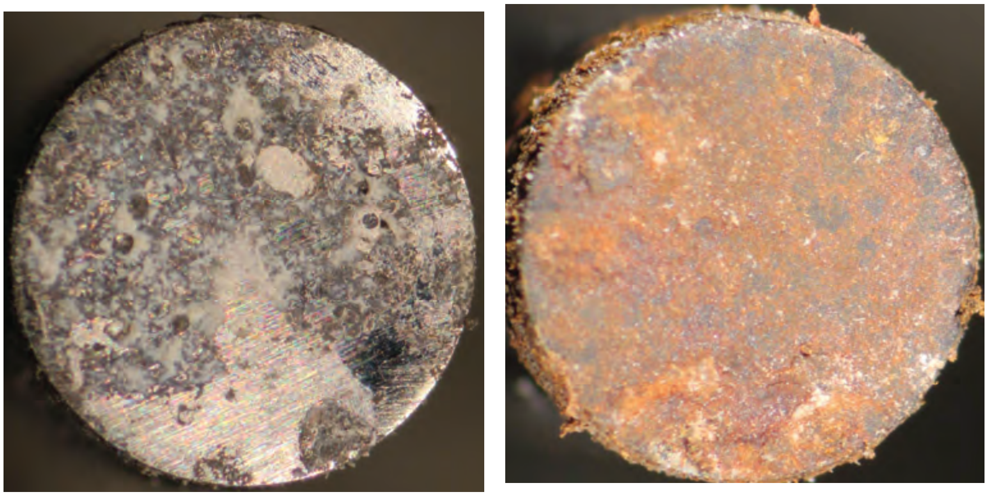

A

B

Figure 4-5. Images of the steel disk electrode extracted from the grout: a)Passive case b)Corroded case.

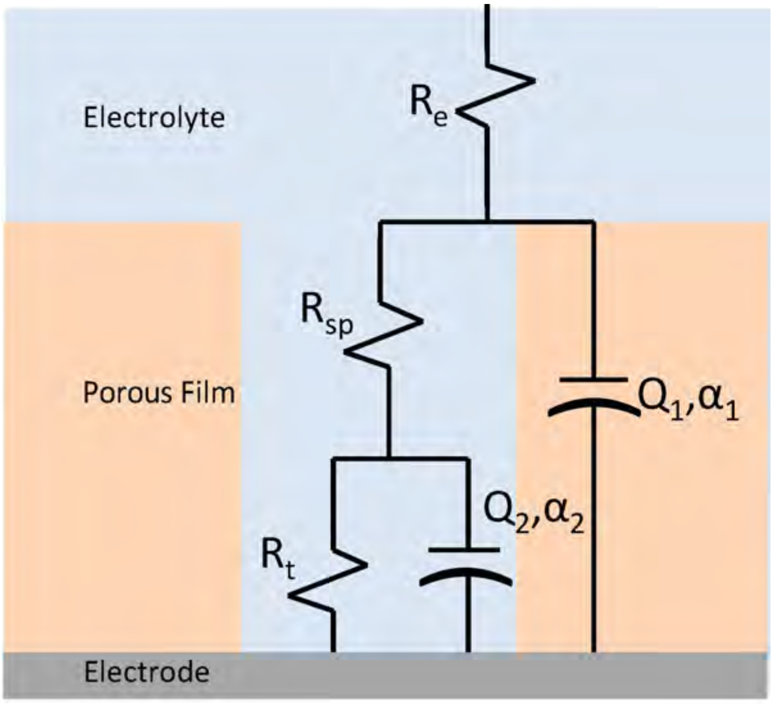

Figure 4-6. Circuit diagram used to fit the passive case impedance of the steel and grout interface.

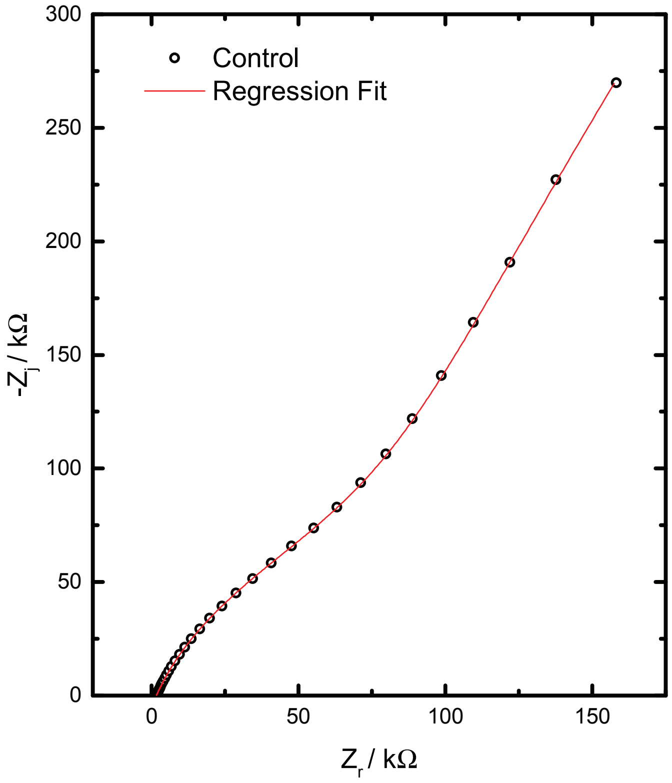

Figure 4-7. Impedance of the passive steel disk electrode in grout fitted with the circuit in Figure 4-6.

due to an uneven oxide layer. The resistance to current flow through the pore is described by R_{sp} and the impedance of the interface between the solution and the bare metal is described as a resistor and constant–phase element in parallel with parameters R_t, Q_2 and α_2. The impedance of the film was modeled as a constant–phase element with parameters Q_1 and α_1 assuming that the film has a distribution of resistivity normal to the electrode surface.

The fitting results are presented in Figure 4-7 in Nyquist format for the control case. OriginLab non–linear complex regression analysis with modulus weighting was used to fit the parameters to the data. The fitting results are presented in Table 4-1 along with the standard error for each parameter. Theoretically, R_t should be very large for the passive case and should decrease as the corrosion rate increases. The same circuit model was applied to the corroded case but the results were not realistic. Therefore, a

Table 4-1. Regression parameters and standard error for equivalent circuit fit to conventional three electrode impedance for the active and passive cases.

	Passive
R_e	$206\pm9.0\ \Omega\ \text{cm}^2$
R_{sp}	$31.57\pm0.86\ \text{k}\Omega\ \text{cm}^2$
R_t	$532\ \text{k}\pm26\Omega\ \text{cm}^2$
Q_1	$3.34\text{e-}4\pm0.04\text{e-}4\ \text{Ss}^\alpha\text{cm}^2$
α_1	0.86 ± 0.01
Q_2	$2.13\text{e-}4\pm0.01\ \text{Ss}^\alpha\text{cm}^2$
α_2	0.79 ± 0.01

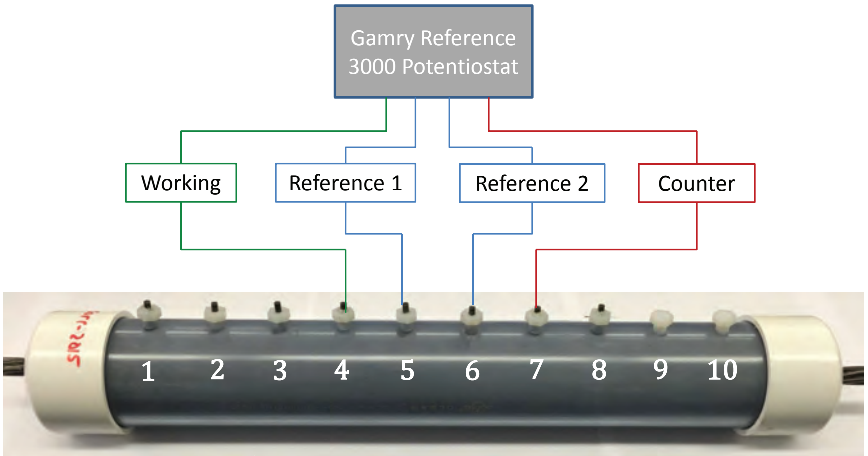

Figure 4-8. 2 ft. fabricated tendon with 10 electrode locations for measuring the indirect impedance and schematic of the four electrode measurement.

measurement model[3] was used to determine the extrapolated value of the zero frequency limit of the real impedance which signifies the lowest possible value of the polarization resistance. A series of Voight elements are fit to the impedance sequentially until the fit can not be improved with the addition of another element. The extrapolated value of the low frequency limit of the impedance is then based on the element which has the largest time constant. The value obtained was approximately 15 $k\Omega$ which is roughly 30 times less than the charge-transfer resistance obtained for the passive case.

4.3 Corrosion Detection Using Indirect Impedance

Experimental tendons were constructed to resemble a 2-ft. section of a 3-in. diameter tendon. A tendon is shown in Figure 4-8 in which a schematic diagram of a potentiostat shows the indirect impedance set-up. A 4–electrode array is used in which an ac current is passed between the outer two electrodes (working and counter) and the potential response is measured between the two inner electrodes (reference 1 and reference 2). For the initial ease of interpretation, tendon sections were made either with one steel strand located at the axis of the cylindrical duct or with just grout. A proprietary grout (Sika) was used as the filler and it was mixed according to manufacturer's specifications and allowed to cure for at least 30 days. Ten 1-cm diameter holes were drilled and tapped into the duct so that the electrodes could be screwed into place thereby preventing the grout from drying out at these points. An in-house electrolyte gel was used as the electrical contact between the titanium electrodes and the grout. The gel was made by mixing carboxyl–methyl cellulose polymer into an electrolyte solution of 1 M KSO4 until consistently viscous. Dimensionally stable 0.5 cm diameter titanium rods coated in iridium-oxide were used as the electrodes.

Impedance measurements on the tendons without the steel were compared to the measurements performed on the tendons with one steel strand. The results are shown in Figure 4-9. The impedance of each case is presented in Nyquist format in Figure 4-9A. The real part of the impedance of the grout only case is much larger than the tendon with the steel but has little capacitive response. The impedance measured on the tendon with the steel has a much smaller ohmic impedance but has a larger capacitive loop indicating that the indirect impedance must sample the properties of the steel. The real part of the impedance is shown in Figure 4-9B as a function of frequency. The real impedance of the tendon without steel is constant with frequency which means the impedance of the behaves as a resistor, and should reflect the resistivity of the grout.

Corrosion was forced on one of the tendons containing steel using an impressed current method. A schematic of the impressed current technique is shown in Figure 4-10. A power source was used to apply a fixed potential difference between the steel and two of the titanium electrodes such that corrosion would be induced on the steel surface

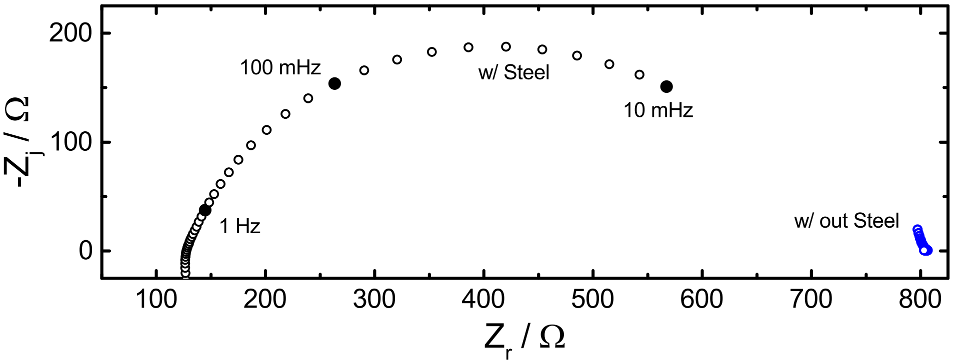

A

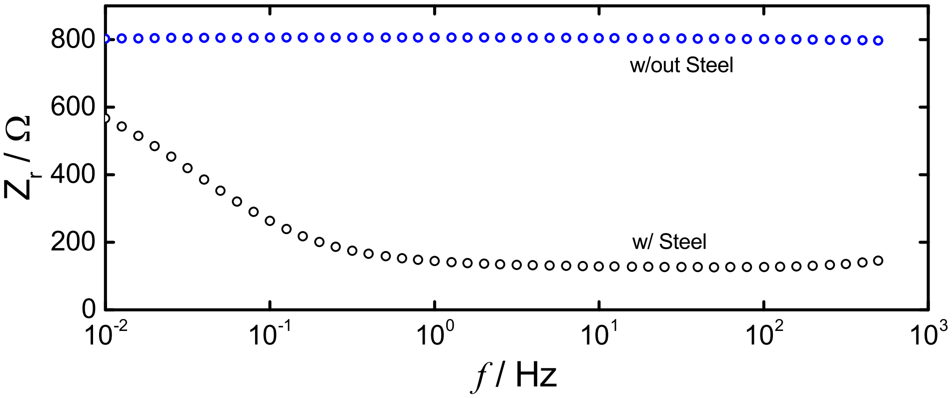

B

Figure 4-9. Indirect impedance of fabricated tendon with and without steel: a) in Nyquist format, b)the real impedance as a function of frequency.

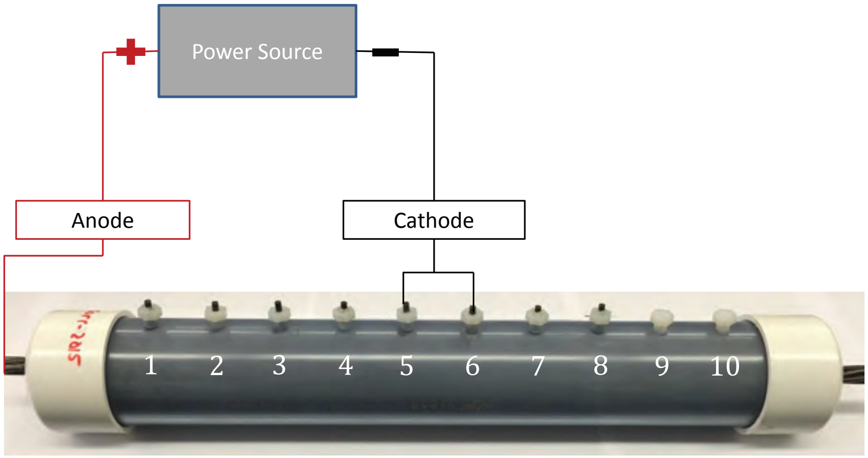

Figure 4-10. Schematic representation of the impressed current technique used to force corrosion.

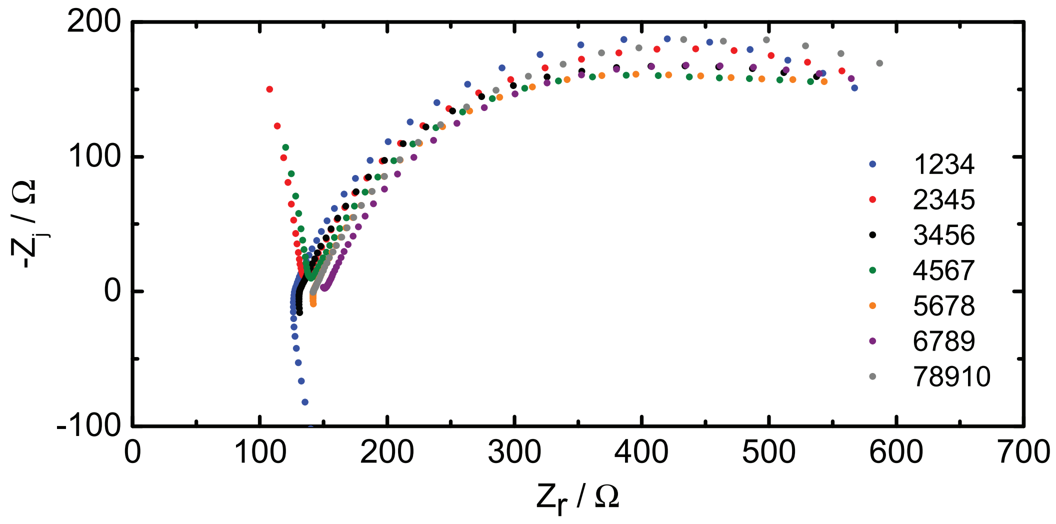

Figure 4-11. Indirect impedance in Nyquist format of a fabricated tendon with passive steel and electrode location as a parameter.

preferentially beneath the two electrodes. A constant potential of 20V was applied for 1 week. The average current that flowed during that time was approximately 150 μA/s.

The indirect impedance results are presented in Figure 4-11 with the location of the electrodes as a parameter. The numbers distinguishing each measurement correspond to the location of the electrodes in order of working, reference 1, reference2, and counter electrodes. The impedance at each location along the tendon contains a capacitive arc and an ohmic resistance between 125 and 155 Ω. There is little variation in the impedance between each location indicating that the impedance of the steel in the control case is for the most part uniform.

The impedance results of the corroded case are presented in Figure 4-12 with the location of the electrodes as a parameter. The same numbering scheme of the electrodes as in the corroded case was used. In the corroded case, the impedance varied significantly with location, indicating that the impedance of the steel was not uniform. The impedance at locations of corrosion should be smaller than the impedance of passive locations. The figure inset in Figure 4-12 shows a magnified view of the 3 smallest impedances. The location of the smallest impedance occurred at locations 1–2–3–4, 5–6–7–8, and 7–8–9–10.

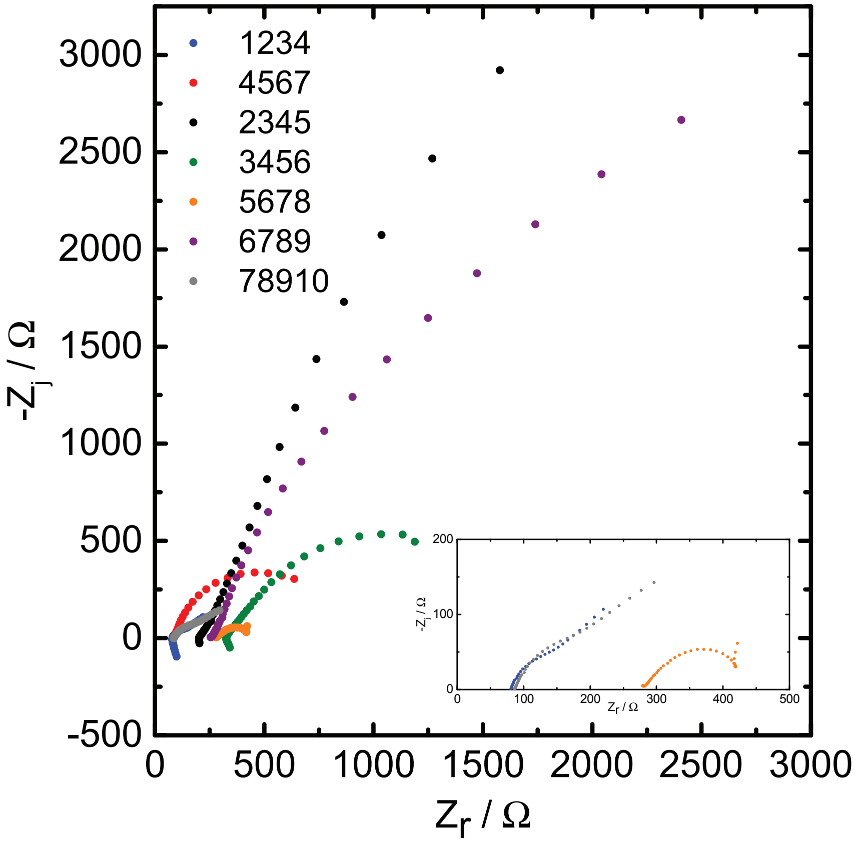

Figure 4-12. Indirect impedance in Nyquist format of a fabricated tendon with corroded steel and electrode location as a parameter.

According to the location of the cathodes in the impressed current technique, the corrosion should be located beneath electrodes 5 and 6. To verify this, the steel was extracted from the tendon by breaking apart the grout. Magnified images were taken along the surface of the steel to determine where the most severe corrosion was present. Images are presented in Figures 4-13 and 4-14 of the steel surface located beneath each electrode. At locations 2, 6, and 10 the surface of the steel is smooth and does not show any signs of corrosion. The locations with the most corrosion were beneath electrodes 1, 3, 5, and 7. Therefore, the indirect impedance measurements should signify corrosion at locations 1–2–3–4, 3–4–5–6, 5–6–7–8, 7–8–9–10. Three out of four of the of the locations did have small impedances but the impedance at location 3–4–5–6, for some reason, had an impedance more similar to a passive state. At steel location 5, Figure 4-13E, there was

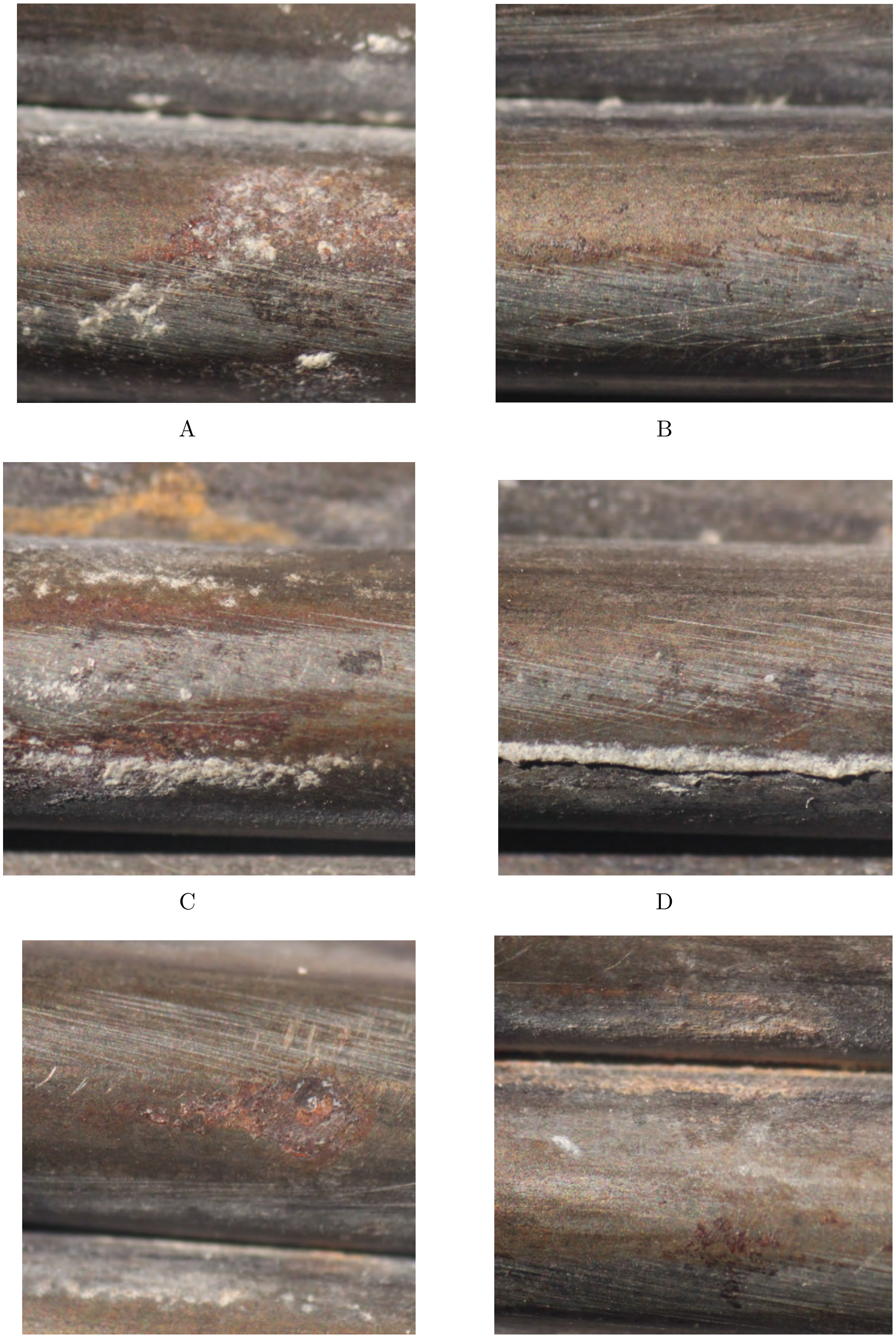

A

B

C

D

E

F

Figure 4-13. Images of the steel surface directly beneath each electrode for the corroded case.

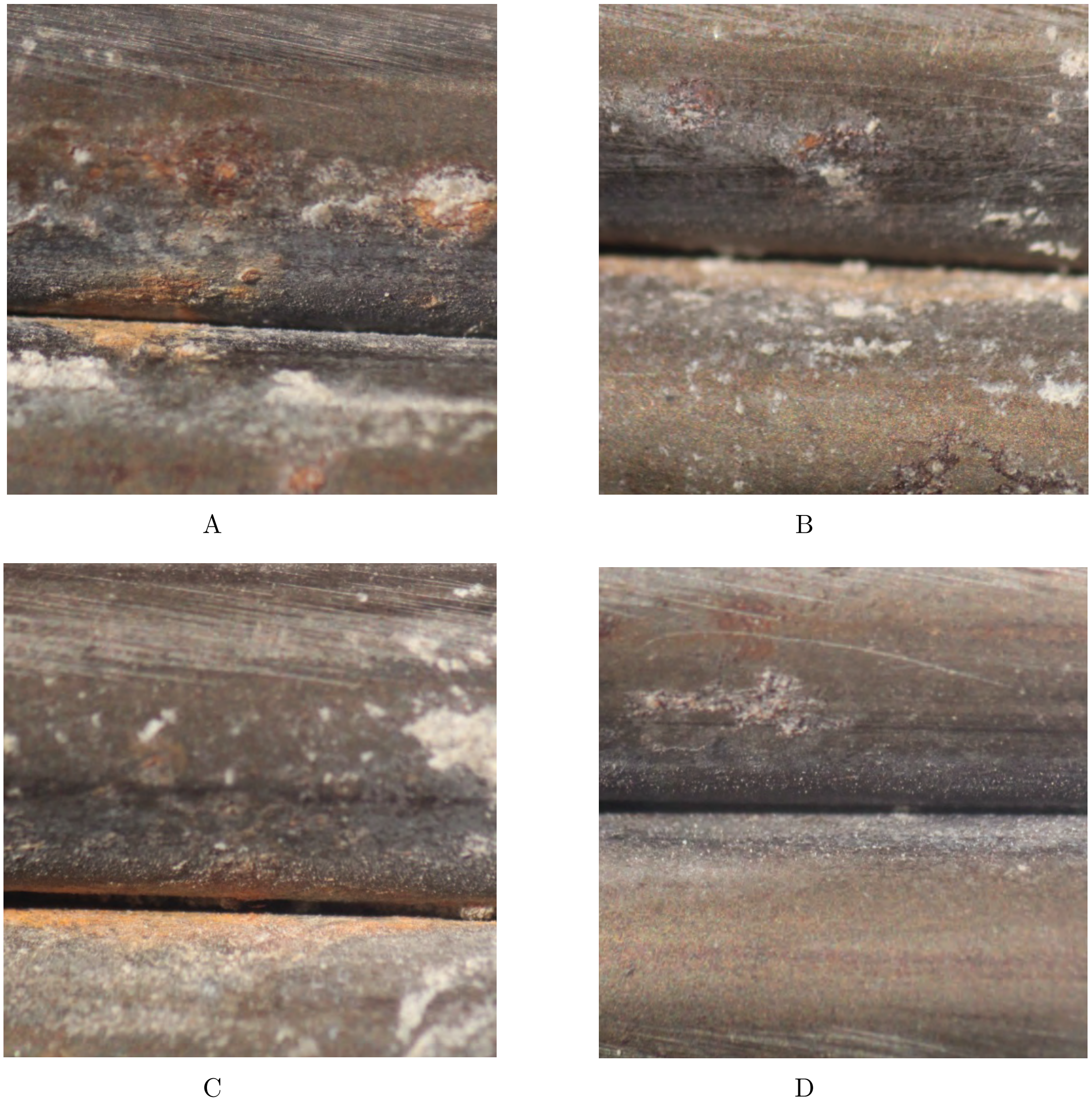

Figure 4-14. Images of the steel surface directly beneath each electrode for the corroded case.

a corrosion pit that formed. The corrosion product was in the form of a redish–brown rust. Some of the corrosion product was incidentally scratched off by the removal of the grout. The indirect impedance was small but also included an inductive loop at low frequencies usually associated with a modulating film. At steel location 4 there was a small longitudinal crack in the steel which is partially filled with grout indicating that the crack was there prior to constructing the tendon.

The indirect impedance measurements on a corroded tendon and a control tendon showed the ability to detect corrosion. The results presented here indicate that only the location of the steel directly beneath the working electrode is sensed. Finite element simulations to determine the location of the steel that is sensed and to develop a way of interpreting the measurements are described in the next chapter.

CHAPTER 5
FINITE ELEMENT SIMULATIONS AND INTERPRETATION

Finite element simulations of the indirect impedance measurement were performed to uncover the contribution of the grout resistivity to impedance as well as determine the location of the steel that a particular configuration sensed. The indirect impedance was found to include two separate contributions of the grout resistivity. There is an ohmic impedance associated with the grout that is parallel to the steel and another ohmic impedance associated with the grout that is in series to the steel. The parallel component was much larger than the series component, and the impedance decreased with decreased frequency, whereas, the series component increased with decreased frequency. By understanding the exact influence the grout has on the indirect impedance, a method may be devised to extract the properties of the steel and determine the corrosion rate.

5.1 Mathematical Development

To aid in the interpretation of the experimental results, a finite element model was developed to simulate the indirect impedance. Huang et al.[28] explained the use of linear kinetics as the boundary condition on a disk electrode based on the derivations of Newman[50] and Nisancioglu.[53, 54] The normal current density at the surface of the electrode can be expressed in terms of a faradaic reaction and a charging current as

$$i = C\frac{\partial(V-\Phi)}{\partial t} + \frac{(\alpha_{\mathrm{a}}+\alpha_{\mathrm{c}})i_0\mathrm{F}}{\mathrm{R}T}(V-\Phi) = -\kappa\frac{\partial\Phi}{\partial y} \tag{5–1}$$

The oscillating current density may be expressed in the frequency domain as

$$\tilde{i} = \mathrm{j}\omega C(\tilde{V}-\tilde{\Phi}) + \frac{(\alpha_{\mathrm{a}}+\alpha_{\mathrm{c}})i_0\mathrm{F}}{\mathrm{R}T}(\tilde{V}-\tilde{\Phi}) \tag{5–2}$$

with the use of the relationship

$$i = \bar{i} + \mathrm{Re}\left\{\tilde{i}e^{\mathrm{j}\omega t}\right\} \tag{5–3}$$

where the current is expressed as the addition of a steady-state and an oscillating term. In Equation 5–2, $\tilde{V}$ is the potential perturbation, and $\tilde{\Phi}$ is the complex oscillating potential within the electrolyte. For the indirect impedance simulation both the working and counter electrode boundary conditions were set as oscillating currents with a positive potential perturbation applied to the working electrode and a negative one applied to the counter electrode. A similar boundary condition was set at the steel but with the potential set to zero such that all other potentials would be in referenced to the steel. The steel was modeled for an active corrosion case and a passive blocking electrode case. The active case, Equation 5–4, is expressed as the addition of the charging and faradaic current, i.e.,

$$\tilde{i} = \mathrm{j}\omega C(-\tilde{\Phi}) + \frac{(\alpha_{\mathrm{a}} + \alpha_{\mathrm{c}})i_0\mathrm{F}}{\mathrm{R}T}(-\tilde{\Phi}) \tag{5–4}$$

The oscillating potential solution is found by solving Laplace's equation with the given frequency-dependent boundary conditions. With the use of potential probes the impedance is simulated as the quotient of the potential difference between two reference probes and the current perturbation applied between the current-injecting electrodes expressed as

$$Z = \frac{\tilde{V}_{\mathrm{ref1}} - \tilde{V}_{\mathrm{ref2}}}{\tilde{I}} \tag{5–5}$$

The charge-transfer resistance for linear kinetics can be expressed in terms of the exchange current density as

$$R_t = \frac{\mathrm{R}T}{i_0\left(\alpha_{\mathrm{a}} + \alpha_{\mathrm{c}}\right)} \tag{5–6}$$

which is the same expression used to estimate the polarization resistance of the steel in the corroding case. The 3D potential distribution was determined under the assumption of uniform electrolyte conductivity, and the indirect impedance was simulated.

The active case, Equation 5–7, is expressed as the addition of the charging and faradaic current.

$$\tilde{i} = j\omega C(-\tilde{\Phi}) + \frac{(\alpha_a + \alpha_c)i_0F}{RT}(-\tilde{\Phi}) \tag{5–7}$$

The passive case is modeled using a Constant-Phase-Element (CPE) with an impedance of

$$Z_{CPE} = \frac{1}{(j\omega)^{\alpha}Q} \tag{5–8}$$

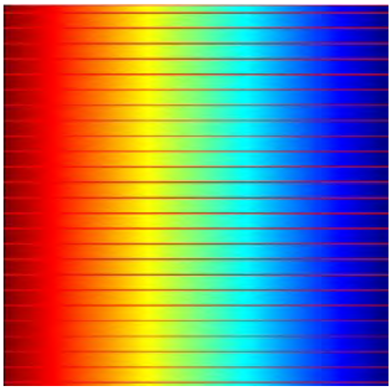

Figure 5-1. Current and potential distribution of a 1 cm square 10 Ohm-m resistivity grout model with current injecting electrodes placed on the vertical sides

where the phase angle is independent of frequency. When $\alpha = 1$, Q has units of capacitance. When α does not equal unity the system has a distribution of time constants or surface heterogeneity either normal or parallel to the surface. [57] The expression used to represent blocking behavior at the steel for the normal current density of a CPE is

$$\tilde{i} = -\tilde{\phi}\omega^{\alpha}Q\left[\cos(\alpha\frac{\pi}{2}) + j\sin(\alpha\frac{\pi}{2})\right] \tag{5–9}$$

The oscillating potential solution is found by solving Laplace's equation with the given frequency-dependent boundary conditions.

5.2 Justification of Boundary Conditions

A 2D square of uniform conductivity, Figure 5-1, was modeled to confirm the oscillating current boundary conditions. The vertical sides of the square acted as the current-injecting electrodes. The potential distribution is shown by the color gradient in Figure 5-1 and the current path is shown by the horizontal red lines. The 2-pt impedance was simulated by dividing the potential difference between the electrodes by the total current crossing one of the electrode boundaries. At all frequencies the real impedance, Figure 5-2, is the resistivity of the electrolyte multiplied by the distance between the electrodes and divided by the cross sectional area. The imaginary impedance is zero since the grout is modeled as a homogenous material with a constant resistance without any dielectric properties.

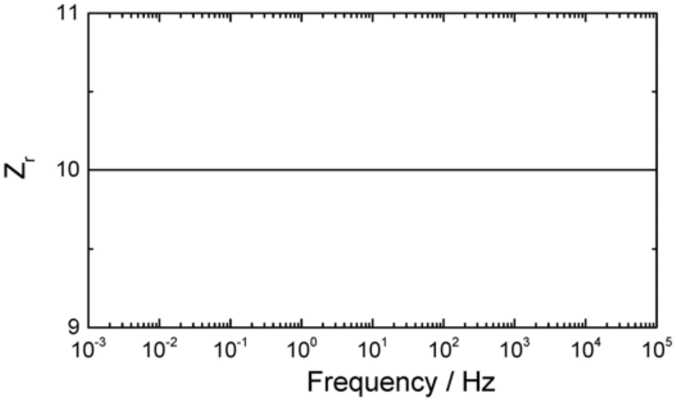

Figure 5-2. Simulated real impedance of as a function of frequency of a 1 cm square grout model with current injecting electrodes placed on the vertical sides.

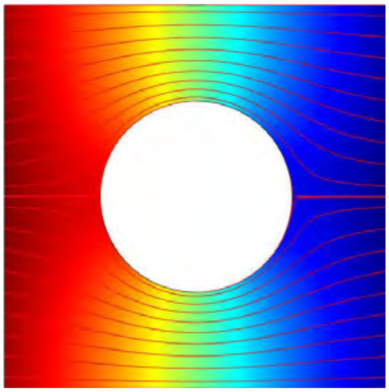

Figure 5-3. Current and potential distribution at the low frequency limit of a 1 cm square grout model with a 0.25 cm radius steel placed in the center and current injecting electrodes placed on the vertical sides.

A steel circular element was inserted into the grout model with the boundary condition described by Equation 5–7. The charge-transfer resistance was set to and the double layer capacitance was. At low frequencies, Figure 5-3, the steel behaves as an open circuit due to the dominance of the charge-transfer resistance and repels the current. At high frequencies, Figure 5-4, it behaves as a closed-circuit and the current enters it normal to the surface. These results are consistent with those of Keddam et al.[33] The Nyquist plot of the simulated impedance, Figure 5-5, is a capacitive loop representative of a resistor and a capacitor in parallel. This is a simple model that shows the concept of indirect impedance, and confirms the use of the oscillating boundary conditions.

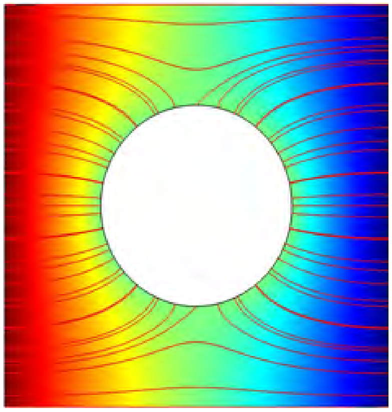

Figure 5-4. Current and potential distribution at the high frequency limit of a 1 cm square grout model with a 0.25 cm radius steel circle placed in the center and current injecting electrodes placed on the vertical sides.

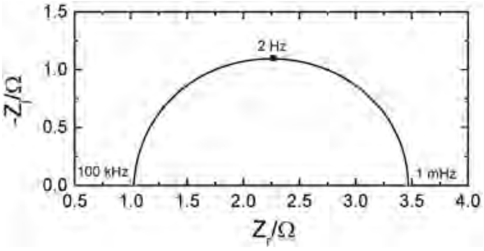

Figure 5-5. Simulated impedance of a 1 cm square grout model with a 0.25 cm radius steel circle placed in the center and current injecting electrodes placed on the vertical sides

A three-dimensional, 60cm long cylindrical section of a tendon was modeled, with and without steel to simulate the impedance of a post-tensioned tendon. The steel strand is 0.625cm in radius and is located along the longitudinal axis of the cylinder. All dimensions of the model were made to match the fabricated tendons. The mesh of the model, Figure 5-6, is composed of free tetrahedral elements which decrease in size at the electrode boundaries. Boundary layer elements were added to the steel and electrode boundaries. Reference electrodes were placed along the surface to analyze the potential distribution along the surface.

5.3 Results & Analysis

The simulated indirect impedance is presented for a finite element model tendon with one steel strand. The parameters used were $R_\mathrm{t} = 11.8$ kΩcm^2, $C = 20$ μF/cm^2,

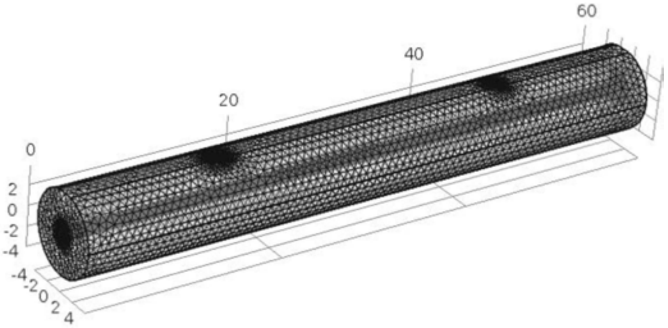

Figure 5-6. Mesh of the 3D tendon model.

and $\rho = 125\ \Omega$ m. An equivalent circuit is presented to fit the impedance based on the ohmic impedance of the grout and the interfacial impedance of the steel. A simplified analogue circuit is presented which reduces the equivalent circuit to three components. A sensitivity analysis of the parameters to changes in steel polarization resistance as well as the distance between the measurement electrodes is also presented.

5.3.1 Experimental Data Fitting

The passive case simulation was used to iteratively fit the experimental impedance by first estimating the resistivity of the grout as 125 Ω-m and iterating the CPE parameters at the steel. Q was found to be $0.9Ss^{\alpha}$ and α was 0.9. The simulated impedance is shown to fit experimental data of 2 electrode configurations at low frequencies, provided in Figures 5-7 and 5-8. The fitting of the indirect impedance for two different electrode configurations is a validation of our finite element model in its ability to replicate experimental measurements and therefore may be used to establish an interpretation procedure.

5.3.2 Determination of Steel Sensing Area

The area of steel that is sensed for each electrode arrangement is required for the interpretation. The indirect impedance was simulated for 3 different cases: a fully passive steel strand, a uniformly corroding steel strand, and a passive strand with a localized area of corrosion at the center indicated by the red section in Figure 5-9. Twenty-five

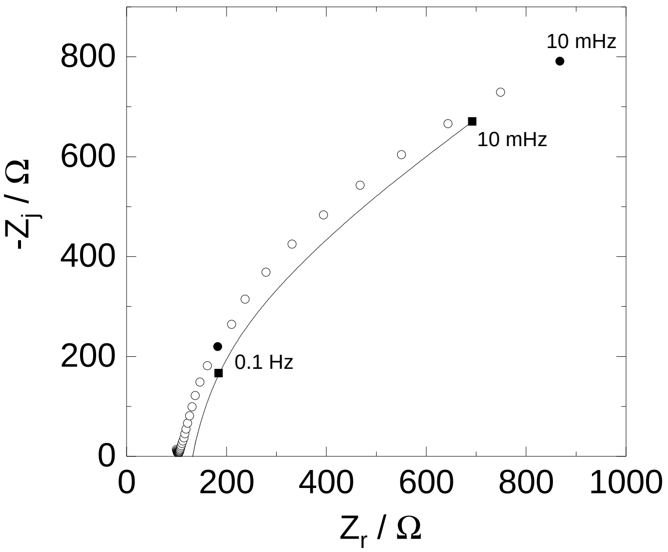

Figure 5-7. Simulated impedance results compared to the experimental results with an electrode configuration of 1357.

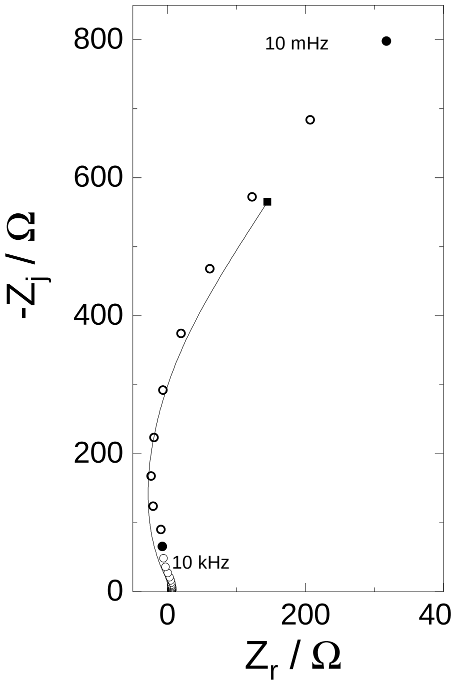

Figure 5-8. Simulated impedance results compared to the experimental results with an electrode configuration of 2356.

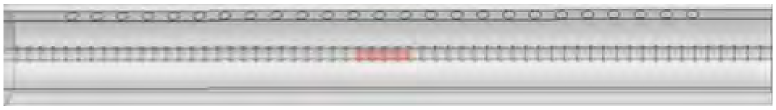

Figure 5-9. Tendon model with locally corroding section in the center of the steel.

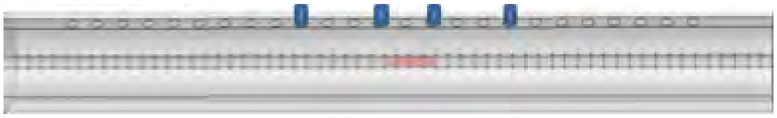

Figure 5-10. Schematic representation of the system geometry for a reference electrode spacing of 4 cm.

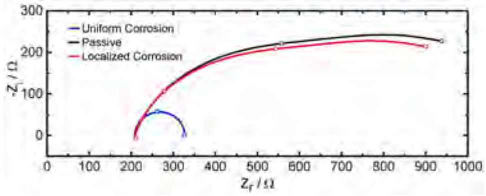

Figure 5-11. Simulated indirect impedance of a 2ft model tendon containing 1 steel strand for a passive case, a locally corroding cases of 4cm at the midpoint of the steel strand, and a uniformly corroding steel for a reference electrode spacing of 4 cm

electrode points were placed along the surface such that multiple electrode configurations could be simulated at once.

In one set of simulations the electrodes were placed with the centerline of the array directly over the active site as is shown in Figure 5-10. The distance between the two reference electrodes was varied from 32 cm to 4 cm to determine if there is a maximum distance in which the corrosion could not be detected. When the electrodes were spaced at 32 cm, the difference between the passive case and the locally corroding case was extremely small. As the electrodes were moved closer together, the difference increased, but, even when the reference electrodes were placed just above the active location, Figure 5-11, the impedance of the locally corroding case alone did not indicate the presence of corrosion. However, the presence of a small difference even when the reference electrode distance is 32 cm indicates that the polarized steel area extends far out from the electrode points, but the location of steel most sensed is not at the centerline of the electrode array.

In the another set of simulations, the electrodes were equally spaced at 4 cm and were moved along the tendon to mimic a likely procedure for a field application. In this case, when the midpoint of the electrode array was 18 cm left of the active location, the

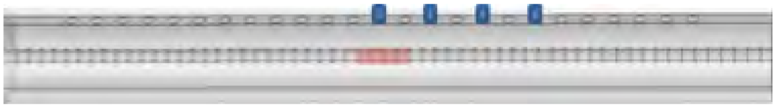

Figure 5-12. Schematic representation of the system geometry for a reference electrode spacing of 4 cm.

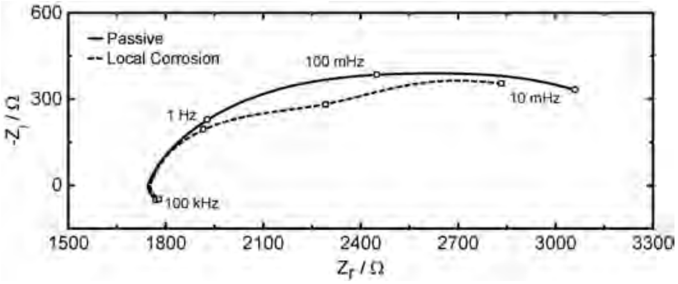

Figure 5-13. Simulated indirect impedance of a 2ft model tendon containing 1 steel strand for a passive case, and a locally corroding cases of 4cm at the midpoint of the steel strand with the electrodes equally spaced at 4cm. The centerline of the electrode array is 6cm right of the centerline of the 2ft tendon and the working electrode is directly over the corroding area.

impedance of the passive and the actively corroding case showed only small differences at lower frequencies. When the electrodes were located 10 cm from the corroding section, the difference became more apparent. However, when one of the reference electrodes was directly over the site of corrosion, the difference diminished. The most prominent difference occurred when the current injection electrode was directly over the site of corrosion, as is shown in Figure 5-12. The simulated impedance results for this configuration are shown in Figure 5-13 in Nyquist format. The passive case shows one depressed capacitive loop while the corroding case shows two overlapping time constants.

5.3.3 Equivalent Circuit

During the indirect impedance measurement, current flows through the grout as well as through the steel. If the contribution of the grout resistivity to the indirect impedance can be determined, then the total steel impedance may be extracted. All previous researchers have attempted to address the contribution of the grout resistivity to the indirect impedance with the use of resistors in series or parallel to the impedance of

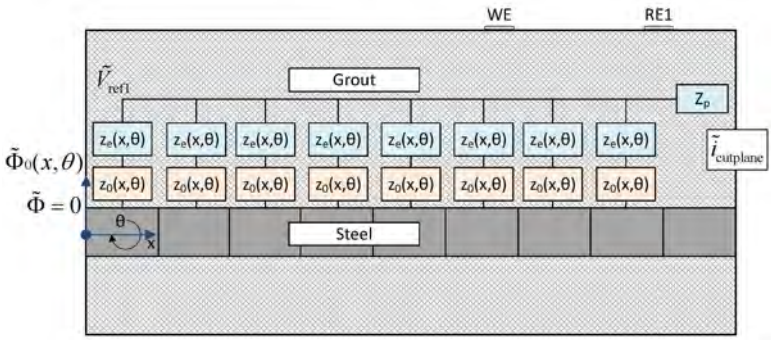

Figure 5-14. Equivalent circuit diagram used to represent the indirect impedance.

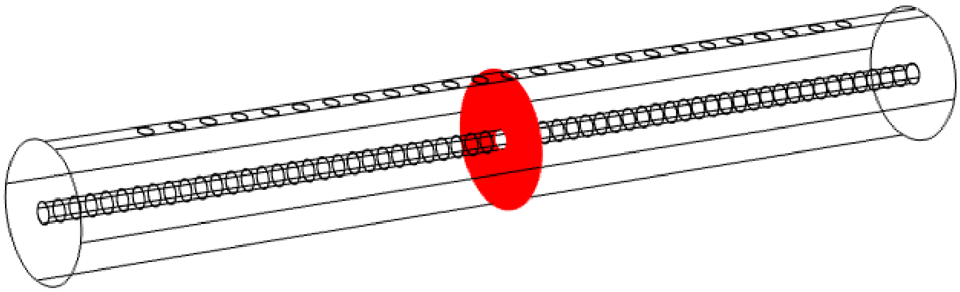

Figure 5-15. Cut plane used to determine the oscillating current through the grout.

the steel. However, due to the nonuniform potential distribution along the surface of the steel and throughout the resistive material, the contribution of the grout must be in the form of an ohmic impedance with real and imaginary parts.

The appropriate equivalent circuit model for an indirect impedance measurement is shown in Figure 5-14. There are two primary current paths from the working electrode to the counter electrode. The current may either run parallel to the steel or in series to the steel. Since some of the current can take one path while the rest takes the other, these two paths must be in parallel. The impedance of the parallel path may be expressed as

$$Z_{\text{parallel}} = \frac{\tilde{V}_{\text{ref1}} - \tilde{V}_{\text{ref2}}}{\tilde{i}_{\text{cutplane}}} \tag{5–10}$$

in which the potential difference between the two reference electrodes is divided by the total current through a plane located at the midpoint of the electrode array as shown in Figure 5-15. The plane only includes the cross-section of the resistive material and not the steel.

The series path impedance must contain the impedance through the grout as well as the interfacial impedance of the steel. Due to the nonuniform potential distribution throughout the grout and along the steel surface the series path impedance must be expressed as

$$Z_{\mathrm{s}} = \left(\int_0^{60} \int_0^{360} \frac{1}{z_{\mathrm{e}}(x,\theta) + z_0(x,\theta)} d\theta dx \right)^{-1} \tag{5–11}$$

in which the sum of the local ohmic and interfacial impedances as a function of position on the surface of the steel are integrated in a parallel fashion. A diagram showing the local ohmic and interfacial impedances configurations is provided in Figure 5-14.

The local ohmic impedance is calculated as

$$z_{\mathrm{e}}(x,\theta) = \frac{\tilde{V}_{ref} - \tilde{\Phi}_0(x,\theta)}{\tilde{i}_0(x,\theta)} \tag{5–12}$$

which is based on the potential difference of the reference electrode and the potential on a point of the steel. The modulus of the ohmic and interfacial impedances is presented in Figure 5-16 as a function of axial location for $\theta = 0$. The solid lines represent the local ohmic impedance and the dashed lines represent the local interfacial impedance. The interfacial impedance is uniform along the steel surface and increases with frequency. The ohmic impedance is nonuniform along the length of the steel and reaches a minimum at the working and counter electrode locations. The ohmic impedance outside the electrode array increases with increases in frequency. At high frequencies, the series path impedance is mostly comprised of the ohmic impedance contribution. At low frequencies the interfacial impedance is on the same order as the ohmic impedance at locations near the working and counter electrodes.

For simplicity, the series path impedance was calculated by segmenting the steel surface into 1 cm by 90° sections and calculating the global ohmic and interfacial impedances of each section. The series impedance was then evaluated as the parallel combination of the global impedances between the reference electrode and a segment of

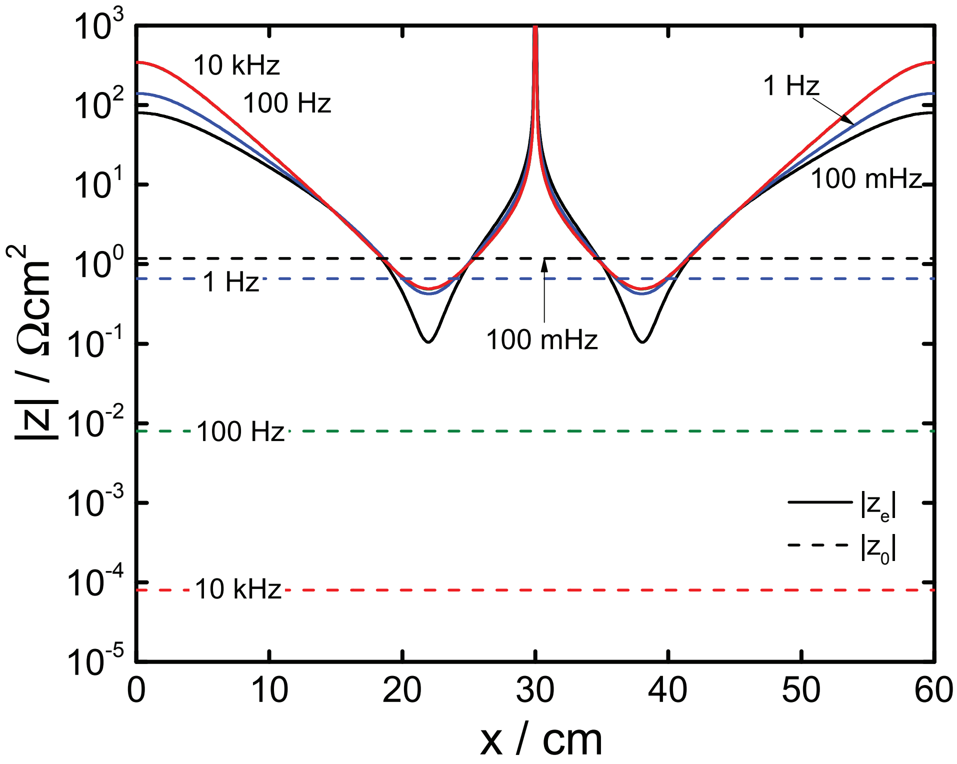

Figure 5-16. Magnitude of the series local ohmic impedance(solid lines) and the local interfacial impedance(dashed lines) as a function of steel position with frequency as a parameter.

the steel surface. The ohmic impedance between the reference electrode and a segment of steel may be expressed as

$$Z_{\mathrm{e,segment}} = \frac{\tilde{V}_{\mathrm{ref1}} - \tilde{V}_{\mathrm{avg,segment}}}{\tilde{i}_{\mathrm{segment}}} \tag{5–13}$$

The ohmic impedance of the first half of the steel segments is calculated based on $\tilde{V}_{\mathrm{ref1}}$ and the second half of the segments is calculated using $\tilde{V}_{\mathrm{ref2}}$. It is necessary to segment the steel to account for the large variation in potential along the steel surface which results in a distribution of local ohmic impedance.

The ohmic impedance in Nyquist format at three segments located outside the electrode array and one located inside the array is shown in Figure 5-17. The ohmic impedance at 1 cm, shown in Figure 5-17A, is inductive and at locations 16 cm (Figure 5-17B) and 17 cm (Figure 5-17C), which are closer to the electrode array, the impedance is

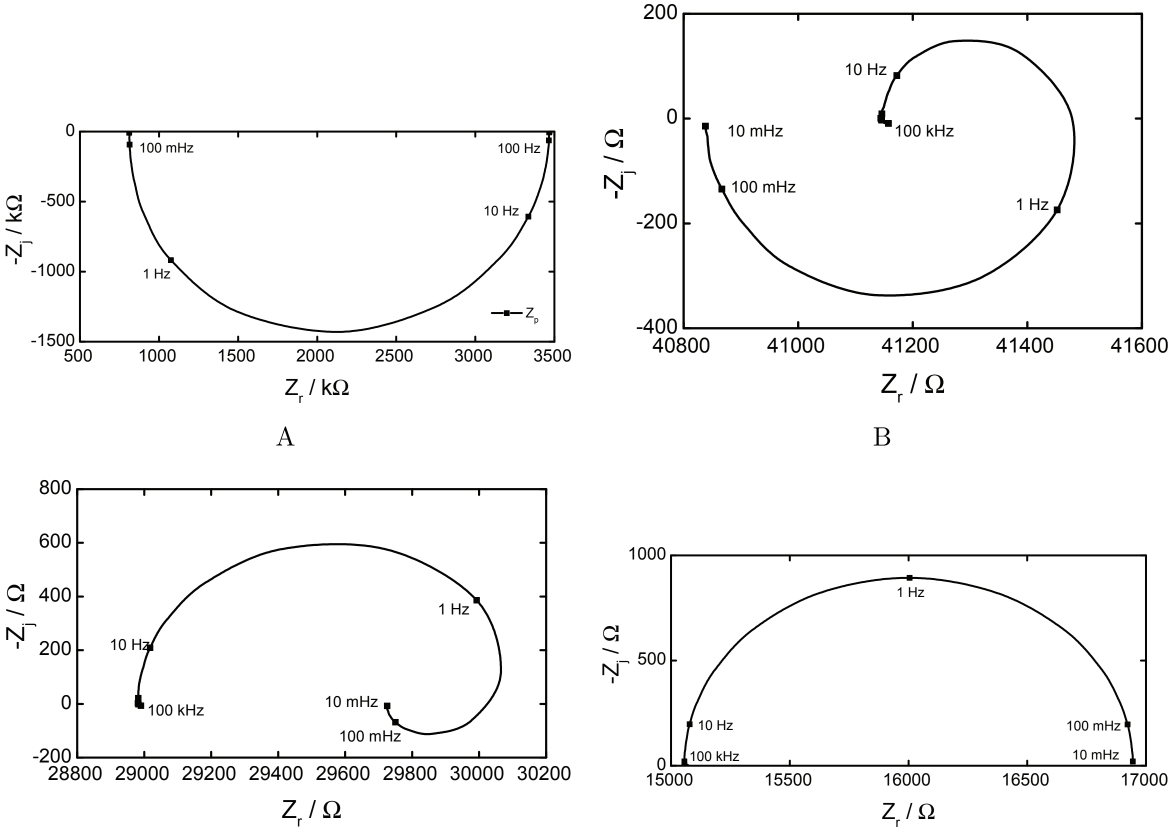

A B

C D

Figure 5-17. The ohmic impedance of a segment located at: a) 1, b) 16, c) 17, d) 26.

capacitive at high frequencies and inductive at low frequencies. The ohmic impedance at location 26 cm (Figure 5-17D), which is located within the electrode array, is capacitive.

The total series impedance for each section of steel may be expressed as

$$Z_{\text{segment}} = Z_{\text{e,segment}} + Z_{0,\text{segment}} \tag{5–14}$$

where $Z_{0,\text{segment}}$ represents the interfacial impedance and may be expressed as

$$Z_{0,\text{segment}} = \frac{\tilde{V}_{\text{avg,segment}}}{\tilde{i}_{\text{segment}}} \tag{5–15}$$

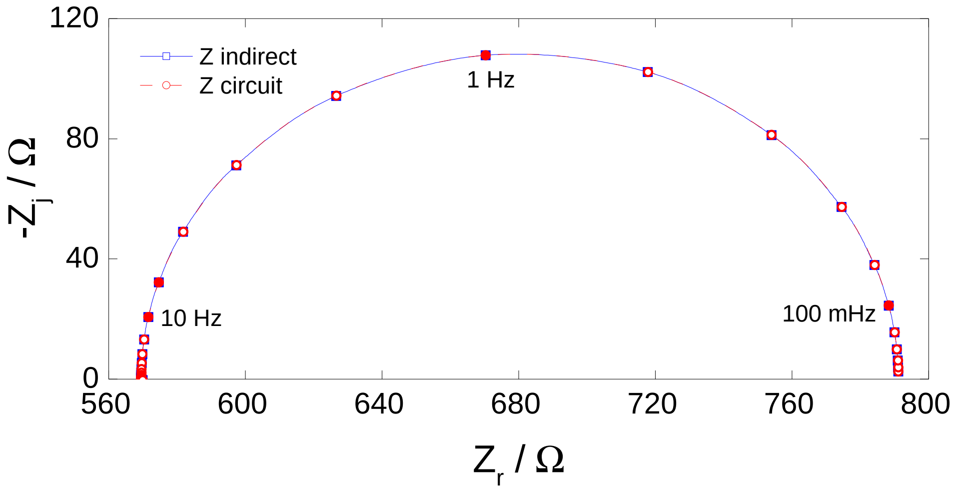

Figure 5-18. Simulated indirect impedance and equivalent circuit impedance calculated using Equation 5–17 in Nyquist format.

which is the quotient of the average oscillating potential of a segment and the oscillating current through segment. The complete series impedance may be expressed as

$$Z_{\text{series}} = \frac{1}{\sum_{1}^{\text{segments}} \frac{1}{Z_{\text{segment}}}} \tag{5–16}$$

which is a parallel combination of the series impedances for each segment. The indirect impedance may be expressed as

$$Z_{\text{indirect}} = \frac{Z_{\text{series}} Z_{\text{parallel}}}{Z_{\text{series}} + Z_{\text{parallel}}} \tag{5–17}$$

representing a parallel combination of the series path impedance and the parallel path impedance.

A comparison of the simulated indirect impedance and the impedance calculated using Equation 5–17 is shown in Figure 5-18. The two impedances are nearly identical. Any error between the simulated indirect impedance and the circuit impedance is due to the averaging of the potential along the surface of each steel segment. The error decreases with decreases in the size of the segments. The breakdown of the indirect impedance presented here may also be extended to account for multiple steel strands. The series

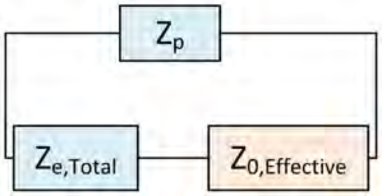

Figure 5-19. Reduced analogue circuit used to represent the indirect impedance.

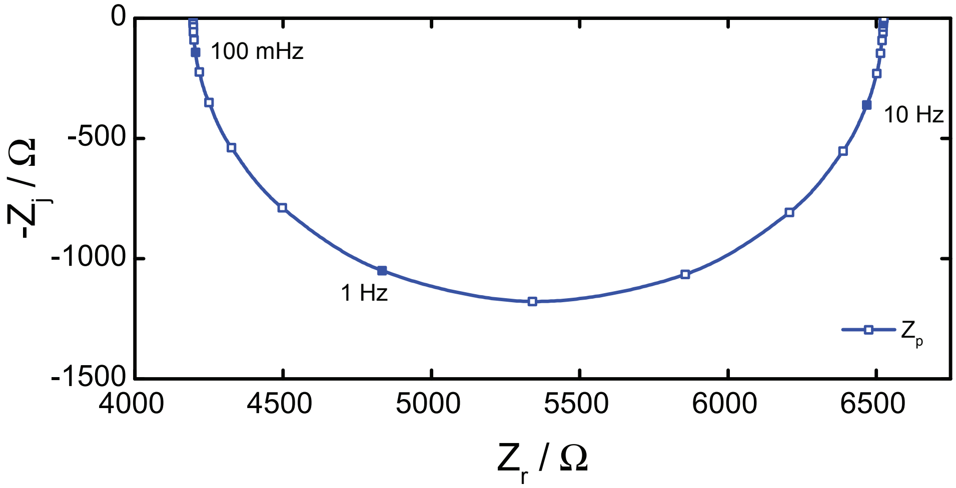

Figure 5-20. Simulated parallel ohmic impedance.

ohmic impedance to each strand may be calculated and each of them would be added in parallel.

5.3.4 Analogue Circuit

Due to the nonuniform current distribution imposed by the unusual geometry of the electrode configuration in an indirect impedance measurement, the contribution of the grout resistivity to the overall indirect impedance is in the form of an ohmic impedance and has real and imaginary parts. Therefore, an equivalent circuit containing linear elements that properly describes the system is not feasible.

A more appropriate circuit expresses the contribution of the grout resistivity in terms of an ohmic impedance such as the circuit shown in Figure 5-19. The parallel path impedance is the same as expressed in Equation 5–10 for the equivalent circuit. The parallel ohmic impedance is presented in Figure 5-20. The parallel impedance is inductive

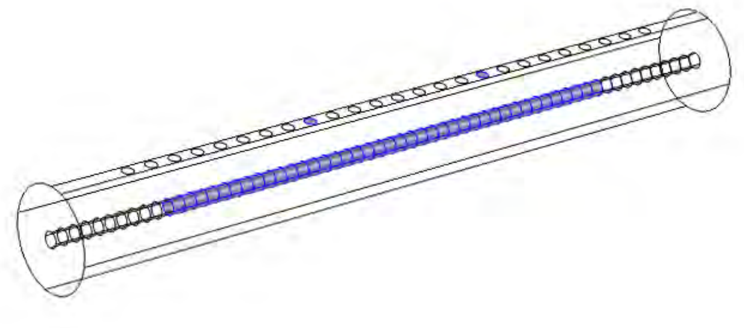

Figure 5-21. Schematic showing the effective area of polarized steel.

and large in comparison to the overall impedance.

As described in Equation 5–14 the series path impedance contains the series ohmic contribution of the grout as well as the steel interfacial impedance. To subtract the total steel interfacial impedance from the series path impedance, the effective polarized area of steel needs to be estimated. Technically, the entire steel surface is polarized since the potential everywhere along the steel is non-zero. However, the further location of the steel segment is from the current-injecting electrodes, the larger the ohmic contribution for that segment is and the less influence the steel interfacial impedance of that segment has.

The effective area of polarized steel was determined by decreasing the polarization resistance of a segment by a factor of 10 and assessing how the overall impedance changed. If the low frequency limit of the indirect impedance changed by more than one percent, the segment of steel was categorized as polarized. The effective area of polarized steel is shown in Figure 5-21. The effective area of steel that is polarized during the indirect impedance did not include the outer 10 cm of the steel strand.

The effective series ohmic impedance, shown in Figure 5-22, was found by subtracting the total interfacial impedance based on the effective polarized area of steel from the series path impedance, also presented in Figure 5-22. The series and parallel ohmic impedances make it difficult to interpret the indirect impedance. However, without taking into account

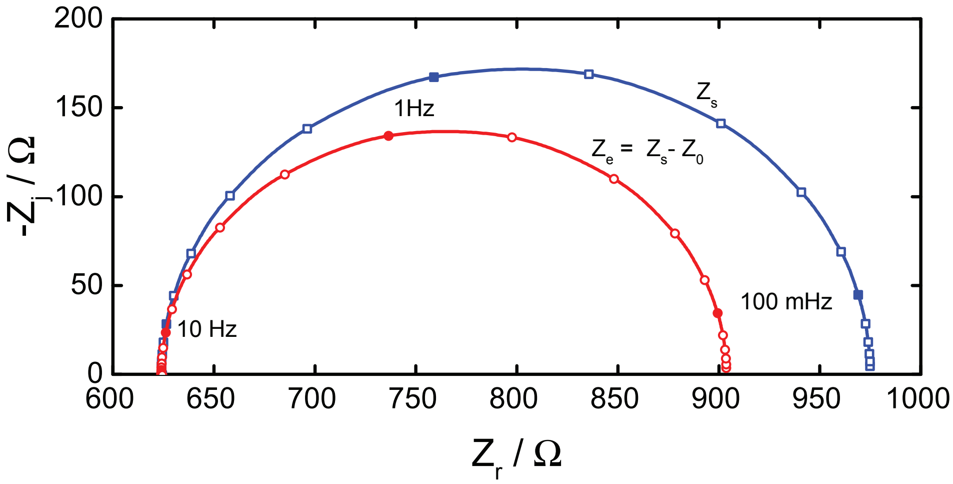

Figure 5-22. Series path simulated impedance and series simulated ohmic impedance.

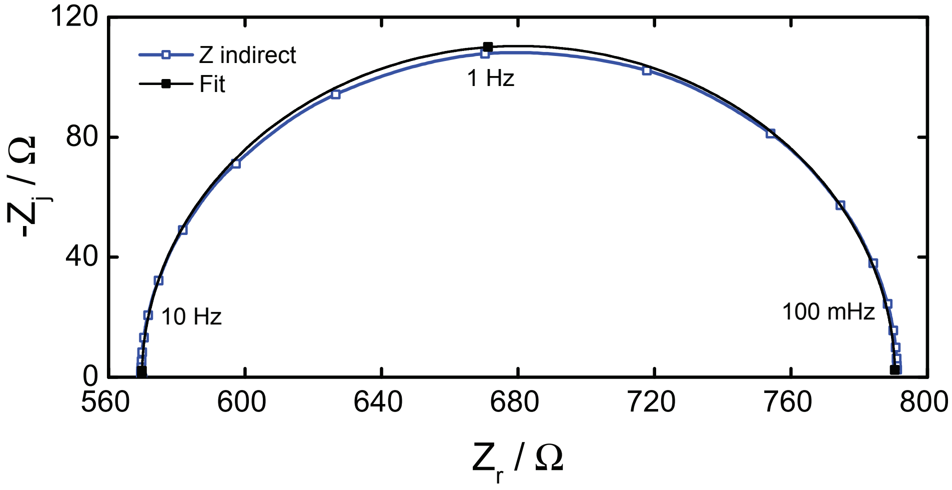

Figure 5-23. Simulated indirect impedance and the impedance calculated from a circuit containing resistors instead of the series and parallel ohmic impedances.

the variation in ohmic impedance as a function of frequency, the polarization resistance of the steel will be overestimated indicating that the corrosion rate of the steel is actually slower than is the case.

As an example, a circuit in which the series and parallel ohmic impedances were expressed as resistors was fit to the indirect impedance, shown in Figure 5-23. The regression yielded an estimated total polarization resistance of 313.1 Ω, whereas, the actual total polarization resistance based on the effective area of steel was 71.2Ω. Without

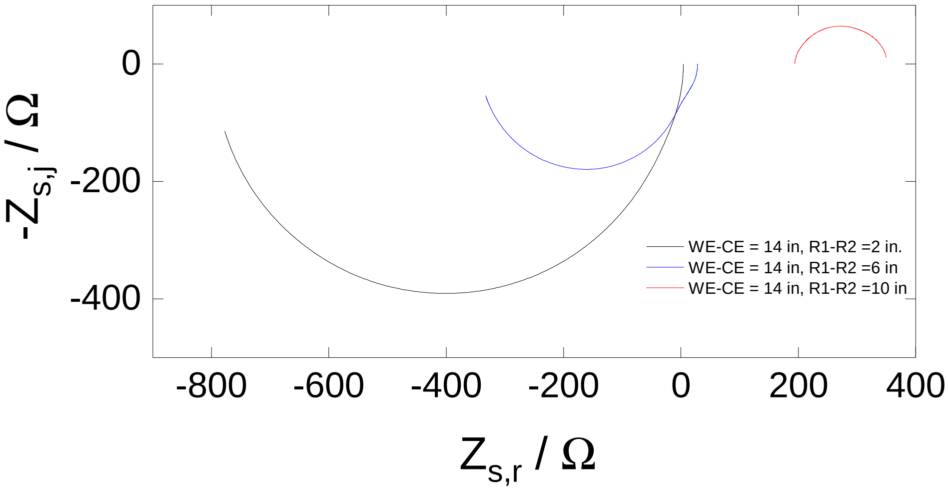

Figure 5-24. The series ohmic impedance in Nyquist format with the spacing between reference electrodes as a parameter.

accounting for the complex nature of the ohmic contributions to the indirect impedance measurement, the polarization resistance was overestimated by a factor of more than four.

5.3.5 Influence of Electrode Configuration

The ohmic impedance parameters vary with changes in the placement of the measurement electrodes. Simulations were performed in which the distance between the reference electrodes was increased while the distance between the working electrode and counterelectrode were held fixed. Simulations were also performed in which the distance between the working electrodes was increased as the distance between the reference electrodes were held fixed. The effective series and parallel ohmic impedances were calculated for each case.

The series ohmic impedance is shown in Figure 5-24 in Nyquist format with the distance between the two reference electrode as a parameter. The distance between the working electrode and counterelectrode was fixed at 14-in. while the distance between the references electrodes was increased from 2-in. to 10-in. by increments of 4-in. The results indicate that the series ohmic impedance is a strong function of the distance between the working electrodes and the reference electrodes. When this distance is large, the series ohmic impedance is inductive as is shown in the cases where the reference electrode

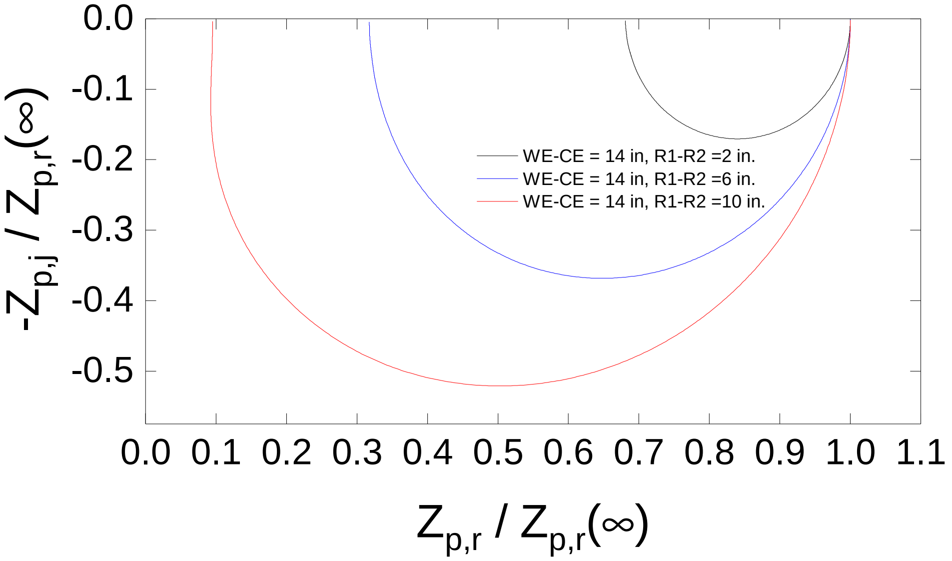

Figure 5-25. The parallel ohmic impedance scaled by the high frequency limit of the real part of the parallel ohmic impedance in Nyquist format with the distance between reference electrode as a parameter.

spacing is 2-in. and 6-in. When the distance between the reference electrodes is 10-in. and the distance between the working electrode and the reference electrode is 2-in., the series ohmic impedance is capacitive. Another interesting feature is at low frequencies the series ohmic impedance is negative which would lead to large distortions in the overall indirect impedance.

The parallel ohmic impedance is shown in Figure 5-25 for the same set of simulations presented in Figure 5-24. The results are shown in Nyquist format but scaled by the high frequency limit of the impedance since the parallel impedance varied significantly with changes in the reference electrode spacing. The parallel ohmic impedance was inductive for each case and the size of the inductive loop increased with increases in the reference electrode spacing. Also, the shape of the inductive loop became more deformed with larger distance between reference electrodes.

The series ohmic impedance is shown in Figure 5-26 in Nyquist format with the distance between the working and counter electrodes as a parameter while the distance between the reference electrodes was fixed at 2 *in*. The results are similar to the case when

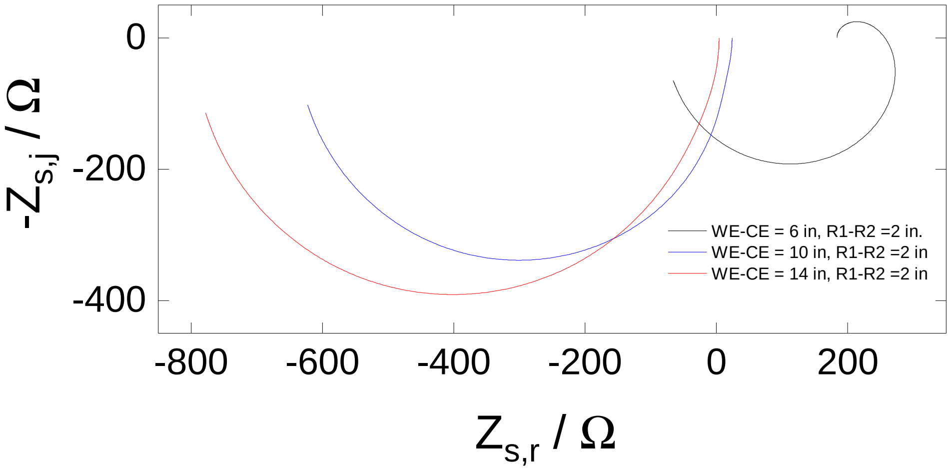

Figure 5-26. The series ohmic impedance in Nyquist format with the distance between the working and counter electrode as a parameter.

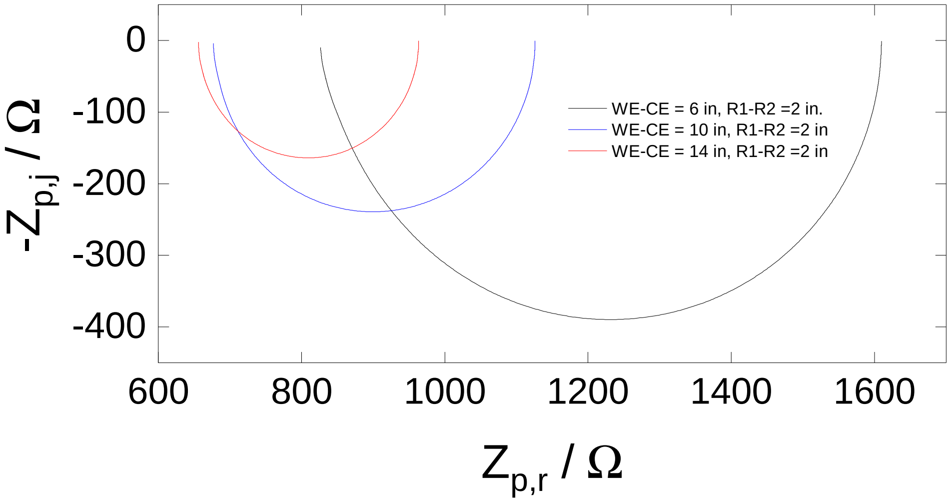

Figure 5-27. The parallel ohmic impedance in Nyquist format with the distance between the working and counter electrode as a parameter.

the distance between reference electrodes was increased, which indicates that the series ohmic impedance is most sensitive to the distance between the working electrode and the reference electrode.

The parallel ohmic impedance is shown in Figure 5-27 in Nyquist format with the distance for the same electrode spacings as presented in Figure 5-26. The magnitude of the parallel ohmic impedance does not change much with changes in the distance between

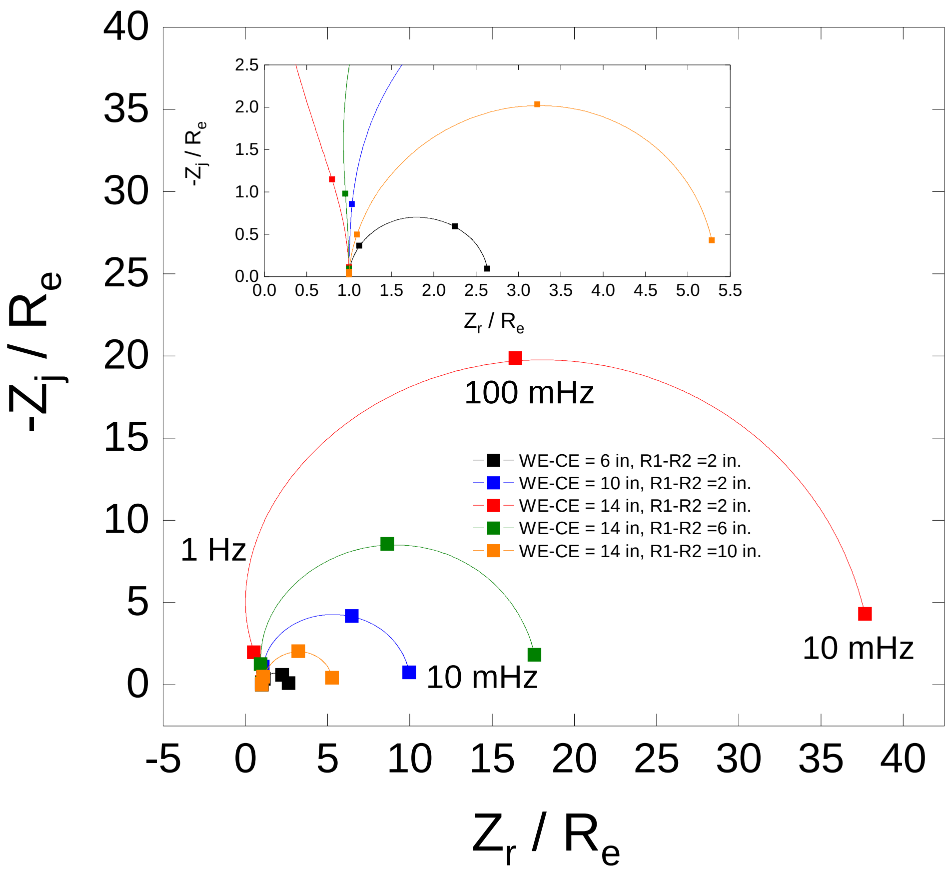

Figure 5-28. The simulated indirect impedance scaled by the ohmic resistance with electrode spacing as a parameter. Three simulations were performed for changes in reference electrode spacing and the other three were for changing the spacing between the working and counter electrode.

the working and counterelectrodes indicating that the parallel component of the ohmic impedance is most sensitive to the distance between the reference electrodes.

The overall indirect impedance is shown in Figure 5-28 scaled by the ohmic resistance for various electrode configurations to determine which electrode configuration yields the least amount of frequency dispersion. The most frequency dispersion is observed when the distance between the working and counter electrode is much larger than the distance between the two reference electrodes. The least amount of frequency dispersion is observed when the electrodes were equally spaced out at a distance of 2 in. The indirect impedance would also change as the depth of the steel from the electrodes changes. However, if the electrode are placed such that the distance between each electrodes is uniform and that distance is close to the depth of the steel the frequency dispersion will be minimal for systems with only one steel strand.

5.3.6 Sensitivity to Steel Polarization Resistance

Simulations were performed in which the steel polarization resistance was increased to determine the sensitivity of the indirect impedance to the steel corrosion state. The variation in the steel and grout interfacial impedance is shown in Figure 5-29 with the polarization resistance as a parameter. The capacitance was held constant. As the polarization resistance is increased, the interfacial impedance becomes more capacitive. The corresponding indirect impedance is shown in Figure 5-30 in Nyquist format. The indirect impedance increases as the polarization resistance of the steel increases showing that the indirect impedance is sensitive to the steel condition.

The overall goal is to be able to measure the indirect impedance and somehow determine the interfacial impedance such that the corrosion rate may be estimated. The series and parallel ohmic impedance contributions to the indirect impedance makes the extraction of the interfacial impedance difficult. However, if these parameters can be estimated from the geometry of the system, estimating the steel polarization resistance may be feasible. The series and parallel ohmic impedances were calculated as a function of steel polarization resistance to determine how dependent the ohmic contribution of the indirect impedance is on the steel impedance. The series ohmic impedance is shown in Figure 5-31 with the polarization resistance as a parameter. As the polarization resistance increases, the series ohmic impedance also increases and becomes more inductive. However, the high-frequency limit does not change. The parallel ohmic impedance is shown in Figure 5-32 with the polarization resistance as a parameter. As with the series ohmic impedance, the parallel component also increases as the polarization increases. However, the low-frequency limit of the real part of the parallel ohmic impedance is more well defined. The high-frequency limit of the parallel ohmic impedance also does not change. Since the ohmic components of the indirect impedance are functions of

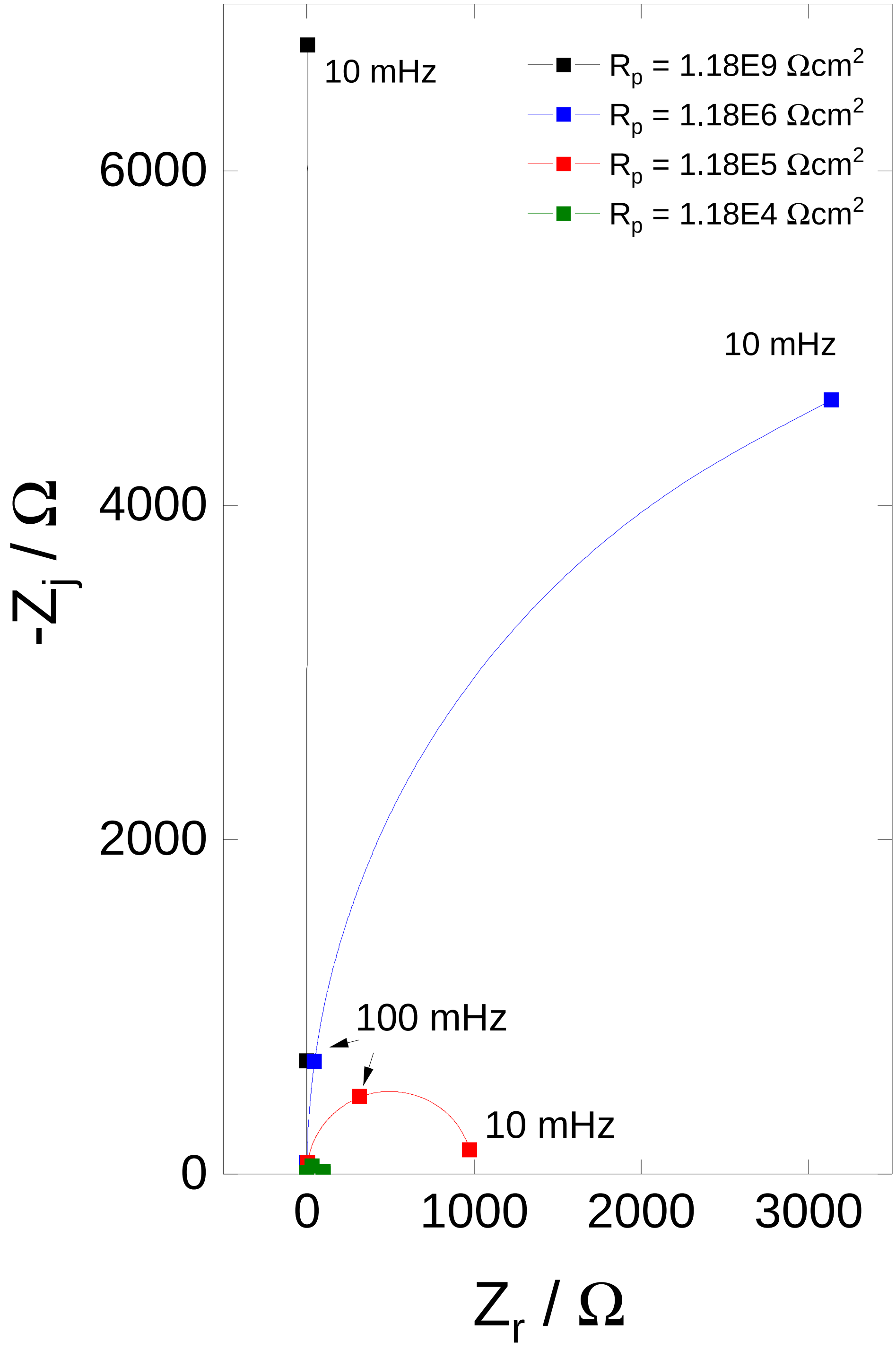

Figure 5-29. The interfacial impedance for a circuit with R_p in parallel with C_0 with R_p as a parameter.

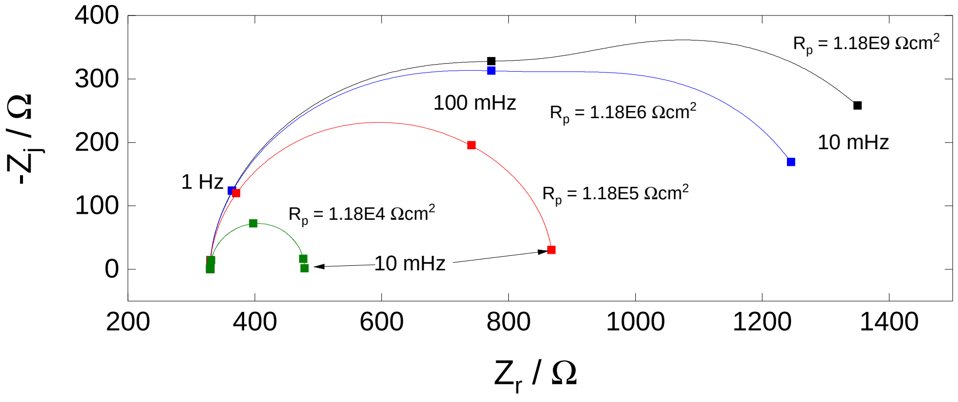

Figure 5-30. The simulated indirect impedance in Nyquist format with R_p as a parameter.

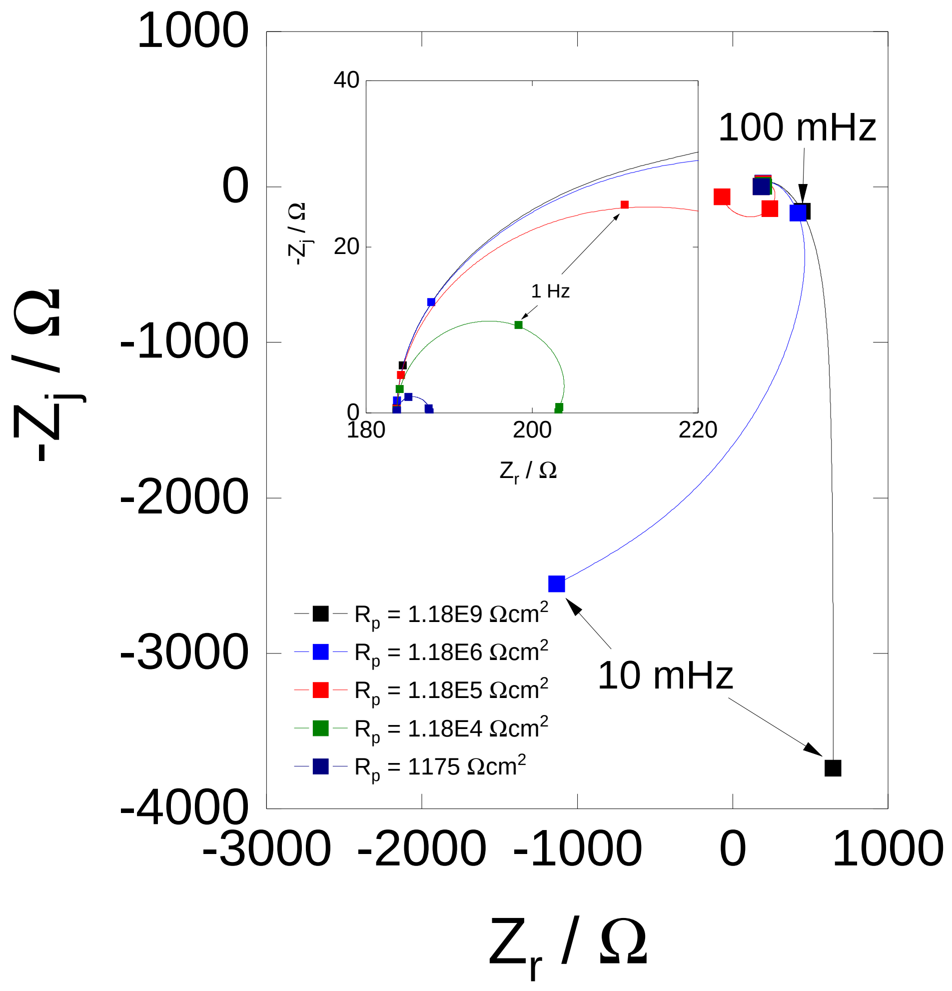

Figure 5-31. The series ohmic impedance in Nyquist format with R_p as a parameter.

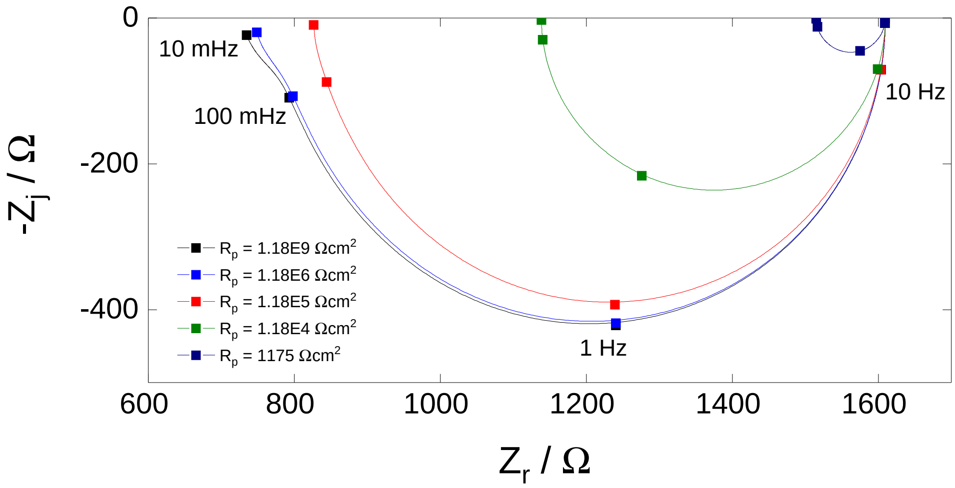

Figure 5-32. The parallel ohmic impedance in Nyquist format with R_p as a parameter.

the steel interfacial impedance, it would be difficult to predict these parameters solely from the geometry. Nevertheless, since the high-frequency limits are not dependent on the interfacial impedance, the ohmic resistance of the indirect impedance coupled with knowledge of the system geometry may be used to estimate the high-frequency limits of the series and parallel ohmic impedances.

CHAPTER 6
FEASIBILITY OF INDIRECT IMPEDANCE FOR POST-TENSIONED TENDONS

This chapter presents experimental results from indirect impedance measurements performed on an extracted tendon section from the Ringling Causeway Bridge as well measurements performed on the Texas A&M mock bridge section. A preliminary analysis was done to estimate the polarization resistance of the steel by fitting the data with a simple equivalent circuit. However, as was shown in the previous chapter, the polarization resistance of the steel is significantly overestimated using this method. Simulations of a tendon with the same geometry and steel placement as one of the tendons from the Ringling Causeway Bridge were performed to compare with experimental results.

6.1 Methods

The external post-tensioned tendons on the Ringling Causeway Bridge showed signs of corrosion fewer than 7 years after construction. The tendons that were replaced were cut into 3 or 4 ft. sections and stored at the FDOT State Materials Office. Indirect impedance measurements were performed on one of the sections that showed corrosion. An image of the cross-section is shown in Figure 6-1. The tendon contained 22 strands of steel which are randomly dispersed. There were visible signs of grout segregation and corrosion of one of the steel strands. Measurements were performed at 6 different locations around the tendon to determine if corrosion could be detected.

The external tendons on the Texas A&M mock bridge, shown in Figure 6-2, were constructed with various levels of corrosion. Corrosion was induced on the steel by submerging parts of the steel strands in an HCl bath solution prior to constructing the tendons. Some of the strands were severed completely and the ends were submerged into the acidic solution. After construction, the tendons and the bridge itself were discretized into 1 ft. sections and labeled alphabetically. Each tendon location specification included the tendon number as well as the section designation (i.e., 13-JK). Indirect impedance measurements were performed at locations in which all the steel strands were severed

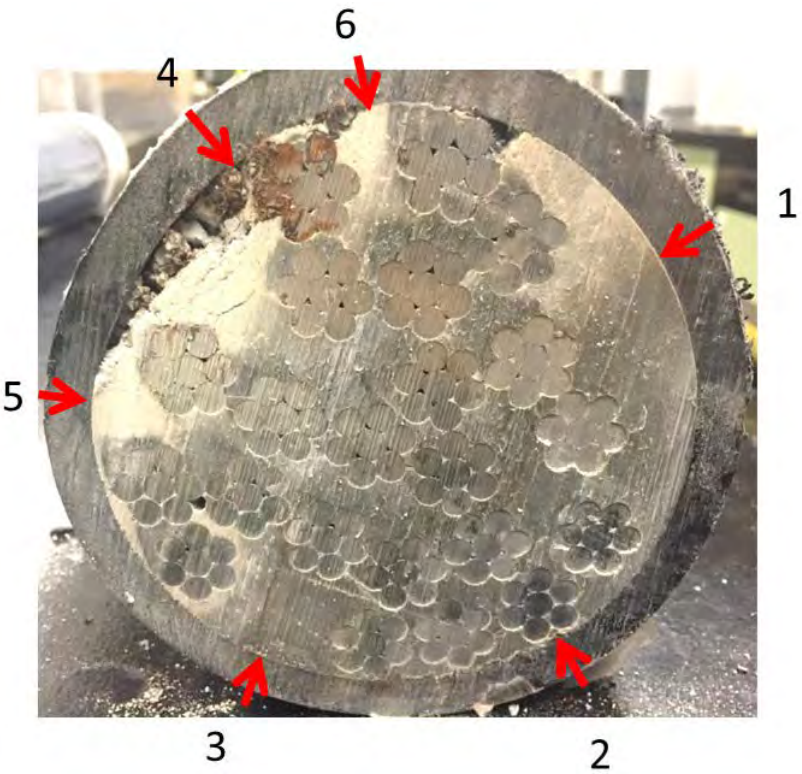

Figure 6-1. The cross-section of the Ringling Bridge tendon. The numbers indicate the locations of the electrodes.

with corroded ends, the steel strands were partially corroded, or all the strands were not corroded.

The experimental setup is shown in Figure 6-3 with the leads of the potentiostat connected to the electrodes. Four small holes were drilled into the HDPE duct to provide access to the grout. Dimensionally stable 0.5 cm diameter titanium rods coated in iridium-oxide were inserted into the holes and used as the electrodes. An in-house conductive gel consisting of a 1M sodium sulphate solution and carboxyl-methyl cellulose as a polymer gelling agent was used to make an electrical connection between the electrode and the grout. Impedance measurements can be taken by either modulating potential, referred to as potentiostatic modulation, or current, referred to as galvanostatic modulation. Potentiostatic modulation was found to be more reproducible and less noisy than galvanostatic modulation measurements. The impedance was measured with a Gamry reference 600 potentiostat over a range of frequencies. Real-time Lissajous

Figure 6-2. An image of the inside of the mock bridge built at Texas A&M.

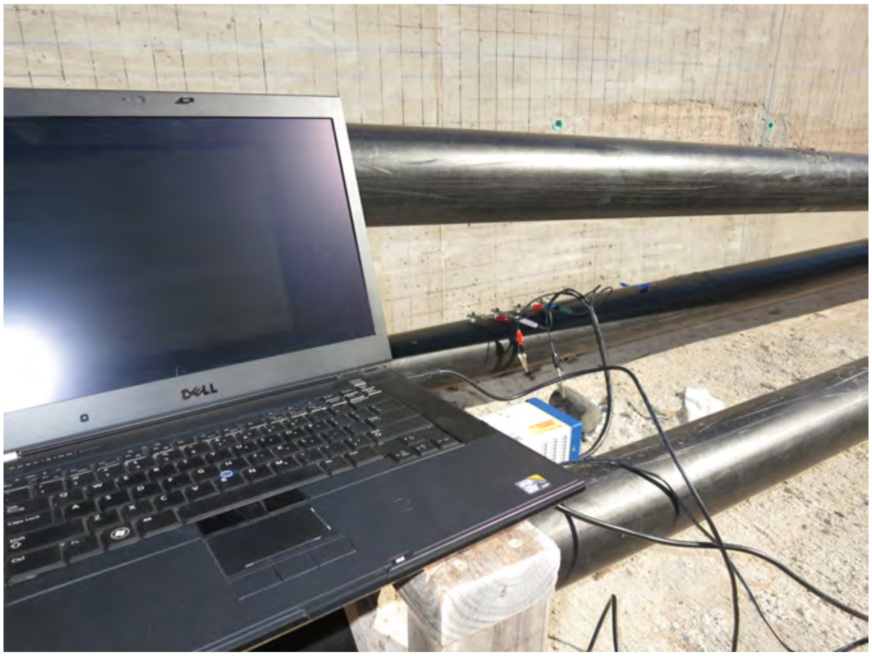

Figure 6-3. Experimental setup of the indirect impedance measurement. Photograph taken at the Texas A&M mock bridge. The Gamry Reference 600 potentiostat is the white/blue box in the center of the photograph.

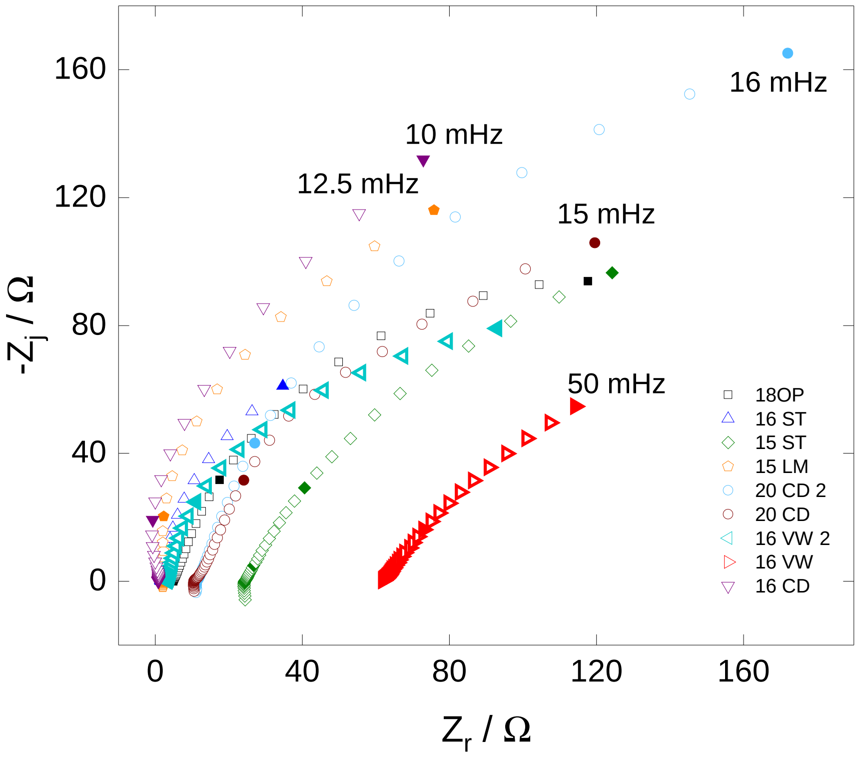

Figure 6-4. Experimental impedance in Nyquist format measured at different sections of the Texas A&M bridge tendons.

plots are displayed on the computer screen while measuring each frequency. After the measurements were performed, the holes were sealed by using HDPE welding technique.

6.2 Experimental Results & Analysis

Results are presented for impedance measurements performed on tendons constructed for the mock bridge section at Texas A&M as well as tendons extracted from the ringling causeway bridge. Finite element simulations were performed for a model which included the geometry of one of the tendons extracted from the Ringling bridge to assess the influence of the placement.

6.2.1 Texas A&M Mock Bridge

Results from the Texas A&M mock bridge are presented in Figure 6-4 for different locations as marked on the bridge. The indirect impedance is a function of the grout resistivity, the steel-grout interfacial impedance, and the location of the steel strands. Measurements were taken at the top of the tendon, unless the designation ends in 2 in which they were taken along the side. Corrosion associated with segregation of grout is most likely to occur near the top of the tendon since the grout near the top will have a higher conductivity. If there is a steel strand located near the electrodes, the real impedance will be negative at high frequencies due to the potential distribution, as is the case for location 16 CD. The high-frequency limit of the real impedance represents the ohmic resistance which can be associated with the resistance of current flow between the grout and the steel. The ohmic resistance is also a good measure of the depth of the steel. The significantly larger ohmic resistance measured at section 16 VW may be attributed to properties of the grout, such as voids.

Sections 16 VW and 16 ST had the smallest impedance values. The smaller impedance values suggest that corrosion was present. The indirect impedance for section 16 VW is shown separately in Figure 6-5. The measurement was fit with a simple circuit with a series and a parallel resistor accounting for the ohmic contribution and the steel impedance was expressed as a R_pC_0 circuit where R_p is the polarization resistance of the steel which is inversely related to the corrosion rate. Based on the circuit fitting $R_p = 292.9\Omega$. The figure inset shows the high frequency behavior. The results show a very small high frequency capacitive loop which overlaps the lower frequency data and may be a sign of corrosion. The indirect impedance for section 16 ST is shown separately in Figure 6-6. The high–frequency behavior for section 16 ST shows an inductive feature and significant high–frequency noise which has not been observed in our bench-top work or numerical simulations. The circuit did not fit the impedance well but R_p was estimated to be 316.5 Ω.

6.2.2 Ringling Causeway Bridge

The indirect impedance results from the Ringling Bridge tendon are shown in Figure 6-7. The numbers correspond to the location of the measurement shown in Figure 6-1. Measurements could not be made at location 2 because the steel strand was exposed from the grout when the holes were drilled. The smallest impedance was found for the location

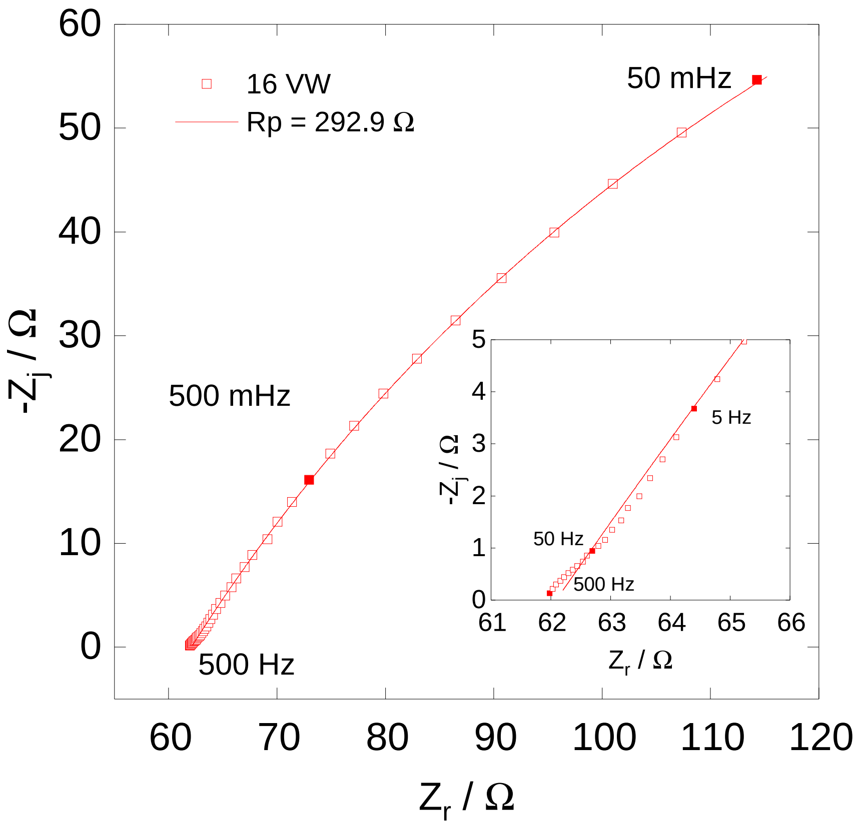

Figure 6-5. Experimental impedance in Nyquist format measured at location 16 VW of the Texas A&M mock bridge tendons.

of the corroded strand, shown as number 4 in Figure 2. A smaller impedance is expected for corroding steel as the impedance associated with corrosion of steel is smaller than the impedance associated with passivated steel.

The impedance at location 4 is shown separately in Figure 6-8. There are two capacitive loops which overlap, indicating the presence of two time constants. The higher-frequency time constant is associated with the corrosion reaction. The results indicate that corrosion can be detected if it is located directly beneath the array of electrodes. However, if the corrosion is located on a steel strand not near the measurement electrodes, it may go undetected.

An experiment was set up to try to overcome this obstacle. Instead of the electrodes being placed along the axis of the tendon, the electrodes were placed circumferentially in hopes that this electrode configuration was more sensitive to corrosion. The impedance

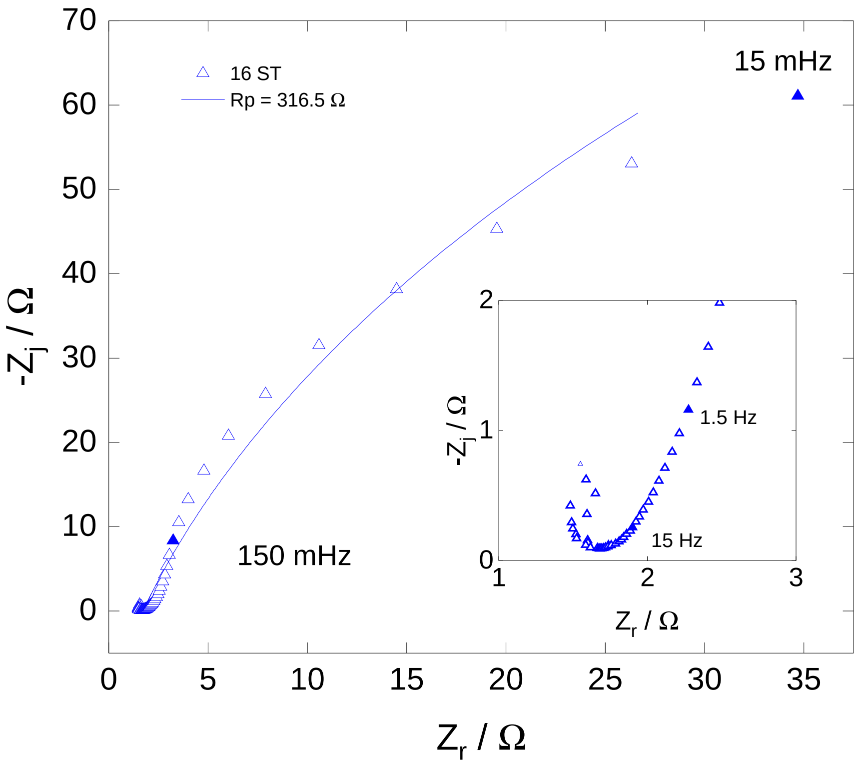

Figure 6-6. Experimental impedance in Nyquist format measured at location 16 ST of the Texas A&M mock bridge tendons.

results are shown in Figure 6-9 with the number designation indicating the location of the 4 electrodes corresponding to the diagram in Figure 6-1. The results are similar to the results in Figure 6-7 in that there is only one particular measurement, when the electrodes were at locations 5-4-6-1, that was able to detect the corrosion shown by the significantly smaller impedance. Therefore, the corrosion detection capabilities of the indirect impedance measurement are confined to cases where the corrosion is present right beneath the measurement electrodes.

6.3 Simulation Results

The geometry of the tendon extracted from the Ringling Bridge was modeled into a finite element stimulation . The model geometry is shown in Figure 6-10 including the same locations of electrode placement as the experimental case. Impedance simulations were performed with the electrode array placed along the axis at one of the designated locations. All of the steel strands were modeled to be passive. The simulated impedance

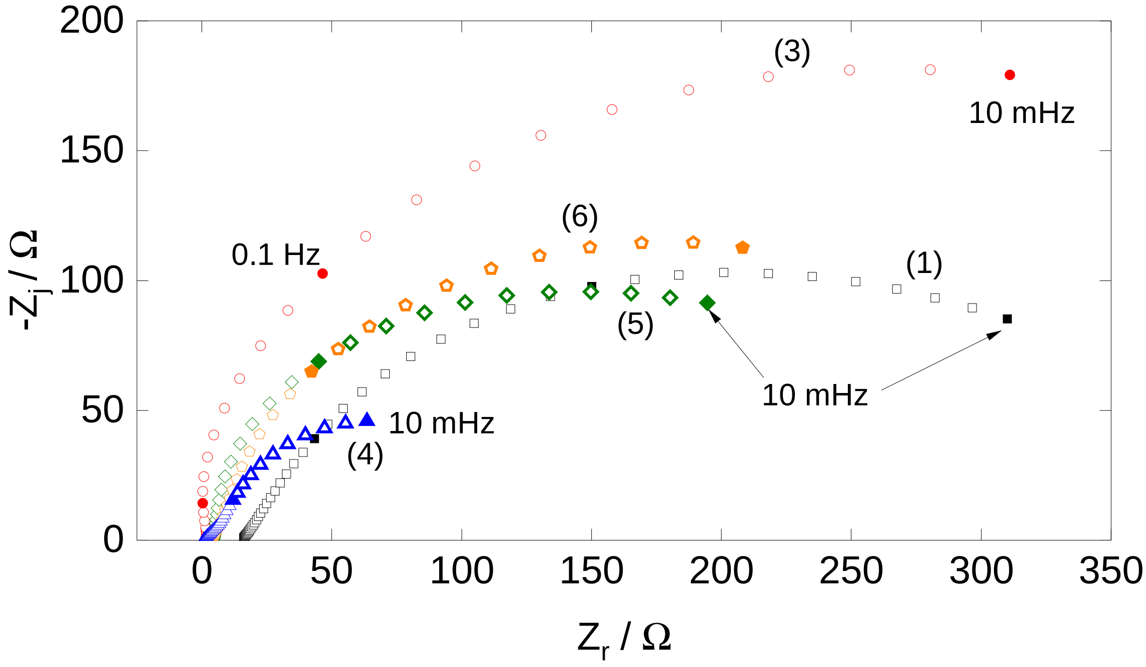

Figure 6-7. Experimental impedance in Nyquist format measured on an extracted tendon from the Ringling Causeway Bridge with the location of the electrodes as a parameter. The numbers in parentheses correspond to the location of the tendon shown in Figure 6-1.

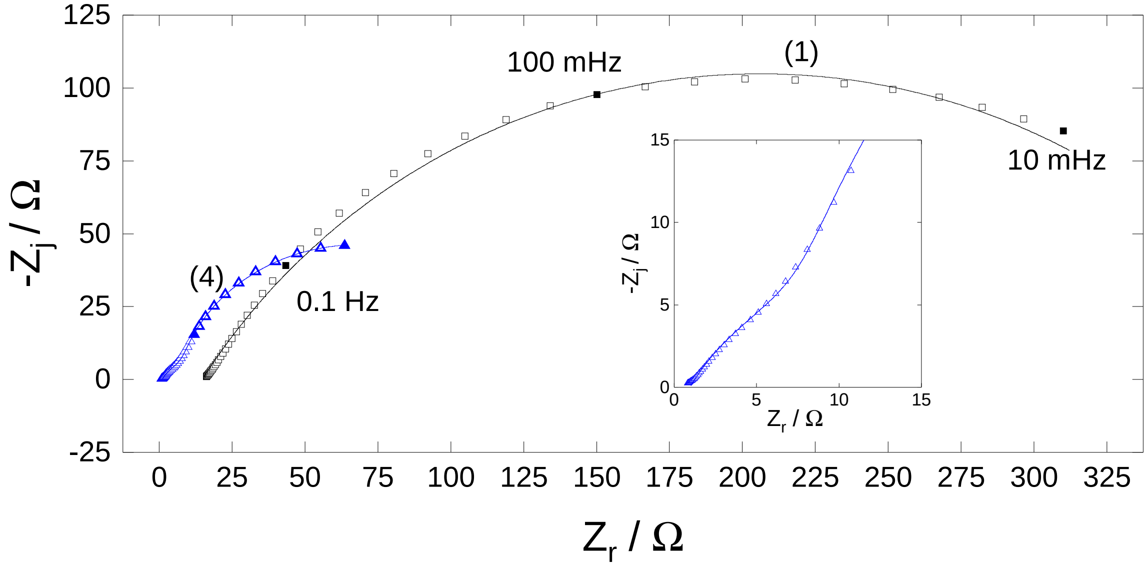

Figure 6-8. Experimental impedance in Nyquist format measured on an extracted tendon from the Ringling Causeway Bridge at location 4

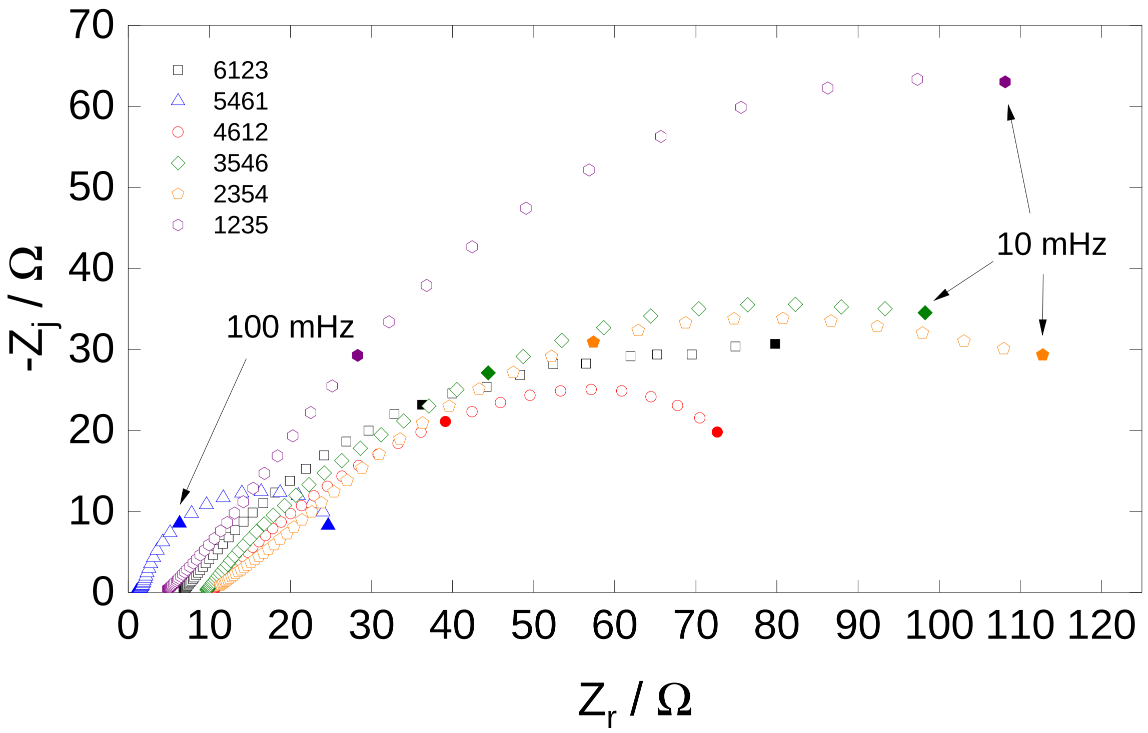

Figure 6-9. Experimental impedance in Nyquist format measured on an extracted tendon from the Ringling Causeway Bridge with the location of the electrodes as a parameter. The numbers in designation corresponds to the electrode locations described in Figure 6-1.

is presented in Figure 6-11 in Nyquist format with the location of the electrodes as a parameter. Due to the location of the steel strands in relation to the location of the electrode probes, the simulated impedance had inductive features at high frequencies. These simulations show that the indirect impedance is sensitive to steel position and it may be important to have a general sense of the location of the steel strands to formulate a reasonable estimate of the corrosion rate.

Simulations were also performed in which the electrodes were placed circumferentially around the tendon as was done experimentally. The simulations were done with all the steel strand set to a passive boundary conditions as well as a scenario in which one of the steel strands was corroding, shown by the location of the red circle in Figure 6-10. The simulation results are presented in Figure 6-12 for the all passive case, represented by the solid lines, and when one of the strands is corroding, shown by the dotted lines.

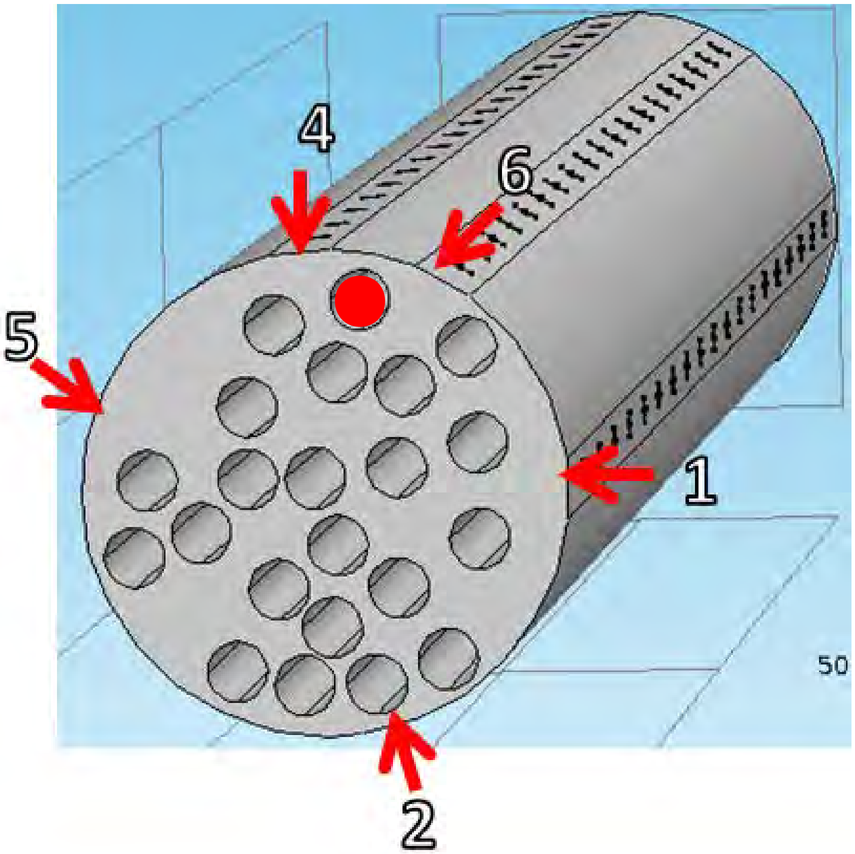

Figure 6-10. Finite element representation of the Ringling Bridge tendon shown in Figure 6-1.

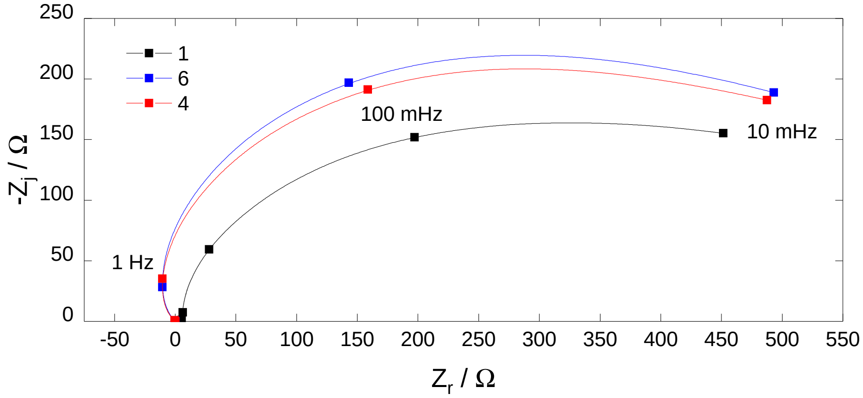

Figure 6-11. Simulated indirect impedance for a 2 ft. cylindrical tendon with 6 steel strands with corrosion state as a parameter.

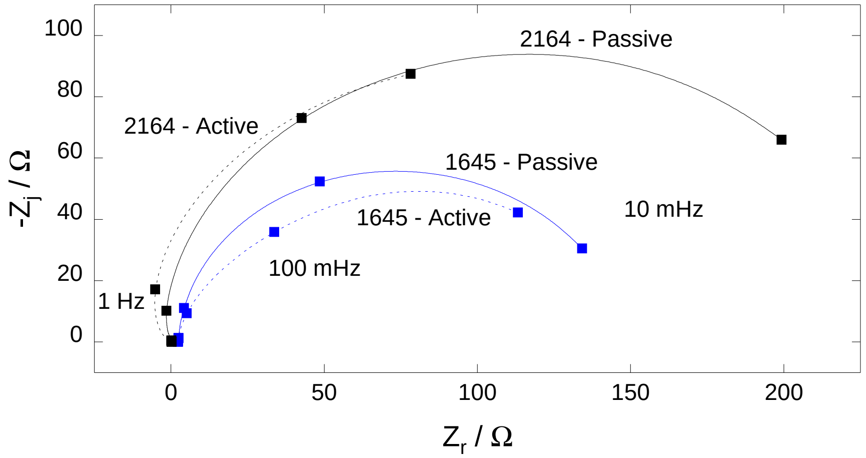

Figure 6-12. Simulated indirect impedance for a 2 ft. cylindrical tendon with 6 steel strands with corrosion state as a parameter.

When the electrode probes were placed at locations 1-6-4-5 the difference between the passive case impedance and the corroding case was not extreme. The difference was more pronounced when the electrode probes were placed at locations 2-1-6-4. When the electrodes are placed longitudinally along the tendon the indirect impedance measurement is most sensitive when the corrosion is directly beneath the working or counter electrode. The same is still true when the electrodes are placed circumferentially around the tendon.

6.4 Discussion

Through the experience of performing indirect impedance measurements on the Texas A&M mock bridge and the tendons extracted from the Ringling bridge, some difficulties were realized. If the electrodes are placed at a location where the steel is exposed from the grout, it is not possible to obtain an impedance measurement. If this occurs in the field, the electrode array should be shifted to a different location around the tendon. The results from the Texas A&M bridge did not show as much of the capacitive loop as the measurements taken from the Ringling tendon. In fact, the magnitude of the impedance also varied significantly between the two cases. This may be due to the use of different grouts which may have different material properties which poses a major challenge in devising a general interpretation procedure. Also, since the indirect impedance is a function of the steel location, which would be difficult to determine a priori, any analysis aimed at estimating a corrosion rate of the steel would have to include a way of accounting for this.

The experiments and simulations both showed that the indirect impedance is a highly localized technique as it is only capable of detecting corrosion or at least showing significant signs of corrosion if it is located directly beneath the working or counter electrodes. Otherwise, the measurement does not show qualitative signs of corrosion. There was no advantage to placing the electrodes circumferentially around the tendon instead of longitudinally. Therefore, if a measurement is taken at the top of the tendon and the corrosion occurs in the center, it will likely go undetected. However, corrosion was shown to occur in the locations of deficient grout formed at elevated locations of the tendon in cases where excess water was used to mix the grout.[63]

While there are many difficulties to the application of indirect impedance to corrosion detection in tendons, there are still clear advantages over existing technologies. The procedure for the indirect impedance measurement is relatively simple and does not require heavy equipment. Measurements are performed in approximately 20 minutes, and the holes that are drilled can be sealed if desired. The interpretation of the indirect impedance results is still a work in progress. Finite element simulations were used to determine the sensitivity of the indirect impedance to corrosion. We fully understand how the impedance of the grout contributes to overall impedance and with more research, a reliable method to estimating the corrosion rate may be achieved.

CHAPTER 7
INFLUENCE OF ROUGHNESS ON IMPEDANCE

Electrical circuits invoking constant–phase elements (CPE) are often used to fit impedance data arising from a broad range of experimental systems. The impedance for a blocking electrode showing CPE behavior may be expressed in terms of ohmic resistance R_e and CPE parameters α and Q as

$$Z = R_\mathrm{e} + \frac{1}{(\mathrm{j}\omega)^\alpha Q} \tag{7–1}$$

where ω is the angular frequency in units of s^{-1}. When $\alpha = 1$, the system is described by a single time–constant, and the parameter Q has units of capacitance; otherwise, Q has units of $\mathrm{s}^\alpha/\Omega\mathrm{cm}^2$ or $\mathrm{F}/\mathrm{s}^{(1-\alpha)}\mathrm{cm}^2$ [57].

While CPEs are commonly used to improve the fit to experimental impedance spectra, the explanation for their origin has been largely conjectural. Recently, Jorcin et al. [30] have proposed that the CPE could have, as an origin, a distribution of time constants through a film or along an electrode surface. They supported their hypothesis with local impedance measurements. An interpretation for CPE behavior caused by a normal distribution was developed in the form of a power–law distribution of resistivity.[24, 25] The power–law model approach has been used successfully to extract a film capacitance and associated parameters for a variety of systems, including oxides on steel,[58] human skin,[58, 74] and polymer coatings.[48] [51]

Brug et al. [12] developed an expression for the capacitance extracted from a CPE caused by a surface distribution of capacitance or charge transfer resistance. The Brug model was shown to apply for the apparent CPE behavior associated with geometry-induced nonuniform current and potential distributions on a disk electrode.[26, 27] As the geometry-induced CPE behavior appears only at high frequency,[28] the disk geometry cannot provide an explanation for CPE behavior caused by surface distributions that may extend over many decades of frequency.

Several other potential causes for surface CPE behavior have been proposed, including porous electrodes,[19, 40, 69] specific adsorption,[62] surface roughness,[35, 59] and even heterogeneity on an atomic scale.[68] Since 1950, electrode roughness emerged as a leading explanation for CPE behavior.

While roughness was initially considered to cause CPE behavior, recent work has questioned this premise. The objective of this work is to explore, by use of finite–element models, whether surface roughness could provide a valid physical explanation for CPE behavior associated with a surface distribution of time constants. An essential question in this analysis is whether electrochemical impedance spectroscopy measurements encompass the frequency at which roughness is expected to influence the impedance response.

7.1 Mathematical Development

The potential distribution within an electrolyte with uniform composition is governed by Laplace's equation,

$$\nabla^2\Phi = 0. \tag{7–2}$$

For the present work, axisymmetric cylindrical coordinates were used in which the potential was assumed to be independent of the angular coordinate.

The potential was separated into steady-state and oscillating components as

$$\Phi = \bar{\Phi} + \mathrm{Re}\left\{\tilde{\Phi}\mathrm{exp}(\mathrm{j}\omega t)\right\} \tag{7–3}$$

where $\bar{\Phi}$ represents the steady-state portion and $\tilde{\Phi}$ represents the complex oscillating portion that is a function of frequency and position but independent of time. The same relationship for the potential applied to the electrode can be expressed as

$$V = \bar{V} + \mathrm{Re}\left\{\tilde{V}\mathrm{exp}(\mathrm{j}\omega t)\right\} \tag{7–4}$$

For a capacitive system, the steady state potential is equal to zero; thus, only the oscillating component was calculated. At $r = 0$, for all y, the symmetry condition

$\partial\tilde{\Phi}/\partial y = 0$ applied. Far from the electrode, as $\sqrt{r^2+y^2} \to \infty$, $\tilde{\Phi} \to 0$. This condition places the counterelectrode infinitely far from the working electrode.

Following Newman [50] and Huang et al. [28], the electrode was assumed to be ideally polarized. The normal flux at the surface of the electrode was expressed as

$$i = C_0 \frac{\partial(V-\Phi_0)}{\partial t} = -\kappa \frac{\partial \Phi}{\partial y}\bigg|_{y=0} \tag{7–5}$$

where C_0 is the capacitance on the electrode surface, κ is the conductivity of the electrolyte, and Φ_0 is the potential outside the diffuse part of the electrode double layer.

The oscillating current density was converted to the frequency domain such that

$$\tilde{i} = \mathrm{j}\omega C_0(\tilde{V}-\tilde{\Phi}) \tag{7–6}$$

where $\tilde{V}$ is the potential perturbation at the electrode and $\tilde{\Phi}$ is the complex oscillating potential within the electrolyte.

Frequency or time-constant dispersion may occur for any electrochemical cell design that does not provide a uniform current distribution across the working electrode surface. This form of frequency dispersion may be referred to as geometry-induced frequency dispersion, in which the characteristic frequency at which time-constant dispersion is evident is inversely related to a characteristic length. A dimensionless frequency, K, may be defined as

$$K = \frac{\omega C_0 l_\mathrm{c}}{\kappa} \tag{7–7}$$

such that frequency dispersion is induced at $K \geq 1$. The corresponding characteristic frequency may be expressed as

$$f_\mathrm{c} = \frac{\kappa}{2\pi C_0 l_\mathrm{c}} \tag{7–8}$$

As the characteristic length increases, the frequency dispersion shifts to lower frequencies. Therefore, the characteristic length should be minimized to avoid frequency dispersion in experiments. In the case of a blocking disk electrode within an insulating plane, the characteristic length is the radius of the disk. Since the ohmic resistance of a disk electrode in units of $\Omega\mathrm{cm}^2$ is given by[49]

$$R_e = \frac{\pi r_0}{4\kappa} \tag{7–9}$$

it may be convenient to express the characteristic frequency as the ratio of the interfacial impedance and the ohmic resistance as

$$K = \frac{R_\mathrm{e}}{Z_0} \tag{7–10}$$

The interfacial impedance for a blocking electrode can be expressed as

$$Z_0 = \frac{1}{\omega C_0} \tag{7–11}$$

such that the dimensionless frequency is

$$K = \frac{\pi}{4}\frac{\omega C_0 r_0}{\kappa} \tag{7–12}$$

This formulation is convenient for a blocking disk electrode, however, it does not apply to other geometries such as a ring or a rectangle where the ohmic resistance is not proportional to the characteristic length. Therefore, for the sake of consistency, the appropriate formulation is the one presented by Huang et al.[28] in which the dimensionless frequency was defined to be

$$K = \frac{\omega C_0 r_0}{\kappa} \tag{7–13}$$

The inclusion of the $\pi/4$ factor does not affect significantly the prediction of the characteristic frequency but it is not applicable to other geometries other than the disk electrode.

The roughness of the electrode was quantified in terms of the roughness factor or rugosity, f_r, obtained by dividing the true polarizable area by the geometric area.[71] A smooth electrode has a roughness factor of unity; whereas, roughness factors much greater than unity may be attributed to porous electrodes. For a uniformly rough surface with

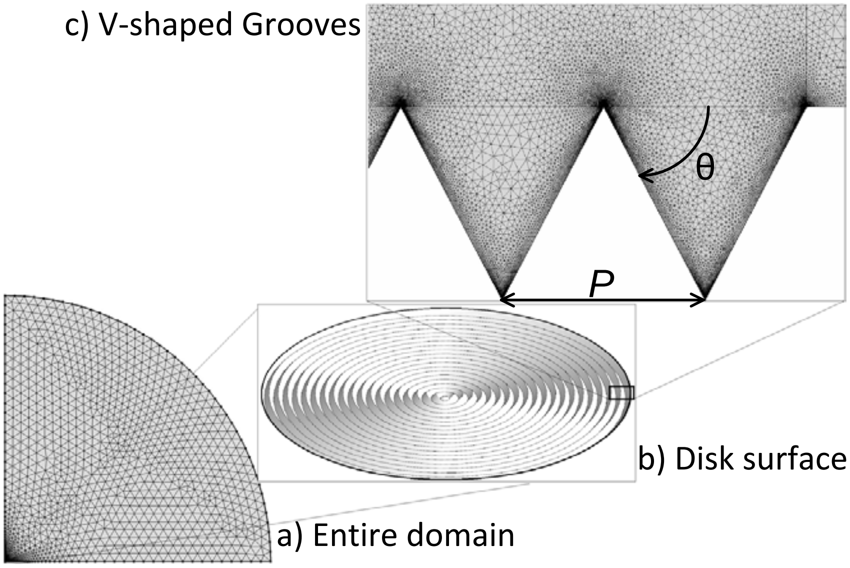

Figure 7-1. Schematic representation showing the finite-element mesh used for the disk electrode simulations: a) entire domain; b) grooved surface of the electrode; c) detail of the grooved electrode.

concentric V–shaped grooves, the roughness factor may be expressed as $f_\mathrm{r} = 1/\cos\theta$, where θ represents the contact angle between the rough surface and a smooth plane.

7.2 Impedance Calculations

Three disk electrode configurations were simulated, including a completely smooth electrode within an insulating plane, a rough electrode within an insulating plane, and a recessed rough electrode. The calculations were performed in axisymmetric cylindrical coordinates for a quarter of a circle domain, shown in Figure 10-3(a), which represents the electrolyte. The counterelectrode was located at $\sqrt{r^2+y^2} = 500$ cm, making the domain size at least 1000 times larger than the radius of the disk. A free triangular mesh was used with a greater density of elements near the working electrode. The grooved surface of the disk is shown in Figure 10-3(b), and an expanded view of the grooves is

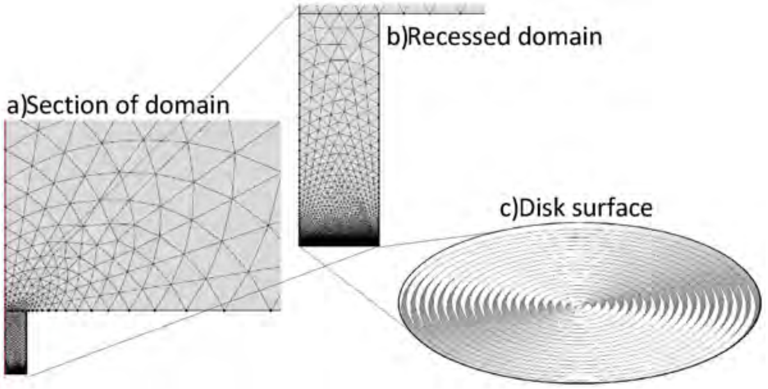

Figure 7-2. Schematic representation showing the finite-element mesh used for the recessed disk electrode simulations: a) portion of the domain emphasizing the recessed electrode; b) the recessed electrode; and c) detail of the grooved electrode.

shown in Figure 10-3(c). The angle θ used for the calculation of roughness factor is also shown in Figure 10-3(c).

The electrode was placed in the $y = 0$ plane centered at $r = 0$ such that the angle between the electrode surface and the insulating plane was 180 degrees. The corresponding primary current distribution approaches infinity at the periphery of the disk. A recessed electrode was configured such that the insulating plane was perpendicular to the electrode surface as shown in Figure 7-2. The depth of the recess was three times the disk diameter, ensuring that the primary current distribution was uniform across the electrode surface. A rough surface was simulated in both cases by adding concentric V–shaped grooves to the electrode surface, as is illustrated in magnified view in Figure 7-2(c). A rough recessed electrode was used to isolate the effect of the rough surface on the impedance; whereas, the rough electrode embedded within an insulating plane showed the coupled effect of the roughness and the nonuniform current distribution associated with the disk geometry.

7.3 Results and Discussion

The results of impedance simulations are presented to show the influence of surface roughness on electrodes embedded within an insulating plane. Results from a recessed

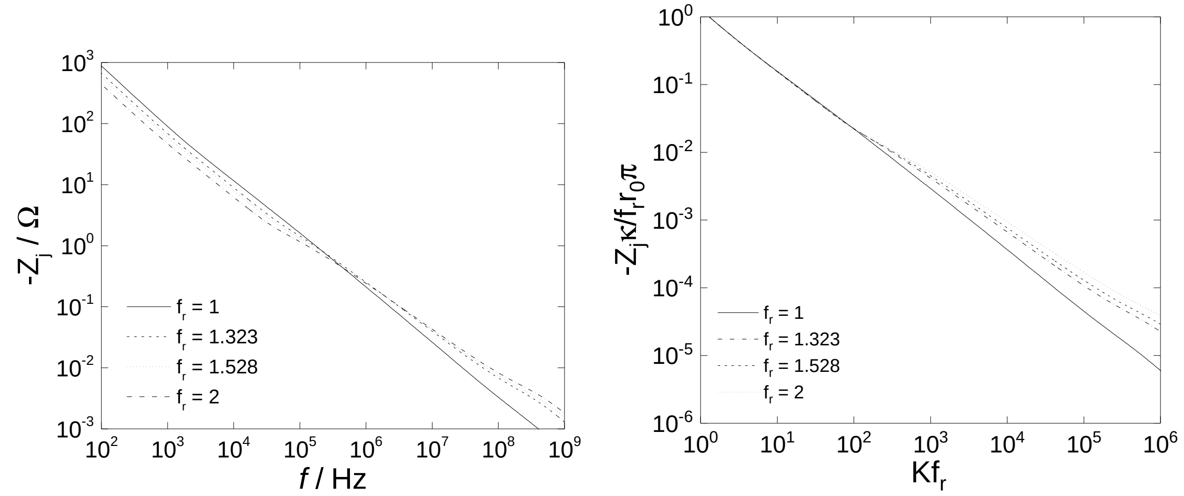

A

B

Figure 7-3. Imaginary part of the calculated global impedance for a rough disk electrode with roughness factor as a parameter: a) dimensional impedance as a function of frequency; b) dimensionless impedance as a function of dimensionless frequency Kf_{r}.

electrode are then used to distinguish between the effect of the roughness and the influence of disk geometry.

7.3.1 Influence of Roughness on a Disk Electrode Within an Insulated Plane

The impedance of smooth and rough disk electrodes within an insulating plane was simulated to show the coupled effect of surface roughness and nonuniform current distributions caused by disk geometry. The calculated imaginary part of the impedance is provided in Figure 7-3A as a function of frequency with the roughness factor as a parameter. The radius was 0.24 cm. The simulated imaginary impedance for the rough electrodes at low frequencies was smaller than the impedance of the smooth electrode and decreased as the roughness factor was increased. The reduced impedance of the electrode could be attributed to the larger polarizable surface area. Conversely, the impedance of the rough electrode was larger than the impedance of the smooth electrode at high frequencies.

The imaginary part of the simulated global impedance, adjusted for the roughness of the electrode, is provided in Figure 7-3B as a function of dimensionless frequency. The dimensionless frequency for a rough–disk electrode can be expressed as

$$Kf_{\mathrm{r}} = \frac{\omega C_0 f_{\mathrm{r}} r_0}{\kappa} \tag{7–14}$$

The impedance is expressed as $Z_{\mathrm{j}}\kappa/f_{\mathrm{r}}r_0\pi$ where the impedance Z_{j} is scaled by unit area with units of Ω-cm^2. The total surface area of a rough electrode is $\pi f_{\mathrm{r}} r_0^2$. The use of the roughness factor in the scaling is confirmed by the superposition of the impedance at low frequencies where the current reaches all parts of the rough surface.

Bode phase plots are often used to represent impedance data. The phase was calculated from the real and imaginary parts of the impedance as

$$\varphi = \arctan\frac{Z_{\mathrm{j}}}{Z_{\mathrm{r}}} \tag{7–15}$$

The magnitude and phase angle corresponding to the impedance presented in Figure 7-3 are expressed in Figure 7-4 as functions of frequency with the roughness factor as a parameter. The phase angle was zero at the high-frequency limit and -90° at the low–frequency limit. The inflection point corresponded to the characteristic frequency. One of the disadvantages of the Bode phase plot is that the contribution of the ohmic resistance may conceal important features. The ohmic-resistance-corrected modulus and phase angle,[56]

$$|Z_{\mathrm{adj}}| = \sqrt{(Z_{\mathrm{r}} - R_{\mathrm{e}})^2 + Z_{\mathrm{j}}^2} \tag{7–16}$$

and

$$\varphi_{\mathrm{adj}} = \arctan\frac{Z_{\mathrm{j}}}{Z_{\mathrm{r}} - R_{\mathrm{e}}} \tag{7–17}$$

respectively, are shown in Figure 7-5. The ohmic–resistance–corrected phase angle, in particular, emphasizes the phase response of the electrode. The ohmic resistance used in equations 7–16 and 9–15 was obtained from the high-frequency limit of the calculated impedance. The adjusted–phase angle showed two deviations from an ideal capacitive response. However, the distinction between the two time constants was not clear.

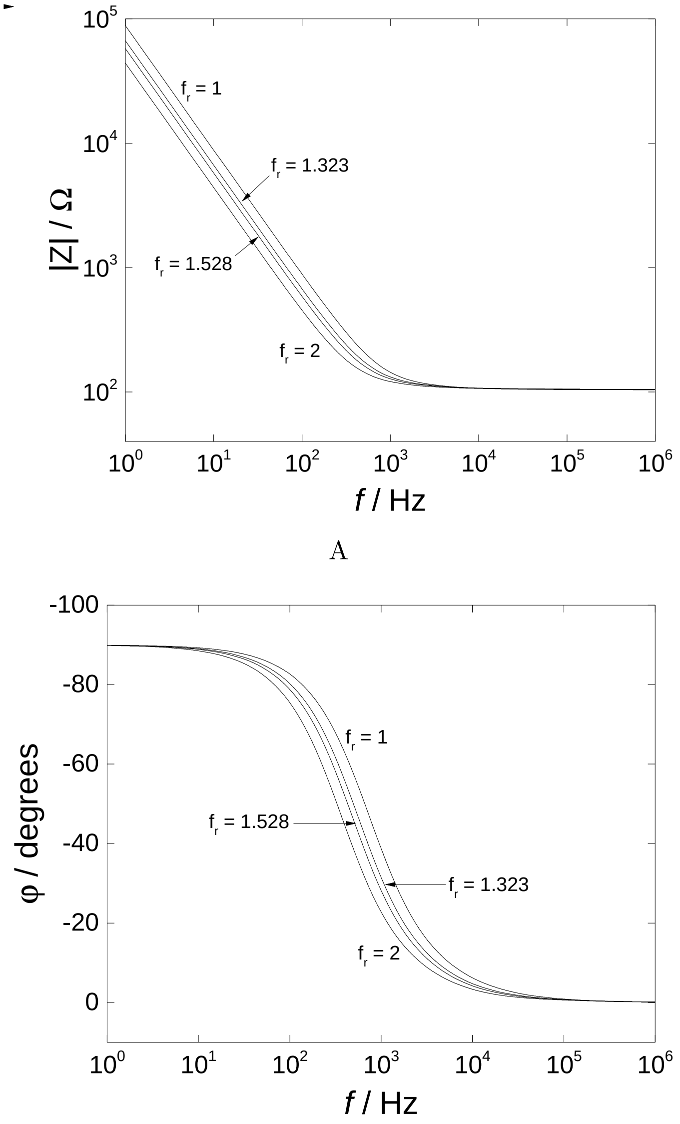

A

B

Figure 7-4. Calculated global impedance as a function of frequency for a rough disk electrode with roughness factor as a parameter: a) magnitude; b) phase.

A clearer separation of features was obtained by use of an imaginary–impedance–derived–phase angle, which is based only on the imaginary part of the impedance, i.e.,

$$\varphi_{\mathrm{dZj}} = \frac{\mathrm{dlog}(Z_{\mathrm{j}})}{\mathrm{dlog}(f)} \times 90^{\circ} \tag{7–18}$$

The derivative of the logarithm of the imaginary impedance with respect to the logarithm of the frequency, used previously to estimate the exponent for a constant-phase element,[56]

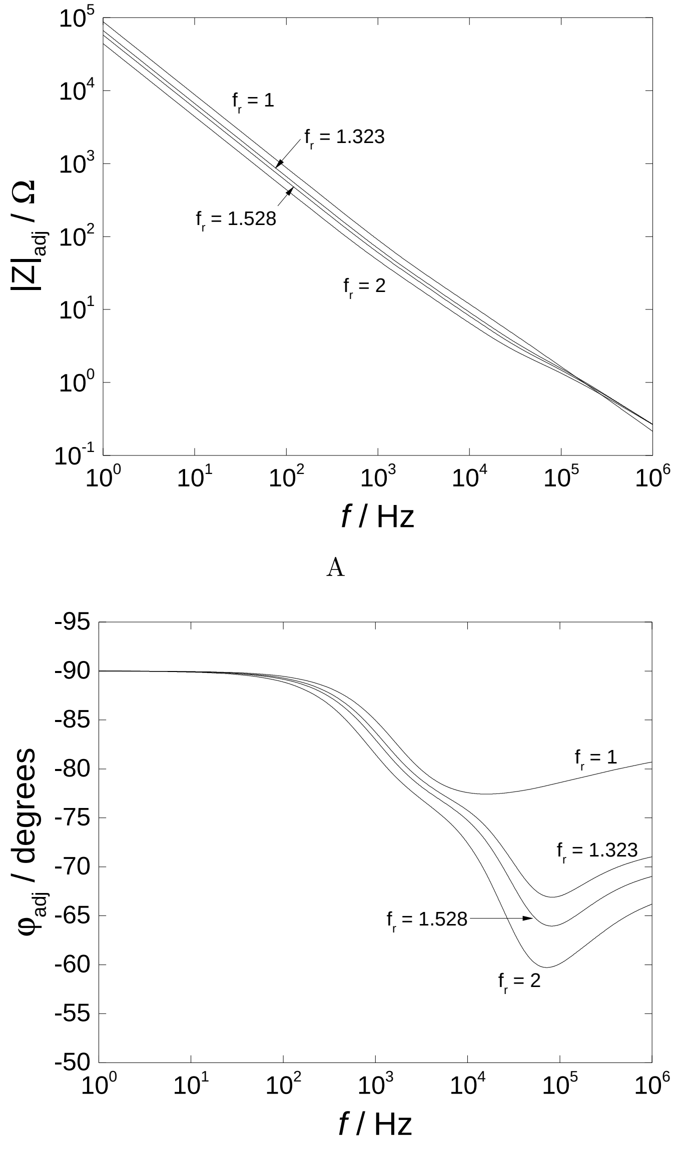

A

B

Figure 7-5. Calculated global impedance as a function of frequency for a rough disk electrode with roughness factor as a parameter: a) ohmic–resistance–corrected magnitude; b) ohmic–resistance–corrected phase angle.

is expressed here as a phase angle. A comparison between the imaginary–impedance–derived phase angle and the adjusted phase angle is presented in Figure 7-6 for a roughness factor of 2 and a roughness period of 40 μm. The imaginary–impedance –derived phase angle shows clearer delineation between the two deviations as compared to the ohmic–resistance–corrected phase angle.

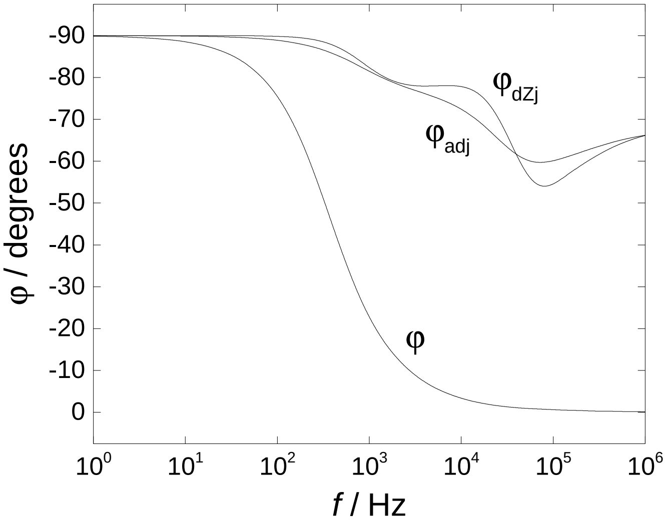

Figure 7-6. Phase angles obtained from equations 7–23, 9–15, and 8–10 for the impedance presented in Figure 7-3 for a rough disk electrode as a function frequency. The roughness factor was $f_r = 2$ and the roughness period was $P = 40$ μm.

The imaginary–impedance–derived–phase angle is presented in Figure 7-7A as a function of frequency with the roughness factor as a parameter. The results for the smooth electrode showed non–ideal behavior at frequencies greater than 800 Hz due to the nonuniform current distribution caused by the electrode configuration [27]. For the rough electrodes, two distinct deviations from ideal behavior were observed. The lower-frequency deviation for a 0.24 cm radius electrode with a roughness factor of 2 occurred at frequencies equal to and greater than 300 Hz, which is 500 Hz less than that observed for the smooth electrode. The magnitude of the difference in frequency between the lower-frequency deviation of the rough electrode compared to the smooth electrode is proportional to the roughness factor. The higher-frequency deviation occurred at roughly 20 kHz.

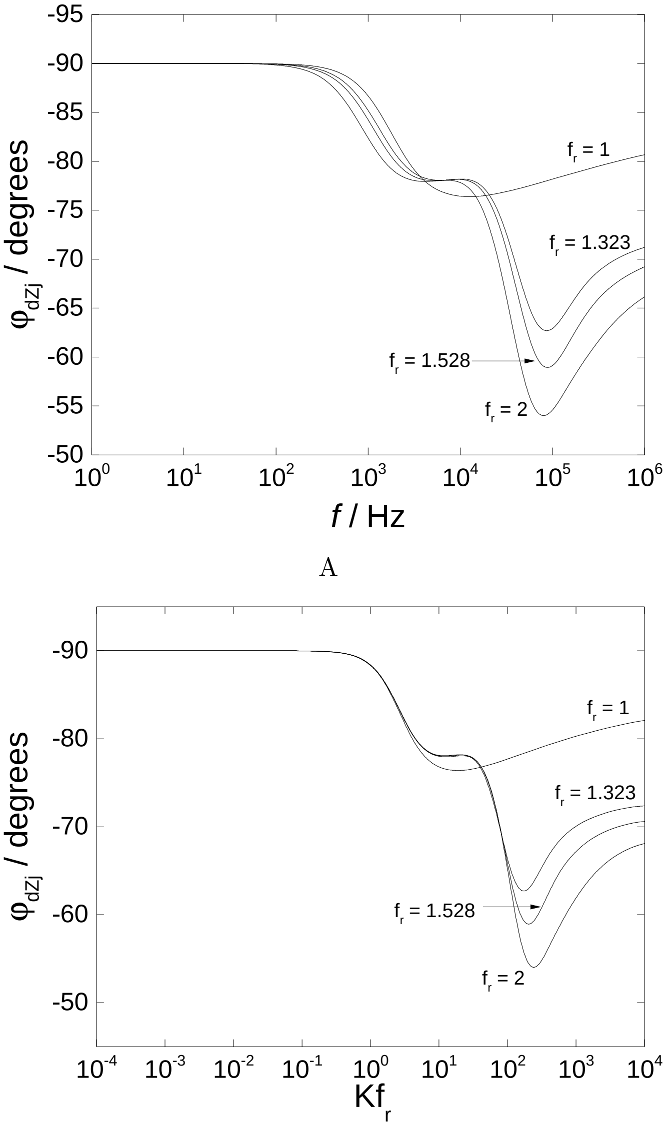

A

B

Figure 7-7. Imaginary–impedance–derived–phase angle calculated from the impedance presented in Figure 7-3 for a rough disk electrode: a) Imaginary–impedance–derived–phase angle as a function of frequency; b) Imaginary–impedance–derived–phase angle as a function of dimensionless frequency Kf_r.

The characteristic frequency at which the current and potential distributions on a smooth disk electrode within an insulating plane begin to influence the impedance response may be expressed as [28]

$$f_{\mathrm{c}} = \frac{\kappa}{2\pi C_0 r_0} \tag{7–19}$$

For a rough electrode, the radius must be modified to include the effect of surface roughness. Therefore, the characteristic frequency at which a rough disk electrode influences the impedance response is expressed as

$$f_{\mathrm{c}} = \frac{\kappa}{2\pi C_0 f_{\mathrm{r}} r_0} \tag{7–20}$$

which is slightly smaller than the characteristic frequency associated with the influence of the nonuniform current distributions. Equation (7–20) accounts for the coupled effect of surface roughness and disk electrode geometry. The dimensionless results, presented in Figure 7-7B in which the characteristic length included the roughness factor, showed that the initial deviation could be attributed to the coupled effect of disk geometry and surface roughness as it occurred at $\mathrm{K}f_{\mathrm{r}} = 1$. The magnitude of the higher–frequency deviation increased as the roughness factor increased, but the characteristic frequency was not altered. This provides indication that the higher–frequency deviation may also be dependent on the roughness factor.

A series of simulations were performed in which the depth and period of the roughness was increased such that the roughness factor was fixed at 2, as illustrated in Figure 7-8. The imaginary–impedance–derived–phase angle corresponding to the impedance response on electrodes with various roughness periods is presented in Figure 7-9A in which the dimensionless frequency was modified by the roughness factor. The results show that as the roughness depth increased, the characteristic frequency of the roughness decreased, but the magnitude of the deviation from ideality remained consistent. Also, the portion of the plot that is superposed is the low–frequency deviation

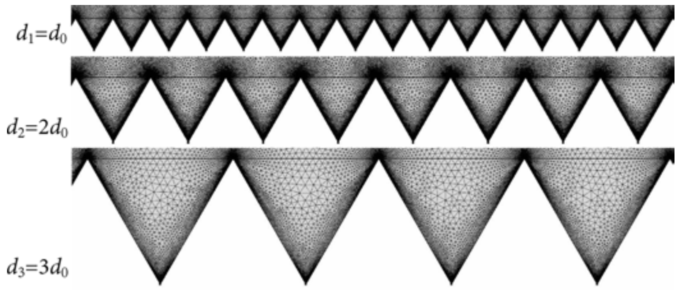

Figure 7-8. Schematic representation showing the manner in which the roughness period was varied for a fixed roughness factor equal to 2. The three configurations have the same surface area.

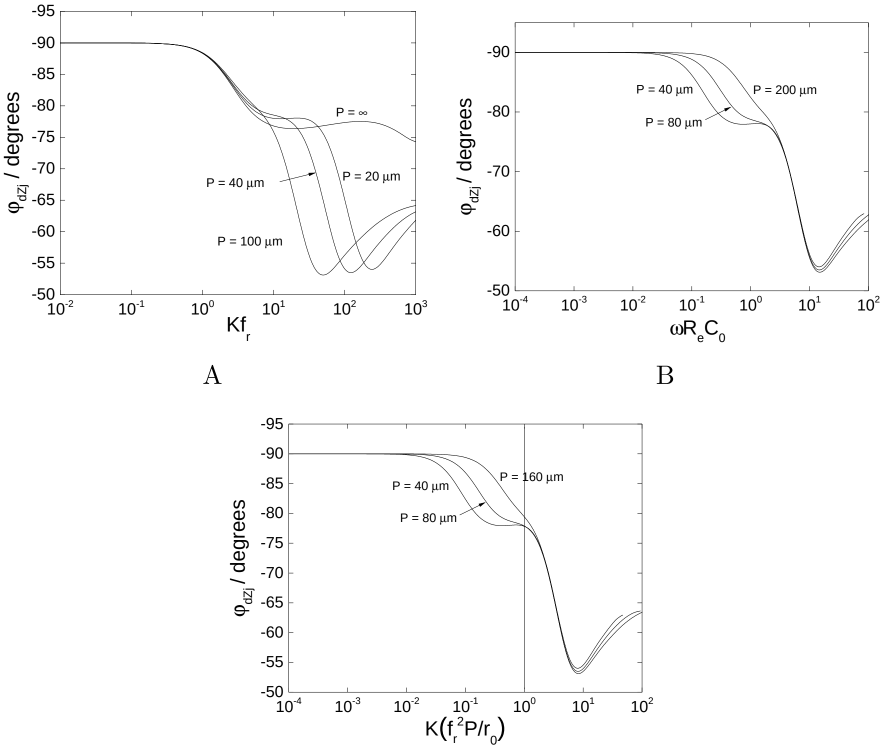

A

B

C

Figure 7-9. The imaginary–impedance–derived–phase angle calculated from impedance simulations of a rough disk electrode within an insulating plane with the roughness period as a parameter and the roughness factor held constant: a) Phase angle as a function of frequency modified by the roughness factor; b) Phase angle as a function of $\omega R_e C_0$ in which the ohmic resistance was calculated from recessed electrode simulations (see equation 7–21); c) Phase angle as a function of dimensionless frequency derived from the approximated ohmic resistance.

representative of the coupled effect of the nonuniform current distribution due to the disk geometry and the surface roughness.

The results of Figure 7-9A are provided in Figure 7-9B as a function of the dimensionless frequency, Equation 7–10. The ohmic resistance associated with the rough grooves was determined from the frequency at which dispersion occurs which can be obtained from recessed electrode simulations as

$$R_e = \frac{1}{2\pi f_c C_0} \tag{7–21}$$

In this case, the superposition occurred at the higher frequency deviation, indicating that the ohmic resistance obtained from recessed electrode simulations is also applicable to disk electrodes within an insulating plane.

The ohmic resistance of the grooves is dependent on the shape of the grooves and therefore can only apply to a particular geometry. An approximation of the ohmic resistance of the rough grooves that is general enough to be independent of geometry was observed to be a function of the roughness factor and the width or period of the grooves expressed as

$$R_e \approx \frac{f_r^2 P}{\kappa} \tag{7–22}$$

The corresponding dimensionless frequency may be expressed as

$$K f_r^2 P / r_0 = \frac{\omega C_0 f_r^2 P}{\kappa} \tag{7–23}$$

in which the characteristic length of surface roughness is expressed as

$$l_{c,rough} = f_r^2 P \tag{7–24}$$

according to equation 7–7. The imaginary—impedance—derived phase angle is shown in Figure 7-9C as a function of the dimensionless frequency corresponding to the approximated ohmic resistance. The approximation of the ohmic resistance showed the same superposition of the higher frequency deviation as did the results in Figure 7-9B in which the true ohmic resistance was used. Similar superposition was observed for simulations of grooves separated by smooth surfaces and for rectangular indentations. While it is interesting that the ohmic resistance associated with the rough grooves somehow corresponds to the dimensionless frequency, the most significant finding is the characteristic length of the surface roughness which directly explains the frequency at which dispersion is observed. More work will need to be done to fully understand the relationship between ohmic resistance and the characteristic length in regards to frequency dispersion.

7.3.2 Influence of Surface Roughness on a Recessed Electrode

Simulations were performed on a rough recessed electrode to isolate the effect of the surface roughness from that of the disk geometry. The imaginary–impedance–derived phase angle, presented in Figure 7-10A as a function of dimensionless frequency with the roughness period as a parameter, shows that the frequencies at which deviation from an ideal response occurred decreased as the depth of the roughness increased. The length scale used to make the frequency dimensionless was the product of the roughness factor and the radius of the disk.

The imaginary–impedance–derived–phase angle is presented in Figure 7-10B as a function of the dimensionless frequency that is based on the a characteristic dimension $f_{\mathrm{r}}^2 P$. The results for three different roughness periods, seen in Figure 7-10A, superpose when plotted as a function of $K f_{\mathrm{r}}^2 P / r_0$. The product of the roughness factor and the geometric disk radius is the characteristic dimension for a rough disk; whereas the radius of the disk is the characteristic length for a smooth electrode. The period of the roughness multiplied by the square of the roughness factor is the appropriate characteristic length associated with the roughness itself.

The deviation from an ideal response of a rough recessed electrode at high frequency may be explained by the nonuniform current and potential distribution along the electrode surface presented in Figure 7-11. The results for K=10^{-5} are presented in Figure 7-11A and the results at K=10^{3} are presented in Figure 7-11B. The streamlines represent the

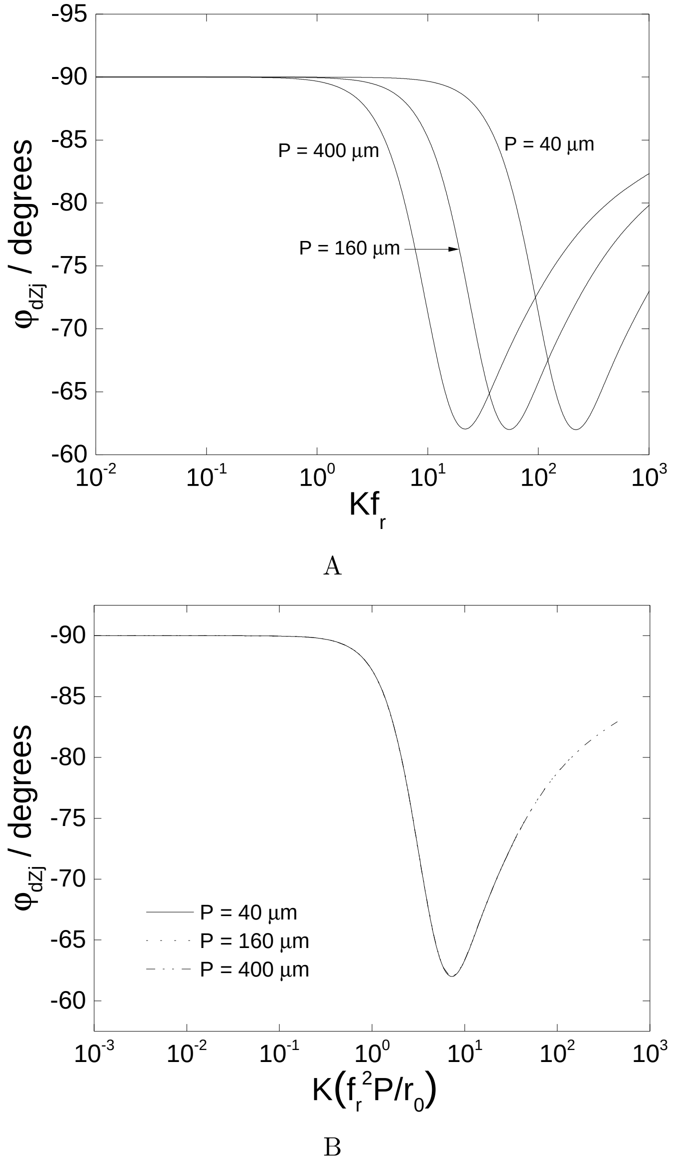

Figure 7-10. Imaginary–impedance–derived–phase angle calculated from the simulated impedance of a rough recessed electrode with the roughness period as a parameter: a) as a function of dimensionless frequency Kf_{r}; and b) as a function of dimensionless frequency Kf_{r}^2P/r_0.

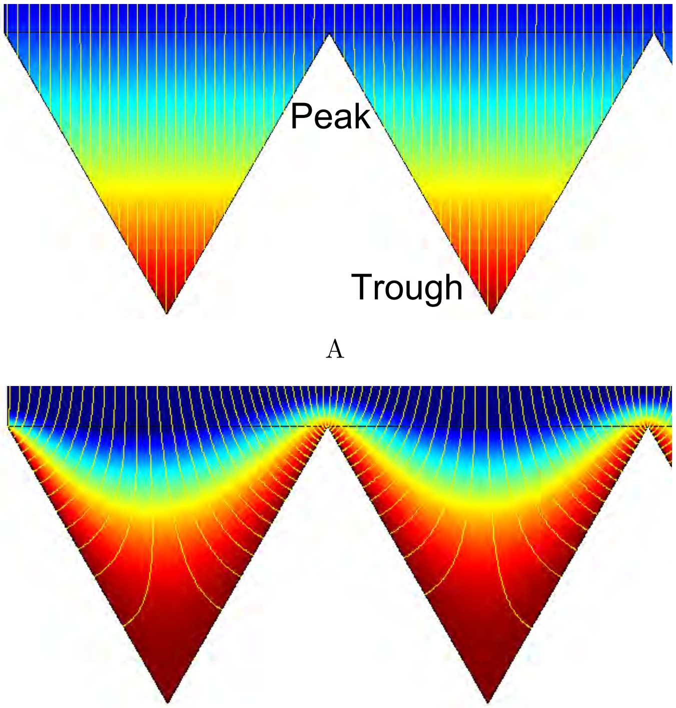

A

B

Figure 7-11. The current paths obtained as $\mathrm{Re}\{\tilde{i}\exp(\mathrm{j}wt)\}$ at a fixed time, t: a) at $K = 10^{-5}$; b) at $K = 10^{3}$. The potential distribution within the electrolyte adjacent to the rough surface is shown by the false–color representation.

current distribution and the potential distribution is shown as a false color gradient. At low frequencies, the potential varied uniformly with the depth of the roughness such that the current lines were parallel to the y–axis. The potential distribution at high frequencies followed the surface profile and the current did not reach the deepest parts of the rough surface. The change in current distribution with frequency caused the observed frequency dispersion.

The local current density at a peak and a trough of one of the grooves of the electrode surface is presented in Figure 7-12 as a function of frequency for a recessed electrode. The current was very small at low frequencies, as expected for a blocking electrode, and increased with frequency in the same manner for both the peak and trough. At high frequencies, the current at the peak increased sharply; whereas, the current at the trough

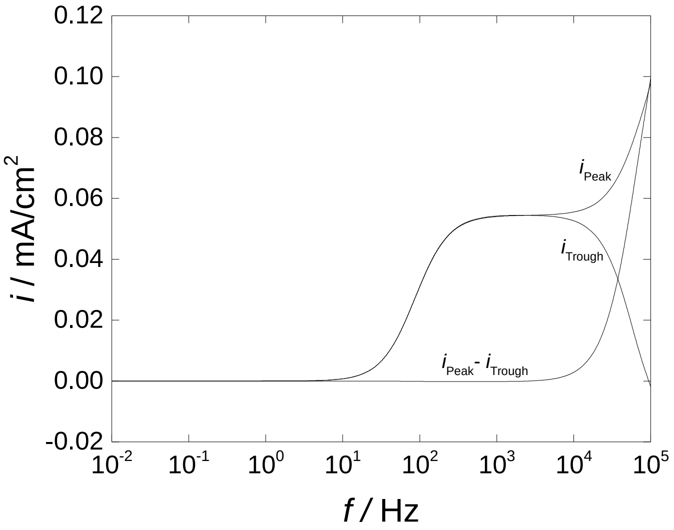

Figure 7-12. Calculated current density at a peak and trough for a recessed electrode as a function of frequency.

dropped to zero. The frequency at which the current at the peak and the trough diverged corresponded to the frequency at which the surface roughness influenced the impedance.

The effective capacitance of the electrode/electrolyte interface may be determined from the imaginary part of the impedance as

$$C_{\mathrm{eff}} = \frac{-1}{\omega Z_{\mathrm{j}}} \tag{7–25}$$

The ratio of the effective capacitance and the input capacitance is provided in Figure 7-13 for the recessed electrode as a function of dimensionless frequency, $\mathrm{K}f_{\mathrm{r}}$, with the roughness factor as a parameter. The current reached all parts of the rough electrode at low frequencies, making the capacitance ratio equal to the roughness factor. At high frequencies, the penetration depth of the current was smaller than the depth of the roughness, and the capacitance ratio decreased due to the nonuniform current distribution associated with the combined effects of the disk geometry and the surface roughness. The effective capacitance of the smooth disk, $f_{\mathrm{r}} = 1$, was equal to the input capacitance, C_0, for all of the frequencies simulated.

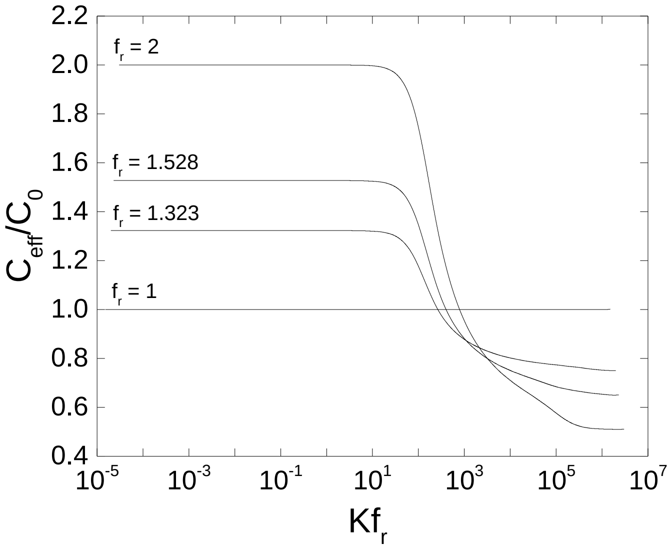

Figure 7-13. The ratio of the calculated effective capacitance and the input capacitance as a function of dimensionless frequency Kf_r with the roughness factor as a parameter for recessed disk electrodes.

An inherent difficulty in determining the characteristic frequency associated with roughness is that the shape of the roughness greatly influences the ohmic resistance[59]. Nevertheless, according to the geometry-independent ohmic resistance expressed in Equation 7–22, the characteristic frequency at which roughness begins to influence the impedance may be roughly estimated as

$$f_\mathrm{c} = \frac{\kappa}{2\pi C_0 f_r^2 P} \tag{7–26}$$

which may be compared to the characteristic frequency developed for a rough disk geometry in equation 7–20.

The frequency at which time–constant dispersion was observed is presented in Figure 7-14 as a function of $f_r^2 P$ for three different ratios of electrolyte conductivity and interfacial capacitance. The characteristic length $f_\mathrm{r} r_0$ associated with a disk within an insulating plane is also provided. The 10^4 cm/s conductivity to capacitance ratio may be obtained for a capacitance $C_0 = 1$ μ F/cm^2, representative of an oxide layer, and conductivity $\kappa = 0.01$ S/cm, representing a 0.1 M NaCl solution. The value $\kappa/C_0 = 10^3$

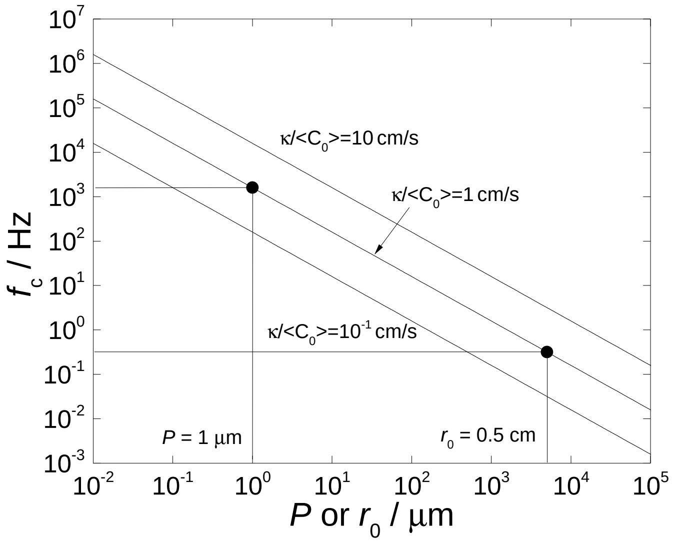

Figure 7-14. The characteristic frequencies, f_{c}, associated with dimensionless frequencies $K(f_{\mathrm{r}}^2 P/r_0) = 1$ or $K(f_{\mathrm{r}}) = 1$ at which the surface roughness influences the impedance as a function of either the roughness depth or the product of roughness factor and electrode radius with κ/C_0 as a parameter.

cm/s may correspond to a capacitance $C_0 = 10$ μF/cm^2 representative of a double layer on an inert metal, and a conductivity, $\kappa = 0.01$ S/cm, again indicative of a 0.1 M NaCl solution.

For an inert rough disk electrode with a roughness factor of 5 and an average width or period of roughness equal to 4 μm (approximately half of the average particle size of No. 1000 grit paper), frequency dispersion due to roughness will initiate at a frequency of 16 kHz for $\kappa/C_0 = 10^3$. If the electrode radius is 0.5 cm, frequency dispersion due to the disk geometry within an insulating plane will occur at 65 Hz, which is much lower than the frequency at which the effect of surface roughness is observed.

The results presented here demonstrate that surface roughness on solid electrodes influences the impedance response when coupled with the effect of nonuniform current distributions due to disk electrode geometry. For small roughness factors, roughness by itself causes frequency dispersion only at frequencies greater than that due to the geometry of disk electrodes.

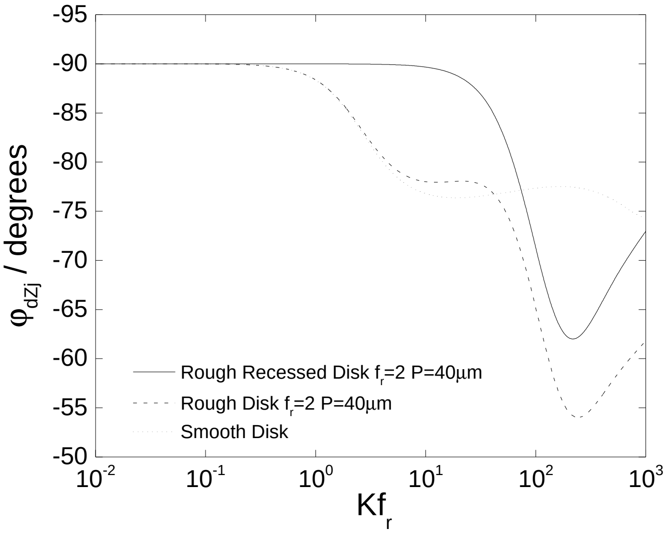

Figure 7-15. The imaginary–impedance–derived–phase angles calculated from impedance simulations of a rough recessed electrode ($f_r = 2$ and $P = 40$ μm), a rough disk electrode within an insulating plane ($f_r = 2$ and $P = 40$ μm), and a smooth disk electrode within an insulating plane.

However, since the roughness factor is a parameter contained within the characteristic dimension of the disk geometry and the surface roughness, there will exist cases in which the roughness of the disk will cause frequency dispersion at frequencies lower than the effect of the disk geometry. Porous electrodes provide an example in which the roughness factor can be on the order of 1000 and the effect of disk geometry would not be seen. Specifically, when $f_r P$ is greater than r_0, frequency dispersion due to the surface roughness will control.

Comparisons are provided in Figure 7-15 for the imaginary–impedance–derived–phase angle associated with a smooth disk electrode, a rough disk electrode within an insulating plane with $f_r = 2$ and $P = 40$ μm, and a rough recessed disk electrode with $f_r = 2$ and $P = 40$ μm. The geometry of the smooth disk electrode within an insulated plane caused deviation from ideal behavior at $\mathrm{K}f_{\mathrm{r}} = 1$ due to the nonuniform current distribution. The line representing the rough, recessed electrode showed frequency dispersion at $\mathrm{K}f_{\mathrm{r}} = 20$, which is numerically equal to $\mathrm{K}f_r^2 P/r_0$=1. The rough electrode within the insulating plane showed the effect of both the disk geometry and the roughness. The roughness effect occurred at $\mathrm{K}f_{\mathrm{r}} = 20$ and the disk geometry effect was observed at $\mathrm{K}f_{\mathrm{r}} = \mathrm{K} = 1$.

7.3.2.1 Effect of pore geometry

Since the shape of the roughness influences the roughness factor, other geometries were modeled to ensure the use of the characteristic dimension for roughness. Rectangular grooves as well as separated V-shaped grooves were simulated. The spacing between the grooves can be accommodated by replacing f_r^2 with $f_r f_p$ where f_p is the surface area of the groove divided by the area of the groove mouth. Therefore, the characteristic frequency at which the roughness will begin to influence the impedance is

$$f_c = \kappa / 2\pi C_0 f_r f_p P \tag{7–27}$$

The imaginary–impedance–derived phase angle for a rough electrode with rectangular grooves is shown in Figure 7-16 with the width of the grooves as a parameter. Figure 7-16A shows the results as a function of frequency and Figure 7-16B shows the results as a function of dimensionless frequency in which the characteristic dimension was expressed as $f_r f_p P$. When the results are shown as a function of frequency, the frequency at which disherison begins to occur increases as the width of the grooves increase. When the results are shown as a function of dimensionless frequency the plots superpose and frequency dispersion begins at a dimensionless frequency of 1.

Similar simulations were performed for a rough electrode with V–shaped grooves with a space between them. The imaginary–impedance–derived phase angle is shown in Figure 7-17 with the width of the grooves as a parameter. Figure 7-17A shows the results as a function of frequency and Figure 7-17B shows the results as a function of dimensionless frequency in which the characteristic dimension was expressed as $f_r f_p P$. Once again, when the results are shown as a function of dimensionless frequency, the frequency dispersion for each width occurs at dimensionless frequency equal to 1. Thus, the characteristic

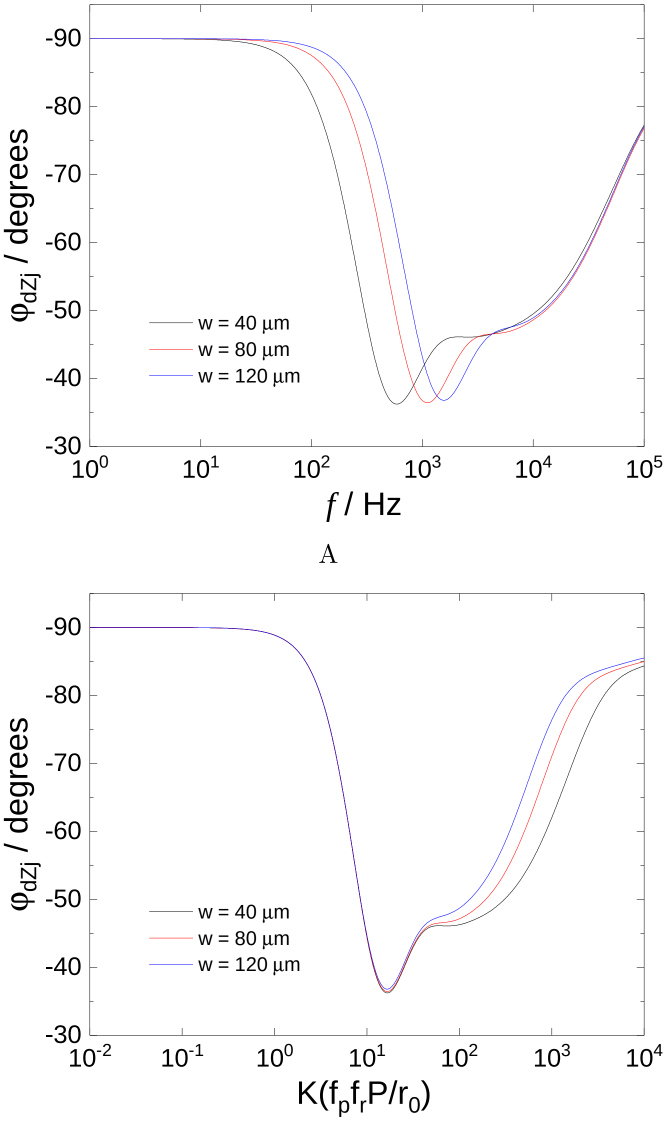

A

B

Figure 7-16. The imaginary–impedance–derived phase angle for a rough electrode with rectangular grooves with the width of the grooves as a parameters.

dimension for roughness presented here is general and can be applied to different shapes of roughness.

7.3.2.2 Transition from a rough electrode to a porous electrode

Porous electrodes are extremely rough electrodes usually containing a complicated network of electro–active pores. Roughness factors for porous electrodes can be 1000 or greater. DeLevie developed the theory of porous electrodes by deriving an expression

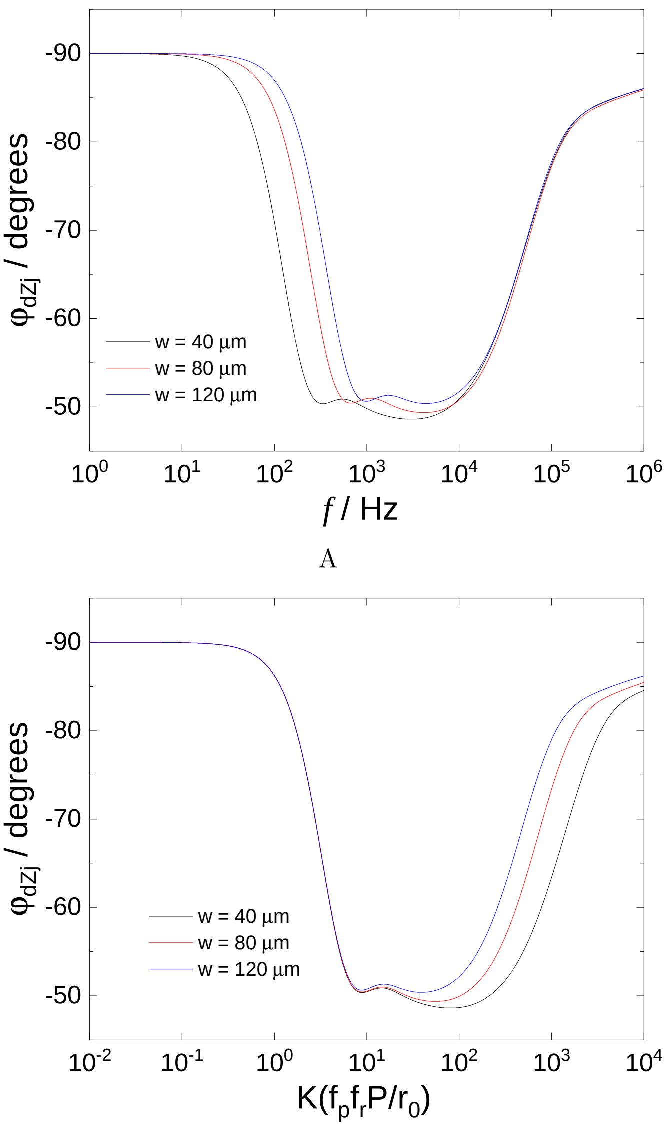

A

B

Figure 7-17. The imaginary–impedance–derived phase angle for a rough electrode with V-shaped grooves with a space between them and the width of the grooves as a parameter.

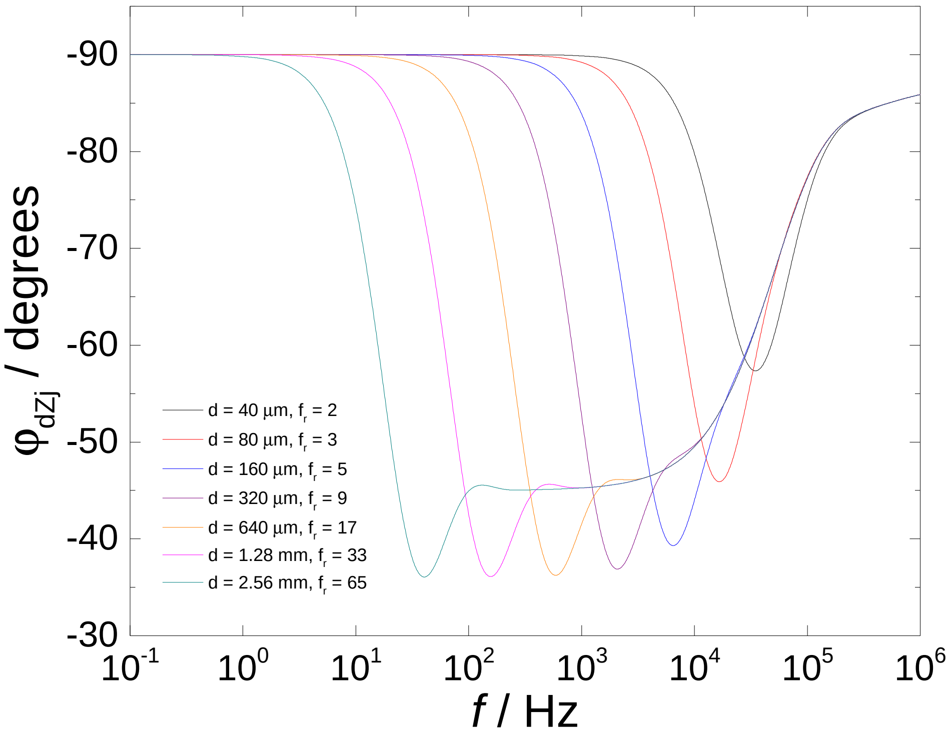

Figure 7-18. The imaginary impedance derived phase angle of rough electrodes as a function of frequency with the depth of grooves and roughness factor as parameters.

for the impedance of a single cylindrical pore.[18] A blocking porous electrode will have a phase angle of 45° at high frequencies. The transition from a rough electrode to a porous electrode may be shown by increasing the depth of the rectangular grooves until the simulated response reflects a porous behavior. Shown in Figure 7-18 is the imaginary–impedance–derived phase angle as a function of frequency for increasingly rough electrodes, characterized by the depth of the rectangular grooves as well as the roughness factor. As the depth of the grooves is increased, the frequency dispersion occurs at lower frequencies. The more interesting feature, however, is the increase in the magnitude of the frequency dispersion at frequencies beyond the initial occurrence of frequency dispersion. As the depth of the rectangular grooves and thus the roughness factor increases, the phase angle approaches a limit of 45° therefore exhibiting a porous electrode response. If the same results are presented as a function of the dimensionless

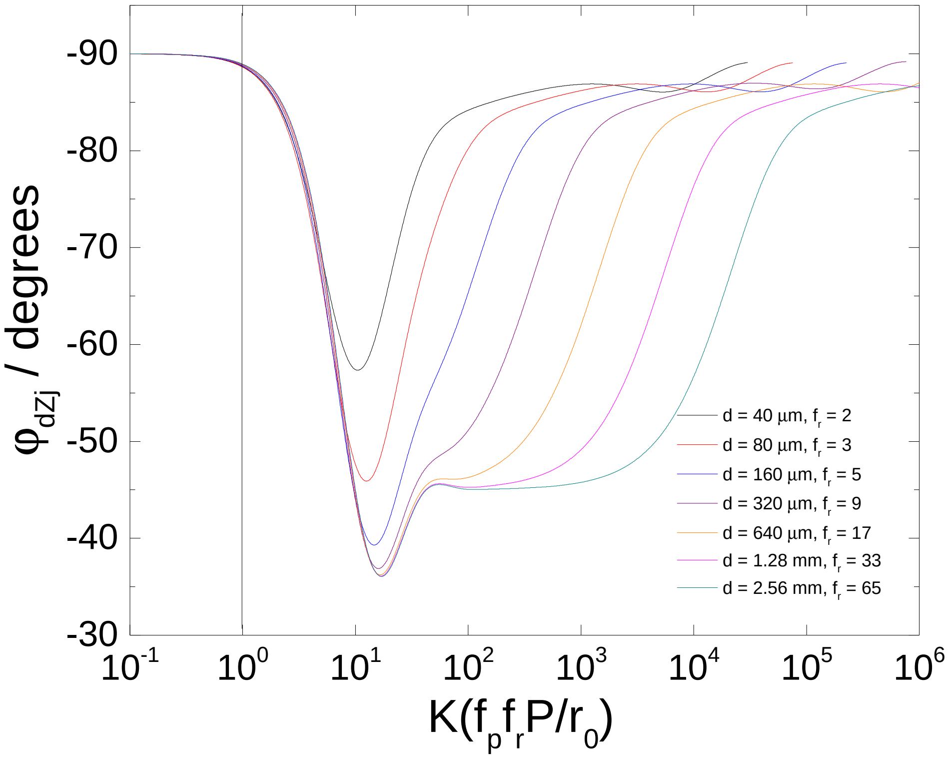

Figure 7-19. The imaginary impedance derived phase angle of rough electrodes as a function of dimensionless frequency with the depth of grooves and roughness factor as parameters.

frequency, shown in Figure 7-19, the plots superpose at dimensionless frequency equal to 1 and clearly show the increase in frequency dispersion as it approaches a phase angle of 45° at higher frequencies. Therefore, the characteristic dimension provided for rough electrodes may also be used to describe the frequency at which a porous electrode response should occur.

CHAPTER 8
INFLUENCE OF CAPACITANCE DISTRIBUTION ON IMPEDANCE

Impedance measurements on solid electrodes often yield constant–phase–element(CPE) behavior over a large range of frequencies. A CPE describes a distribution of time constants which can be physically categorized as occurring either normal to or along the electrode surface [30].

Hirschorn et al.[24, 25] used a measurement model incorporating a series of elements to show that a power-law distribution of resistivity through an oxide film gives rise to CPE behavior. This model has been used to determine the film thickness of oxides on stainless steel and aluminum electrodes[58]. It has also been used to determine physical properties of human skin[58, 74] and polymer coatings[48].

Distributions of solution resistance are observed in planar disk electrode experiments. Huang et al. showed that the geometry of a disk electrode within an insulating plane leads to frequency dispersion on blocking electrodes at frequencies greater than dimensionless frequency $\omega C_0 r_0/\kappa{=}1$ [28]. Jorcin et al. [30] confirmed these results experimentally with the use of local electrochemical impedance spectroscopy.

Surface roughness of the electrode, once believed to contribute to the cause for frequency dispersion [11], will also yield a distribution of ohmic resistance. Alexander et al.[4] showed that surface roughness at the micron scale leads to frequency dispersion at frequencies larger than those due to the disk geometry if the radius of the disk is greater than the characteristic length, $f_r P$, where f_r is the roughness factor and P is the period of the roughness. The period of the roughness may represent the average width of the rough grooves. The disk radius will in most cases be greater than this characteristic dimension except in cases of very large roughness factors such as those that yield porous electrode behavior. This result contradicts the theory that surface roughness may be a source of CPE behavior over a large range of frequencies.

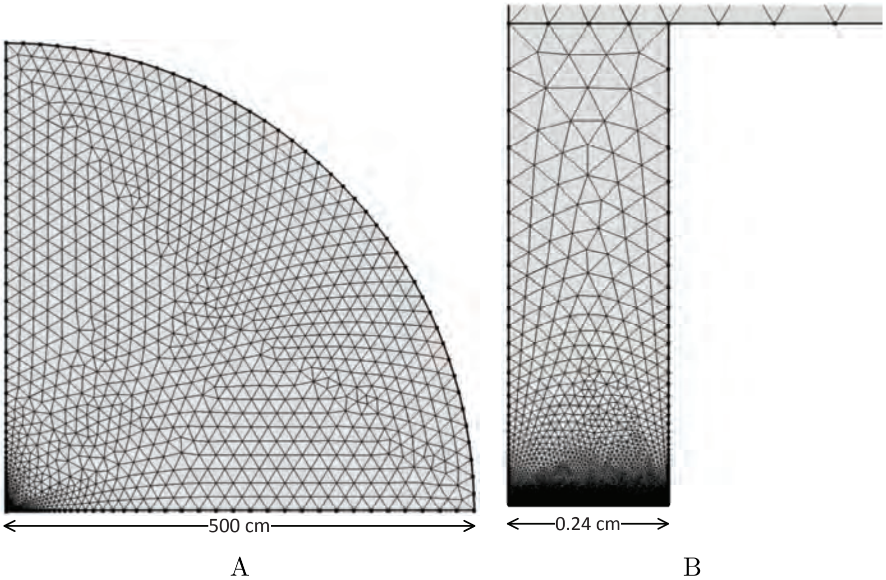

Figure 8-1. Finite-element mesh for the disk electrode simulations. a) Axi-symmetric domain used to represent disk electrode experiments; b) mesh showing a detailed view of a recessed electrode. The outer domain is shown in Figure 10-3.

The objective of this work is to explore, by use of finite-element models, whether a surface distribution of capacitance could provide a valid physical explanation for CPE behavior over a broad range of frequencies and to determine the characteristic frequency and dimension associated with this form of surface heterogeneity.

8.1 Impedance Calculations

Two disk electrode configurations were simulated, including a disk electrode embedded within an insulating plane, and a recessed disk electrode. The calculations were performed in COMSOL Multiphysics 4.3 using cylindrical coordinates for a quarter of a circle domain, provided in Figure 10-3, which represented the electrolyte. Calculations were performed for electrode radii of 0.12 cm, 0.24 cm, and 0.48 cm. The counterelectrode was located at $\sqrt{r^2+y^2}$=500 cm, making the domain size at least 1000 times larger than the radius of the disk (see Alexander et al.[4]). This geometry was chosen to ensure that the counterelectrode could be considered to be infinitely far from the working electrode.

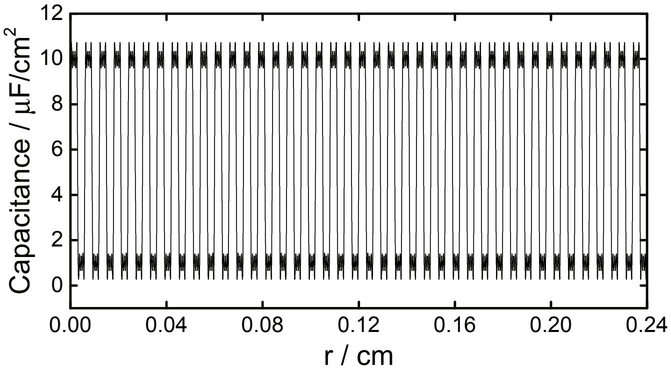

Figure 8-2. Capacitance distribution as a function of radial position based on a square wave represented by a Fourier series with a period of 60 μm.

A free triangular mesh was used with a greater density of elements near the working electrode.

A capacitance distribution was simulated by a Fourier series that represented a square wave distribution, as shown in Figure 8-2 as a function of radial position. The Fourier series[21] was expressed as

$$C_0(r) = \langle C \rangle + \sum_{n=1}^{\infty} (C_{\max} - C_{\min}) \cos(2n\pi P r) \tag{8–1}$$

where the constants $C_{\max}$ and $C_{\min}$ represented the maximum and minimum capacitance. The average capacitance of the electrode surface $\langle C \rangle$ was calculated as

$$\langle C_0 \rangle = \frac{2}{r_0^2} \int_0^{r_0} C_0(r) r dr \tag{8–2}$$

where r_0 is the radius of the disk. The capacitance as a function of the radial position was integrated over the surface of the electrode and then divided by the area of the electrode. The period P of the square wave may be representative of an elemental grain size in which the capacitance is assumed to be relatively uniform across a grain and then jump to another value at an adjacent grain. Simulations were performed with 5, 10, 20, and 40 terms of the Fourier series. Numerical artifacts were observed at high frequencies when the series was truncated at 5 and 10 terms. As more terms were added to the series the artifacts shifted to higher frequencies and with 20 terms in the series this behavior was eliminated from the simulated frequency range. The Fourier series was therefore truncated after 20 terms.

The electrode was assumed to be purely capacitive, i.e., the contributions of slow reaction kinetics and mass-transfer were neglected. The potential distribution within the electrolyte domain was solved using Laplace's equation

$$\nabla^2\Phi = 0. \tag{8–3}$$

The potential comprises steady-state and oscillating components and may be expressed as

$$\Phi = \bar{\Phi} + \mathrm{Re}\left\{\tilde{\Phi}\exp(\mathrm{j}\omega t)\right\} \tag{8–4}$$

The potential of the electrode surface may also be expressed in the same manner as

$$V = \bar{V} + \mathrm{Re}\left\{\tilde{V}\exp(\mathrm{j}\omega t)\right\} \tag{8–5}$$

The normal oscillating current density at the surface of the electrode was expressed as

$$\tilde{i} = \mathrm{j}\omega C_0(r)(\tilde{V} - \tilde{\Phi}) \tag{8–6}$$

where $\tilde{V}$ is the potential perturbation at the electrode and $\tilde{\Phi}$ is the complex oscillating potential within the electrolyte. The value of the potential perturbation will not affect the impedance response, but, for all of the stimulations presented in this work, a value of 10 mV was used. The oscillating potential was constrained to be equal to zero at the counterelectrode. The impedance was calculated as

$$Z(\omega) = \frac{\tilde{V}}{\tilde{i}} \tag{8–7}$$

for a specified range of frequencies.

8.2 Results and Discussion

Impedance simulations are presented to show the influence of a heterogeneous surface capacitance on disk electrodes. Results are shown first for a recessed electrode

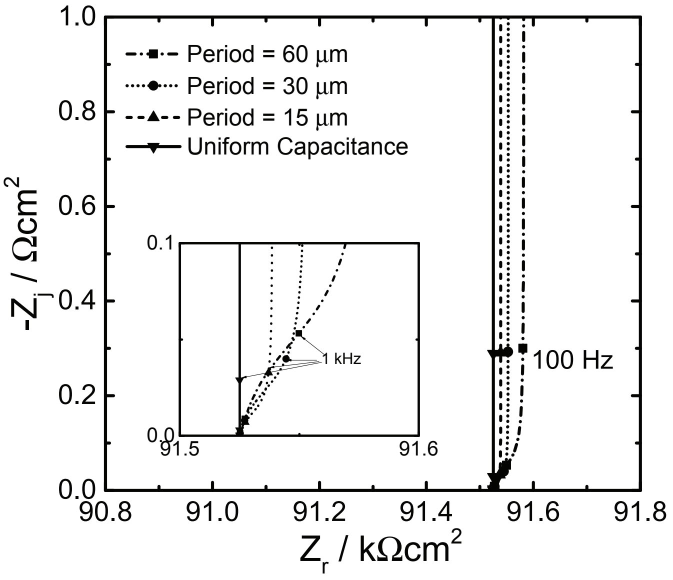

Figure 8-3. The impedance in Nyquist format of a recessed disk electrode with the square wave capacitance distribution shown in Figure 8-2 and the period of distribution as a parameter.

configuration and then a disk electrode within an insulating plane. Dimensionless results are used to determine the characteristic lengths and frequencies associated with a radially-periodic distribution of capacitance.

8.2.1 Capacitance Distribution on Recessed Electrodes

A recessed electrode model was used to isolate the effect of surface heterogeneity on the impedance response of blocking electrodes. The simulated impedance response of a recessed disk electrode with the square wave capacitance distribution shown in Figure 8-2 is presented in Figure 8-3 as a function of frequency with the period of distribution as a parameter. The minimum and maximum capacitance values expressed in Equation 9–5 were set to $1\mu\text{F/cm}^2$ and $10\mu\text{F/cm}^2$ respectively to represent a surface with an oxide film and a bare metal surface. The conductivity of the solution was 10^{-5} S/cm. The impedance was representative of an ideal capacitor at frequencies below 100 kHz, shown by the vertical lines that are perpendicular to the real axis. The figure inset shows a magnified view of the impedance at high frequencies. As the period of the capacitance distribution increases, the frequency at which dispersion begins decreases.

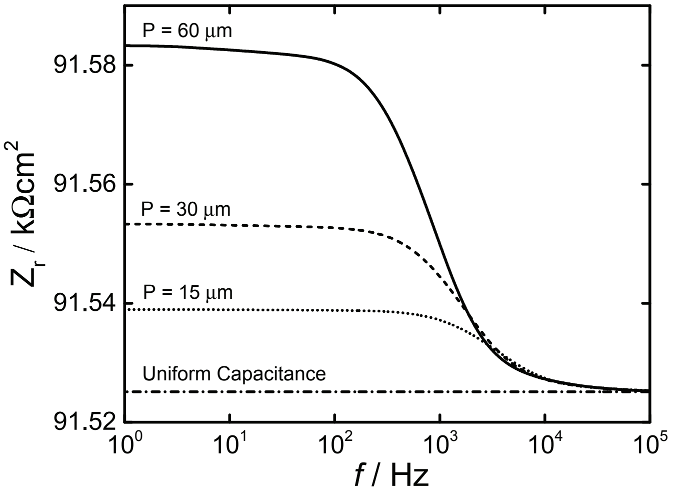

A

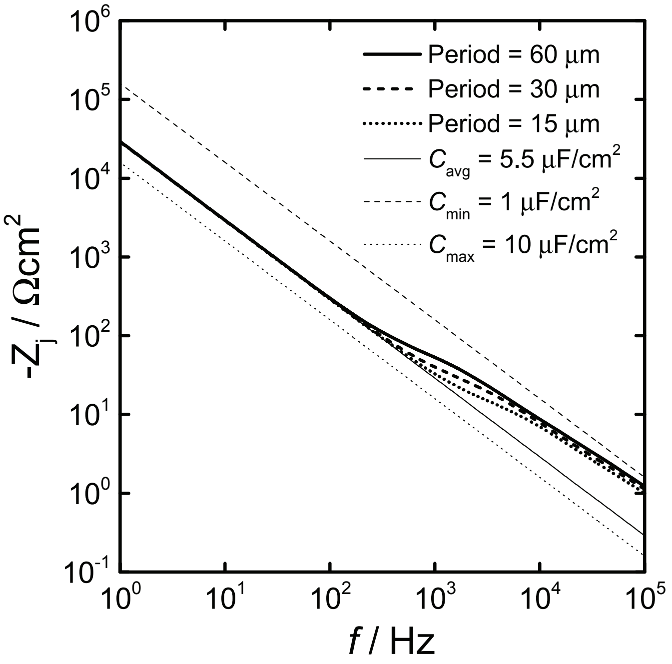

B

Figure 8-4. The simulated impedance as a function of frequency of a recessed disk electrode with a square wave capacitance distribution and the period of distribution as a parameter: a) the real part of the impedance; b) the imaginary part of the impedance.

The simulated real impedance as a function of frequency is presented in Figure 8-4A with the period of the capacitance distribution as a parameter. The low–frequency limit of the real impedance increased as the period of the distribution increased. The high–frequency limit, which represents the ohmic resistance, was unaffected by the distribution of capacitance.

The imaginary impedance may be expressed as a function of the surface–averaged capacitance as

$$\langle Z \rangle = \frac{-1}{\omega \langle C_0 \rangle} \tag{8–8}$$

Similar expressions may be formed for the maximum and minimum values of the capacitance. The impedance calculated from surface–averaged as well as the maximum and minimum capacitance values are compared to the simulated imaginary impedance in Figure 8-4B as a function of frequency with the period of the distribution as a parameter. The imaginary impedance at low frequencies coincided with the impedance based on the surface–averaged capacitance. Deviation from the surface–averaged impedance occurred at high frequencies where the impedance asymptotically approached the impedance associated with the minimum capacitance value.

The deviation from the expected impedance response may be explained by the current and potential distribution along the electrode surface, which is presented in Figure 8-5. In the case of blocking electrodes, the solution resistance controls the current distribution at high frequencies while the interfacial impedance controls at low frequencies. The potential distribution at low frequencies is represented by the color gradient in Figure 8-5A. The streamlines corresponded to the path of the modulus of the oscillating current expressed as

$$|\tilde{i}(\omega)| = \sqrt{\tilde{i}_{\mathrm{r}}^{\,2} + \tilde{i}_{\mathrm{j}}^{\,2}} \tag{8–9}$$

in which $\tilde{i}_{\mathrm{r}}$ and $\tilde{i}_{\mathrm{j}}$ represent the real and imaginary parts of the oscillating current. The false color representation of potential distribution was adjusted to emphasize the variations near the electrode surface. The regions of the electrode surface with higher capacitance have a lower impedance and the current flows more easily through these points. Despite the nonuniform current distribution, the impedance response at low frequencies was indicative of a pure capacitor with a value of the averaged surface

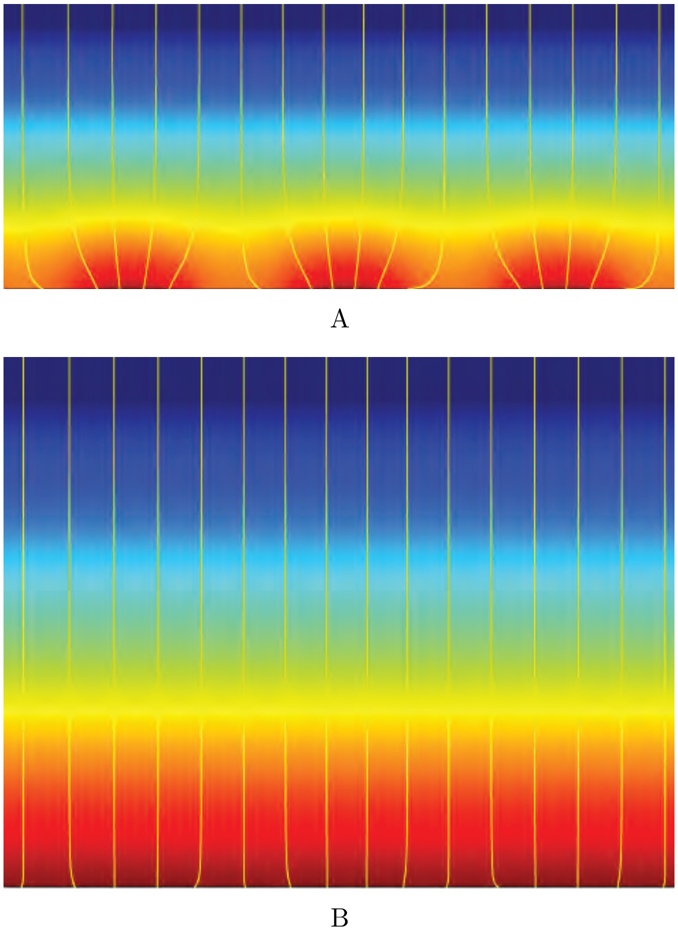

Figure 8-5. The current paths near the surface of a recessed electrode exhibiting a square–wave distribution of capacitance obtained as $\sqrt{\tilde{i}_r^2 + \tilde{i}_j^2}$: a) at 10 mHz; b) at 100 kHz. The potential distribution within the electrolyte adjacent to the rough surface is shown by the false–color representation.

capacitance. The potential distribution along the electrode surface at 100 kHz, presented in Figure 8-5B, was more uniform.

The modulus of the oscillating current density along the electrode surface is presented in Figure 8-6 as a function of radial position. The low–frequency current response, presented in Figure 8-6A, showed a variation of current proportional to the variation in surface capacitance and small values of current. The high frequency response, presented in Figure 8-6B, showed much higher values of current however the distribution was much more uniform with only variations at locations where the capacitance changes from one

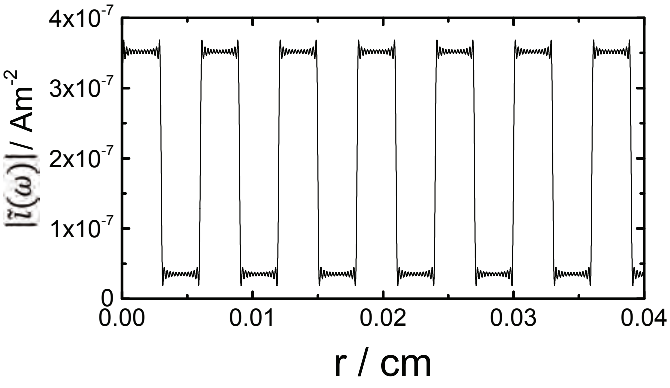

A

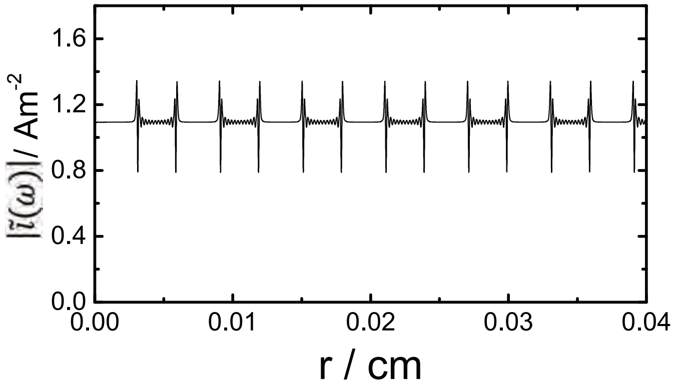

B

Figure 8-6. Normal current distribution at the electrode surface due to a nonuniform capacitance distribution with a period of 60μm of a recessed electrode as a function of radial position: a) current distribution at 10mHz; b) current distribution at the high frequency limit of the simulations $f = 100$ kHz.

value to the other which can be attributed to the finite number of terms in the Fourier series.

A phase angle dependent only on the imaginary part of the impedance was defined by Alexander et al. [4] as

$$\varphi_{\mathrm{dZj}} = \frac{\mathrm{dlog}(Z_{\mathrm{j}})}{\mathrm{dlog}(f)} \times 90^{\circ}. \tag{8–10}$$

As compared to other definitions of phase angle, the imaginary–impedance–derived phase angle is more sensitive to the onset of frequency dispersion. The imaginary–impedance–derived phase angle is presented in Figure 8-7A as a function of frequency with the period of distribution as a parameter. The effect of a varying capacitance along the surface of

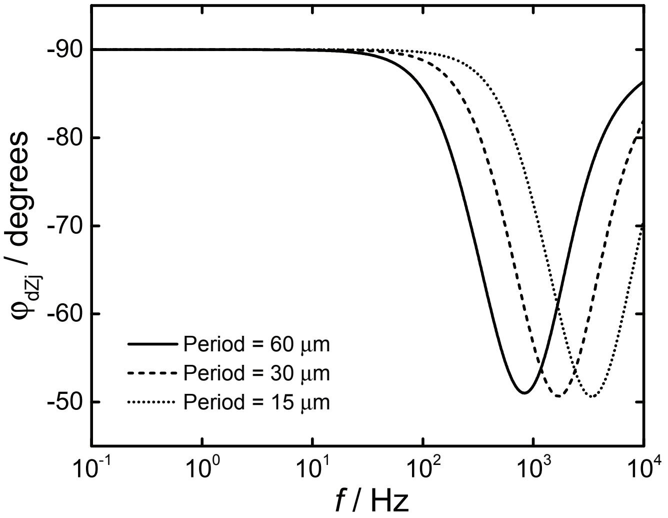

A

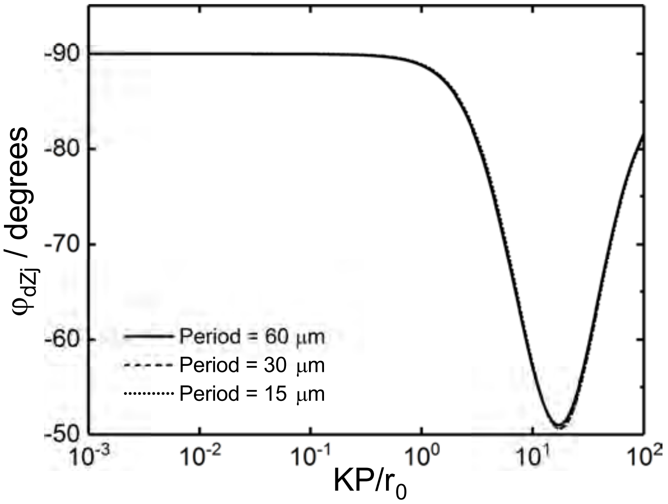

B

Figure 8-7. Imaginary–impedance–derived phase angle calculated from the impedance data in Figure 8-4: a) phase angle as a function of frequency; b) phase angle as a function of dimensionless frequency based on the averaged capacitance and the period of the distribution.

the electrode did not influence the imaginary impedance at low frequencies as indicated by a phase angle, ϕ_{dZj} = -90°. However, frequency dispersion did occur in all cases at high frequencies with a minimum phase angle of approximately $-50°$. The deviation from the expected capacitive behavior occurred at lower frequencies as the period of the distribution increased. If the period of the distribution is taken as the grain size within a polycrystalline surface, grain sizes on the order of 1μm and less should not lead to frequency dispersion at frequencies less than 1 kHz.

A dimensionless frequency can be expressed for the distribution of capacitance by amending Equation 7–7 to include the surface–averaged capacitance expressed as

$$K = \omega \langle C_0 \rangle l_{\mathrm{c,Cap}} \tag{8–11}$$

where $l_{c,Cap}$ represents the characteristic length for the capacitance distribution. Since the frequency dispersion shifted to lower frequencies with increases in the period of the distribution, one obvious choice for the characteristic length associated with a distribution of capacitance is the period of the distribution. The imaginary–impedance–derived phase angle is presented in Figure 8-7B as a function of dimensionless frequency. The results were superposed, confirming that the period is the appropriate characteristic length to use to describe surface heterogeneity of capacitance. The characteristic frequency at which a non-uniform capacitance began to influence the impedance was determined to be $KP/r_0 = 1$.

Since impedance is often used to measure interfacial capacitance, it is important to ensure that a distribution of capacitance along the surface does not complicate the use of this technique. The effective capacitance of the electrode/electrolyte interface may be determined from the imaginary part of the impedance as

$$C_{\mathrm{eff}} = \frac{-1}{\omega Z_{\mathrm{j}}} \tag{8–12}$$

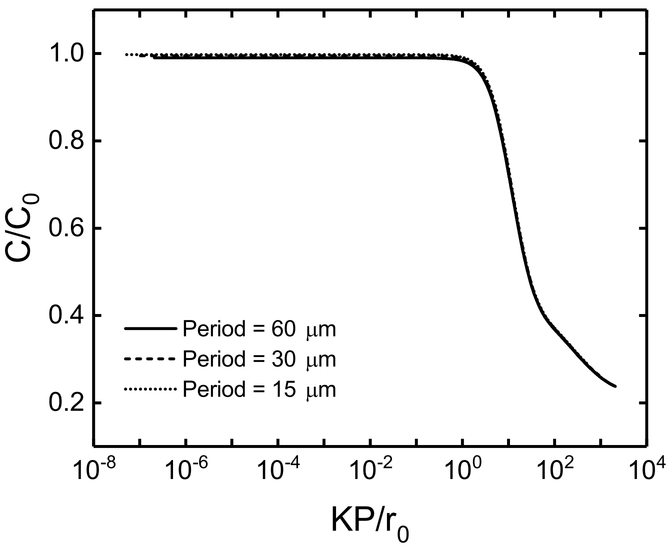

Figure 8-8. The ratio of the calculated effective capacitance and the surface–averaged input capacitance as a function of dimensionless frequency KP/r_0 with the period of the distribution as a parameter for recessed disk electrodes.

The ratio of the calculated capacitance and the surface–averaged capacitance is shown in Figure 8-8 as a function of dimensionless frequency with the period of the distribution as a parameter. In all cases, the simulated capacitance closely matched the surface–averaged capacitance of the electrode at low frequencies.

8.2.2 Capacitance Distribution on Disk Electrodes

The impedance of a disk electrode within an insulating plane containing a heterogenous surface capacitance was simulated to show the coupled effect of capacitance distribution and non-uniform current distributions due to disk geometry. The goal of these simulations was to determine if the effect of capacitance distribution influences the impedance at frequencies lower than the effect of disk geometry.

The geometry of a disk electrode embedded within an insulating plane causes frequency dispersion at high frequencies due to the non-uniform current distribution at high frequency. As the frequency increases to infinity, the magnitude of the oscillating component of the modulated current at the periphery of the disk approaches infinity while the current at the center of the disk remains finite. The simulated current distribution

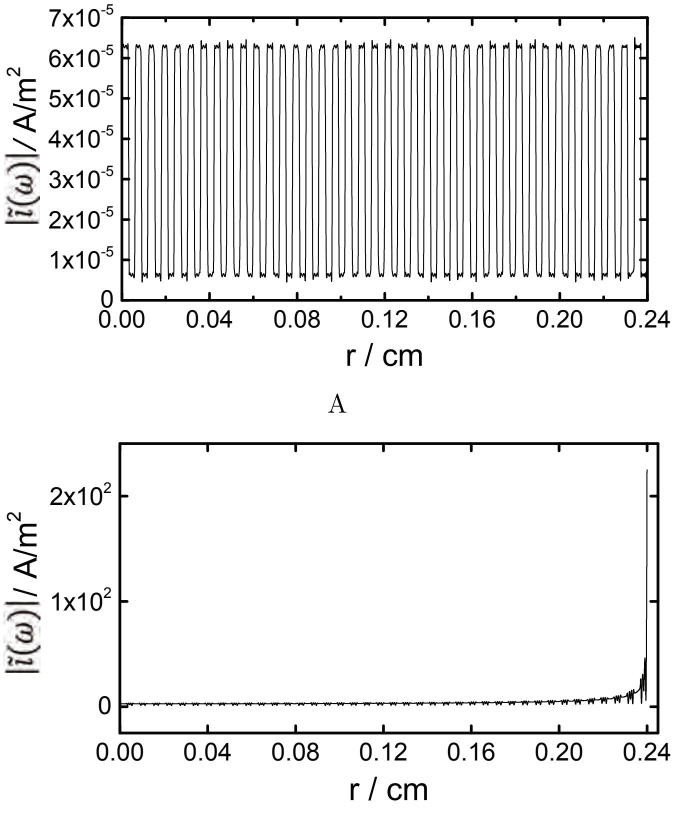

A

B

Figure 8-9. Normal current distribution at a disk electrode surface as a function of radial position: a) current distribution at 10 mHz; b) current distribution at 100 kHz.

at an electrode surface containing the capacitance distribution in Figure 8-2 is provided as a function of radial position for 10 mHz in Figure 8-9A and for 100 kHz in Figure 8-9B. The current distribution at low frequencies resembled the square–wave distribution features. At high frequencies, the effect of the disk geometry overshadowed the effect of the capacitance distribution since the current at the periphery approached infinity.

The imaginary–impedance–derived phase angle is provided in Figure 8-10A as a function of frequency. At low frequencies the phase angle was constant with a value equal to −90°. Frequency dispersion became apparent at approximately 1 Hz for all periods of capacitance distribution due to the geometry of the disk. At higher frequencies, dispersion due to the nonuniform capacitance distribution occurred such that increases in the period

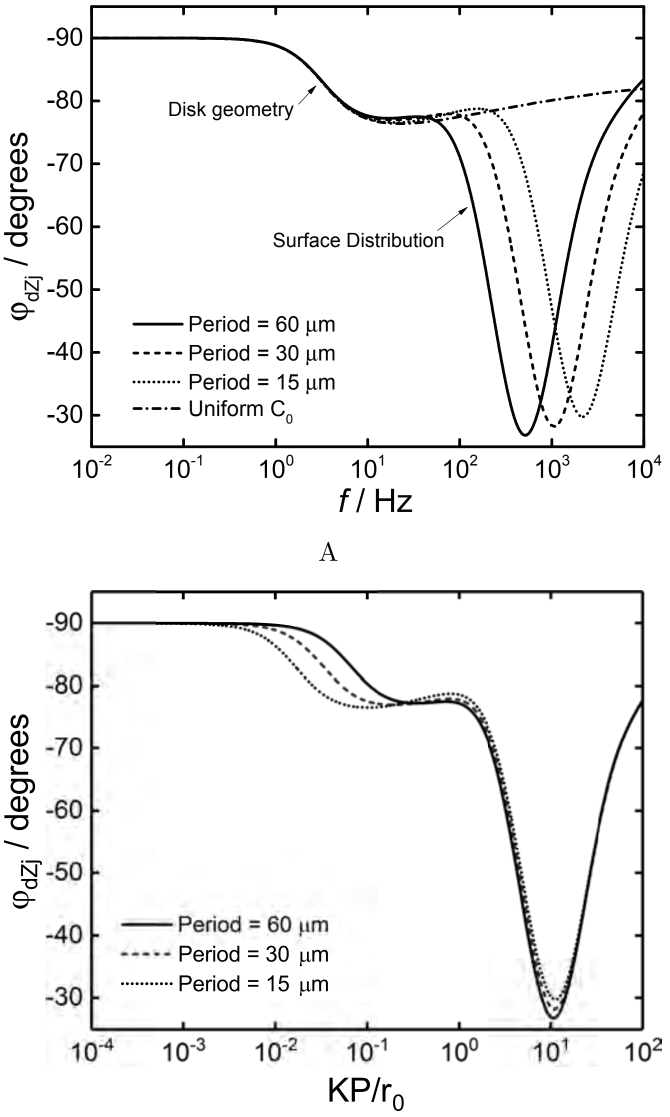

A

B

Figure 8-10. Imaginary–impedance–derived phase angle for a disk electrode within an insulating plane: a) phase angle as a function of frequency; b) phase angle as a function of dimensionless frequency based on the averaged capacitance.

of the distribution caused the deviation to shift to lower frequencies. The same results are presented in Figure 8-10B as a function of dimensionless frequency in which the period of the distribution was used as the characteristic length. The frequency dispersion due to the surface heterogeneity was superposed, indicating that the period of the capacitance distribution is the appropriate characteristic length. The results obtained for a recessed electrode provided in Figure 8-7 show only the frequency dispersion due to the surface distribution of capacitance.

The imaginary–impedance–derived phase angles are presented in Figure 8-11A as a function of frequency with the radius of the disk as a parameter. The period of the distribution was fixed at 60 μm. Changes in the radius of the electrode influenced only the frequency dispersion associated with the geometry of the disk. The imaginary impedance derived phase angle is shown in Figure 8-11B as a function of dimensionless frequency, Equation 7–8. The frequency dispersion associated with disk geometry was superposed and the frequency dispersion associated with the capacitance distribution was not.

Simulations were performed to explore whether the amplitude of the capacitance distribution may influence the frequency at which the impedance is influenced. The imaginary–impedance–derived–phase angle was calculated from simulations on planar disk electrodes with different amplitudes of capacitance distribution and are presented in Figure 8-12 as a function of frequency. As the amplitude of the distribution increased, the deviation from -90° shifted to lower frequencies. However, when the frequency is made dimensionless with the use of the period as the characteristic length and the average value of the capacitance, shown in Figure 8-12B, the characteristic frequency at which dispersion occurred did not change with amplitude and only the magnitude of the dispersion increased.

The ratio of the calculated capacitance and the average capacitance is presented as a function of dimensionless frequency in Figure 8-13 with the period of the distribution as a parameter. In all cases, the simulated capacitance closely matched the averaged–surface

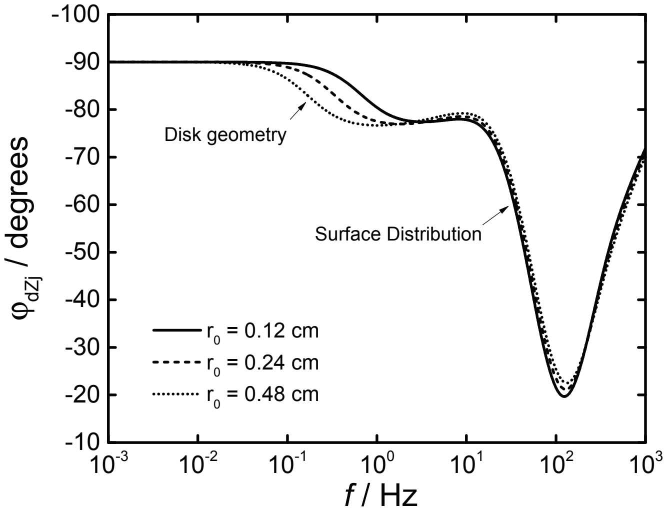

A

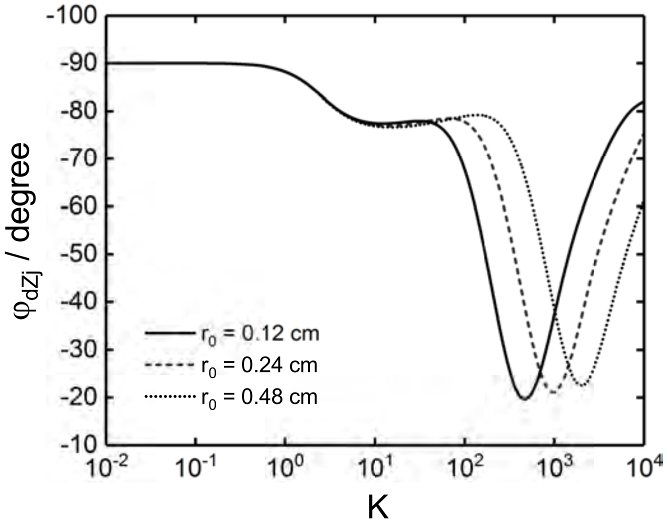

B

Figure 8-11. Imaginary–impedance–derived phase angles values calculated from the impedance data with the disk radius as a parameter: a) imaginary–impedance–derived phase angle as a function of frequency; b) imaginary–impedance–derived phase angle as a function of dimensionless frequency $K = \omega \langle C_0 \rangle r_0 / \kappa$

.

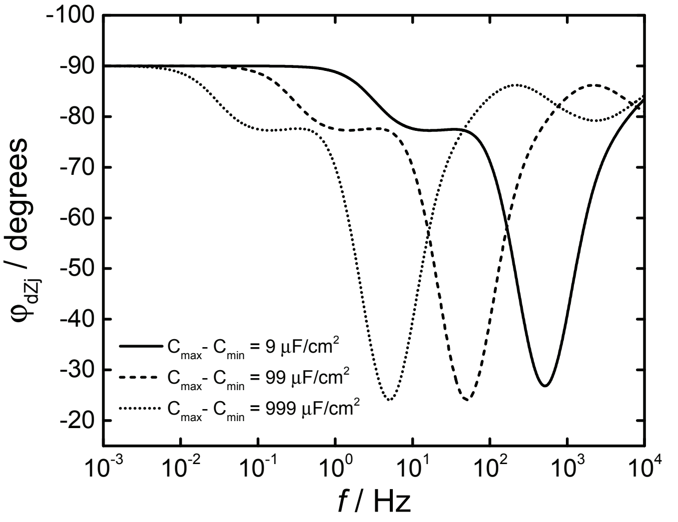

A

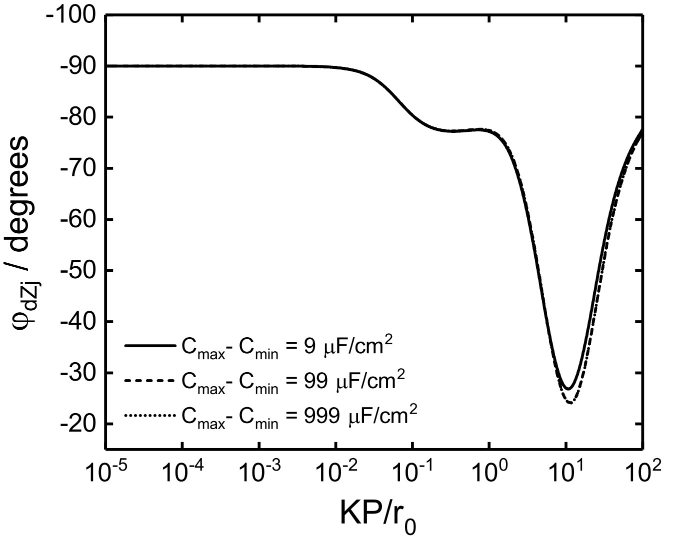

B

Figure 8-12. Imaginary–impedance–derived phase angle calculated from impedance data on disk electrodes with a radial distribution of capacitance with the amplitude of the square wave as a parameter: a) phase angle as a function of frequency; b) phase angle as a function of dimensionless frequency based on the averaged capacitance and the period of the square wave as the characteristic length.

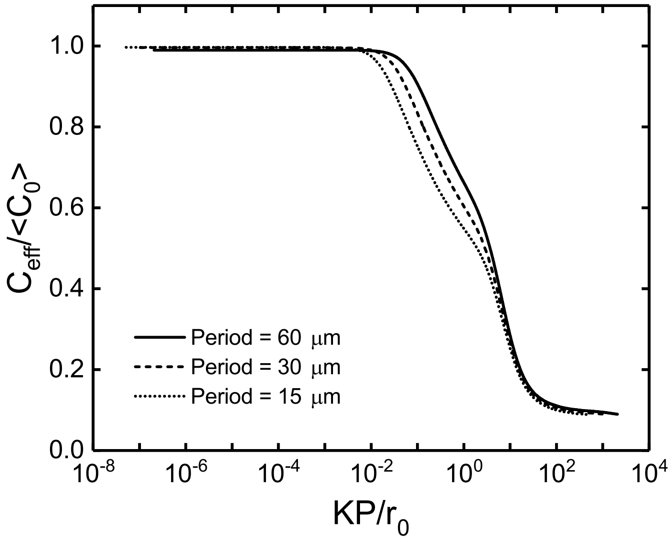

Figure 8-13. The ratio of the calculated effective capacitance and the surface–averaged input capacitance as a function of dimensionless frequency KP/r_0 with the period of the distribution as a parameter for disk electrodes within an insulating plane.

capacitance of the electrode at low frequencies, indicated by a capacitance ratio value equal to 1. At high frequencies, an initial decrease of the capacitance ratio was caused by the nonuniform current distribution on the disk surface. At a dimensionless frequency equal to one, a further decrease was observed due to the capacitance heterogeneity.

The characteristic frequency at which frequency dispersion occurs for a planar disk electrode exhibiting a distribution of capacitance may be expressed as

$$f_{c,r_0} = \frac{2\kappa}{\pi^2 \langle C_0 \rangle r_0} \tag{8–13}$$

where $\langle C_0 \rangle$ represents the surface-averaged capacitance. The characteristic frequency at which frequency dispersion begins due to the capacitance distribution may be expressed as

$$f_{c,P} = \frac{\kappa}{2\pi \langle C_0 \rangle P} \tag{8–14}$$

in which the period of the distribution is the characteristic length associated with the distribution. The frequency at which dispersion begins is presented in Figure 8-14 as a function of both the disk radius as well as the period of the capacitance distribution

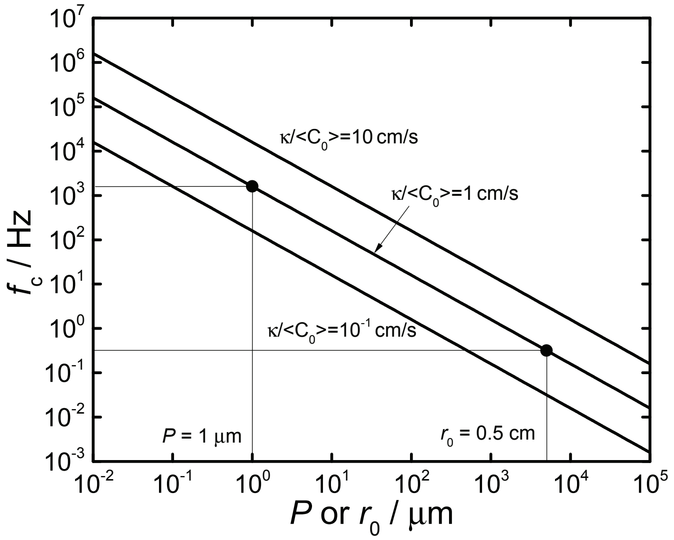

Figure 8-14. The frequency KP/r_0=1 at which the surface heterogeneity influences the impedance as a function of distribution period and disk radius with $\kappa/\langle C_0\rangle$ as a parameter.

with the ratio, $\kappa/\langle C_0\rangle$, as a parameter. The period of the distribution may be associated with the average width of grain sizes within a noncrystalline surface. For a 0.5 cm radius electrode in a system with $\kappa/\langle C_0\rangle = 1$ cm/s (corresponding for example, to $\langle C_0\rangle = 20$ μF/cm^2 and a 0.16 mM sodium chloride concentration) and an average grain size of 1 μm, the frequency at which dispersion occurs due to the disk geometry is 400 mHz while the frequency at which dispersion occurs due to the nonuniform capacitance is 1.6 kHz. The frequency dispersion due to the capacitance distribution will always occur at greater frequencies than the frequency dispersion due to the disk geometry.

CHAPTER 9
INFLUENCE OF REACTIVITY DISTRIBUTION ON IMPEDANCE

Electrical circuits invoking constant-phase elements (CPE), i.e.,

$$Z = R_{\mathrm{e}} + \frac{R_{\mathrm{t}}}{1 + (\mathrm{j}\omega)^{\alpha} Q R_{\mathrm{t}}} \tag{9–1}$$

are often used to fit impedance data arising from a broad range of experimental systems. Equation (9–1) is expressed in terms of an ohmic resistance R_{e}, a charge–transfer resistance R_{t} and CPE parameters α and Q. When $\alpha = 1$, the parameter Q has units of capacitance; otherwise, Q has units of $\mathrm{s}^{\alpha}/\Omega\mathrm{cm}^2$ or $\mathrm{F/s}^{(1-\alpha)}\mathrm{cm}^2$ [57]. The physical origin of the CPE has been described as being associated with a distribution of time constants through a film or along an electrode surface. The frequency dispersion associated with a distribution of time constants normal to the electrode surface is well established; whereas, the frequency dispersion associated with a surface distribution is less well understood. Hirschorn et al. [24, 25] showed that a power–law distribution of resistivity through a film yields CPE behavior. The power–law–model approach has been used successfully to extract a film capacitance and associated parameters for a variety of systems, including oxides on steel,[58] human skin,[58, 74] and polymer coatings.[48, 52]

Brug et al. [12] developed an expression for the capacitance extracted from a CPE caused by a surface distribution of capacitance. Córdoba-Torres et al. [15] showed that the Brug model explained the correlation observed between CPE parameters α and Q for two experimental conditions: the corrosion of polycrystalline iron and the deposition of $\mathrm{CaCO_3}$ scale on gold electrodes. The results were attributed to a distribution of time constants associated with surface heterogeneity. The exact nature of the surface heterogeneity was not identified. In subsequent work, Córdoba-Torres et al. [16] suggested that the CPE behavior results from energetic distributions rather than geometric heterogeneity or roughness.

Ring electrodes were studied by Chen et al. [14] to determine the characteristic frequency at which frequency dispersion is induced due to the geometry of the ring. The current near the inner and outer edges of a ring electrode approaches infinity. Chen et al. [14] determined empirically an approximation of the characteristic length to be

$$\ell_{\mathrm{c,ring}} = \frac{r_2 - r_1}{1 + (r_1/r_2)^2} \tag{9–2}$$

where the width of the ring was scaled by a term which approached 0.5 as r_1 approached r_2 and unity as r_1 tends to 0. This expression works best for intermediate values of r_1/r_2.

Alexander et al. [4] identified the characteristic dimension associated with roughness expressed as

$$\ell_{\mathrm{c,rough}} = f_{\mathrm{r}}^2 P \tag{9–3}$$

in which P was defined as the period of the roughness or the average width of a rough groove. They showed that roughness consistent with even poorly polished electrodes does not lead to time–constant dispersion in the frequency range used for electrochemical measurements.

Alexander et al. [5] showed that a capacitance distribution gave rise to frequency dispersion, but that the effect was seen at frequencies higher than that associated with the disk geometry. The characteristic length for a periodic distribution as a function of the radial coordinate was the period of the distribution such that

$$\ell_{\mathrm{c,cap}} = P \tag{9–4}$$

and, as the period decreased, the frequency dispersion occurred at higher frequencies.

The object of the present work is to explore the type of surface heterogeneity that can lead to a Brug–style CPE. As was previously described, surface roughness and geometric considerations did not lead to CPE behavior. Nor did a distribution of capacitance. This paper addresses the question of how a distribution of reactivity affects the impedance response and whether this form of heterogeneity can lead to a CPE response.

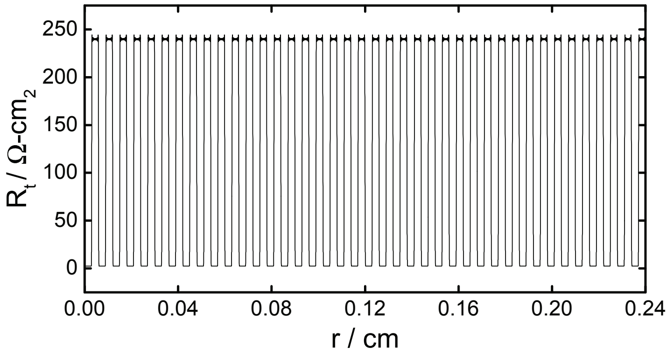

Figure 9-1. Reactivity distribution as a function of radial position based on a square wave represented by a Fourier series with a period of 60 μm.

9.1 Mathematical Development & Impedance calculations

A reactivity distribution was simulated by a charge-transfer resistance distribution. A Fourier series was used to represent a square wave, shown in Figure 9-1 as a function of radial position. The Fourier series was expressed as

$$R_{\mathrm{t}}(r) = \langle R_{\mathrm{t}} \rangle + \sum_{n=1}^{\infty} (R_{\mathrm{t,max}} - R_{\mathrm{t,min}}) cos(2n\pi P) \tag{9–5}$$

where the constants $R_{\mathrm{t,max}}$ and $R_{\mathrm{t,min}}$ represented the maximum and minimum scaled values of reactivity. The average reactivity of the electrode surface $\langle R_{\mathrm{t}} \rangle$ was calculated as

$$\langle R_{\mathrm{t}} \rangle = \frac{2}{r_0^2} \int_0^{r_0} R_{\mathrm{t}}(r) r dr \tag{9–6}$$

in which the reactivity as a function of the radial position was integrated over the surface of the electrode and divided by the area of the electrode. The period of the square wave may represent an elemental grain size in which the reactivity is assumed to be relatively uniform across a grain and to then jump to another value at an adjacent grain. The Fourier series was truncated after 20 terms.

The potential distribution within an electrolyte domain with uniform composition is governed by Laplace's equation

$$\nabla^2 \Phi = 0 \tag{9–7}$$

A two-dimensional axial symmetric coordinate system was used in which the potential was assumed to be independent of the angular coordinate. The potential was separated into steady-state and oscillating components as

$$\Phi = \bar{\Phi} + \mathrm{Re}\left\{\tilde{\Phi}\exp(\mathrm{j}\omega t)\right\} \tag{9–8}$$

where $\bar{\Phi}$ represents the steady-state portion and $\tilde{\Phi}$ represents the complex oscillating portion that is a function of frequency and position but independent of time. The same relationship for the potential applied to the electrode can be expressed as

$$V = \bar{V} + \mathrm{Re}\left\{\tilde{V}\exp(\mathrm{j}\omega t)\right\} \tag{9–9}$$

At $r = 0$, for all y, the symmetry condition $\partial\tilde{\Phi}/\partial r = 0$ was assumed to apply. Far from the electrode, as $\sqrt{r^2 + y^2} \to \infty$, $\tilde{\Phi} \to 0$. This condition places the counterelectrode infinitely far from the working electrode.

The normal flux at the surface of the electrode exhibiting faradaic reactions was expressed as

$$i = C_0\frac{\partial(V - \Phi_0)}{\partial t} + \frac{(\alpha_a + \alpha_c)i_0F}{RT}(V - \Phi_0) = -\kappa\frac{\partial\Phi}{\partial y}\bigg|_{y=0} \tag{9–10}$$

where C_0 is the capacitance on the electrode surface, κ is the conductivity of the electrolyte, and Φ_0 is the potential outside the diffuse part of the electrode double layer.[27]

The oscillating current density was converted to the frequency domain such that

$$\tilde{i} = \mathrm{j}\omega C_0(\tilde{V} - \tilde{\Phi}) + \frac{(\alpha_a + \alpha_c)i_0F}{RT}(\tilde{V} - \tilde{\Phi}) \tag{9–11}$$

where $\tilde{V}$ is the potential perturbation at the electrode and $\tilde{\Phi}$ is the complex oscillating potential within the electrolyte.

The charge-transfer resistance may be expressed as

$$R_t = \frac{RT}{(\alpha_a + \alpha_c)i_0F} \tag{9–12}$$

Equation 9–11 was then expressed as

$$\tilde{i} = \mathrm{j}\omega C_0(\tilde{V} - \tilde{\Phi}) + \frac{1}{R_t}(\tilde{V} - \tilde{\Phi}) \tag{9–13}$$

In order to observe deviations from an expected response it is useful to express data in dimensionless form. Throughout this paper, the impedance is scaled by the ohmic resistance. Simulations were performed for both disk and recessed disk electrodes. In 1963, Kelman[34] solved a steady-state diffusion problem for flow through a cylindrical pore into an infinite domain. West and Newman[73] applied his solution to formulate a mathematical equivalent to the ohmic resistance of a recessed electrode as

$$R_{\mathrm{e,rec}} = \frac{\pi r_0}{4\kappa} + \frac{l}{\kappa} + \frac{\pi r_0 h_{\mathrm{a}}(l/r_0)}{\kappa} \tag{9–14}$$

where l is the depth of the recess. The first term represents the ohmic resistance to a disk electrode and the second term is the resistance through the cylindrical recessed region. The third term represents a correction factor which Kelman solved using Bessel functions and asymptotic matching. West and Newman determined from Kelman's solutions that $h_{\mathrm{a}}(l/r_0) \propto (l/r_0)\ln(l/r_0)$ as l/r_r0 approaches 0. The upper limit $h_{\mathrm{a}}(l/r_0)$ is 0.011 and applies for (l/r_0) greater than 0.5. For the present simulations, $(l/r_0) = 3$, such that $h_{\mathrm{a}}(l/r_0) = 0.011$

9.2 Results

The effect of a nonuniform distribution of reactivity may be observed in Figure 9-2A for a recessed electrode. The simulated real impedance was scaled by the ohmic resistance of the recessed electrode. The average charge–transfer resistance and the period of the distribution were treated to be parameters. The largest period simulated, $P = 60$ μm, showed the largest variation in the low-frequency asymptote of the real impedance, used to determine the charge-transfer resistance. However, the variation was minuscule and would not greatly influence the interpretation of the impedance. The imaginary impedance scaled by the ohmic resistance of the recessed electrode is presented in Figure 9-2B as a function

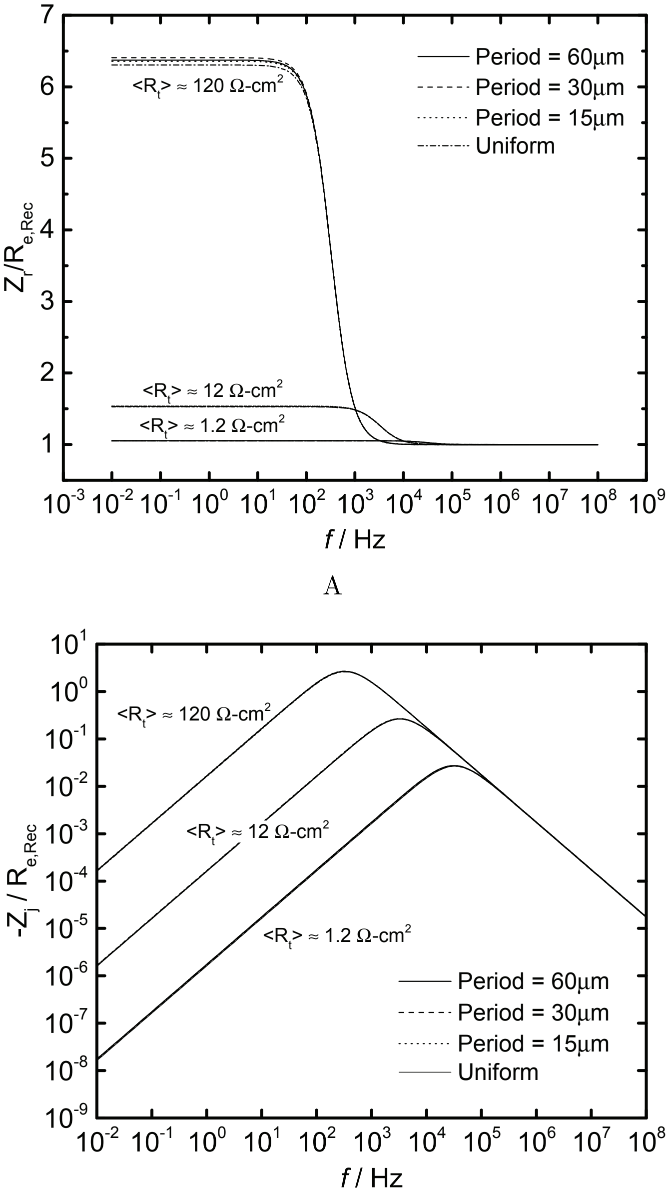

A

B

Figure 9-2. Global impedance scaled by the ohmic resistance of a recessed electrode with a square–wave distribution of capacitance as a function of frequency with the period and averaged charge–transfer resistance as parameters: a) real impedance; b)imaginary impedance.

of frequency in log-log scale. The variations in the real impedance shown in Figure 9-2A are not visible in the plot format of Figure 9-2B.

An adjusted phase angle may be expressed as

$$\varphi_{\mathrm{adj}} = \arctan \frac{Z_{\mathrm{j}}}{Z_{\mathrm{r}} - R_{\mathrm{e}}} \tag{9–15}$$

where the ohmic resistance is subtracted from the real part of the impedance. The adjusted phase angle is presented in Figure 9-3A as a function of frequency for the results presented in Figure 9-2. The results do not show signs of frequency dispersion. The low and high–frequency limits of the phase angle were 0° and -90° respectively, indicating a purely RC response. For a faradaic reaction, the dimensionless frequency depends on the charge–transfer resistance of the reaction taking place and does not involve the ohmic resistance. Therefore, the dimensionless frequency may be expressed as

$$KR_{\mathrm{t}}/R_{\mathrm{e}} = \omega C_0 \langle R_{\mathrm{t}} \rangle \tag{9–16}$$

in which the surface–averaged charge–transfer resistance is scaled by the impedance associated with the interfacial capacitance. The adjusted–phase angle is presented in Figure 9-3B as a function of dimensionless frequency. All of the simulated data associated with different combinations of periods and averaged charge–transfer resistances are superposed and the inflection point, or the point at which the phase angle was equal to $-45°$ occurred at dimensionless frequency $KR_{\mathrm{t}}/R_{\mathrm{e}} = 1$.

9.3 Discussion

The nonuniform reactivity lowered the global effective charge-transfer resistance with increases in the period of the distribution. This behavior is not associated with frequency dispersion because, as shown in Figure 9-3B, the phase angle calculations superposed with those determined from an electrode with a uniform charge-transfer resistance. Frequency dispersion is dependent on the $R_{\mathrm{e}}C$ time constant. All geometric effects including the disk and ring geometry as well as roughness influence the ohmic resistance, R_{e}. The

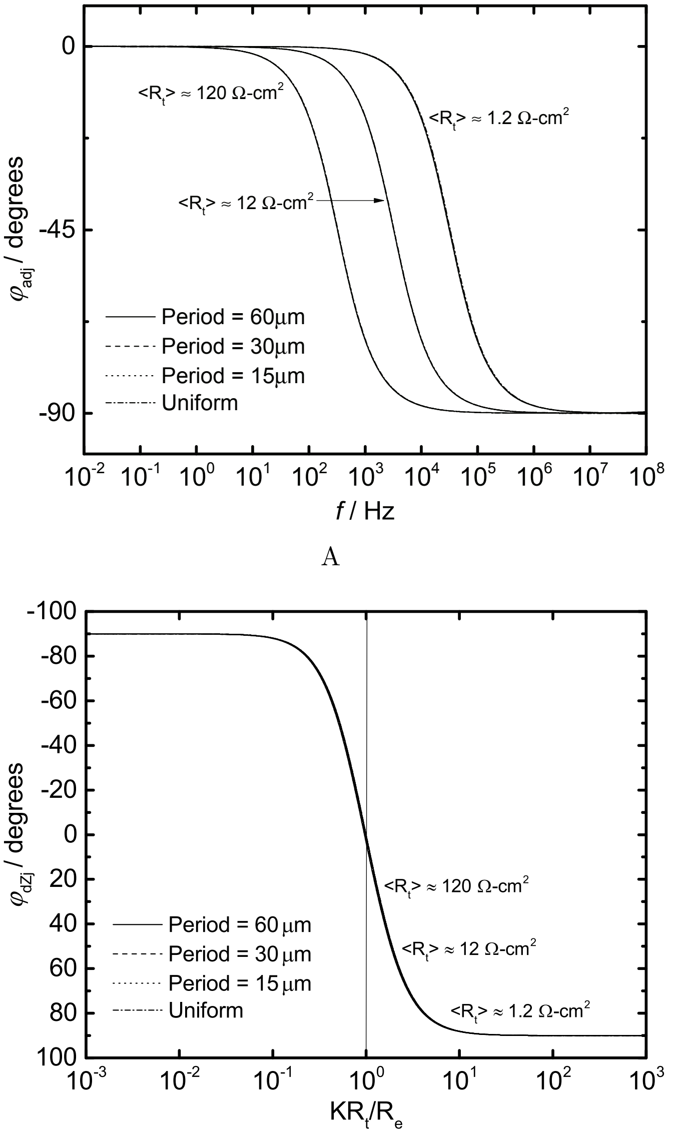

A

B

Figure 9-3. Imaginary–impedance–derived phase angle for a recessed electrode with the period and averaged charge–transfer resistance as parameters: a) phase angle as a function of frequency; b) phase angle as a function of dimensionless frequency based on the averaged charge–transfer resistance.

capacitance distribution directly effects the capacitance, C. The reactivity distribution does not influence the impedance significantly because neither R_e nor C are affected.

For each form of surface heterogeneity there exists a characteristic frequency at which dispersion is induced. The characteristic frequency is inversely proportional to the characteristic length associated with the type of surface heterogeneity. As the characteristic length decreases, the frequency dispersion shifts to higher frequencies. The reactivity distribution did not produce a frequency dispersion and therefore a characteristic length is not applicable. However, as the period of the distribution increased, the difference in the asymptotic value of the real impedance at low frequency increased. For a disk electrode within an insulating plane, the characteristic length is the radius of the disk. An approximate characteristic length of a ring electrode can be expressed as a function of the width of the ring. For surface roughness, the characteristic length is the product of the square of the roughness factor and the period of the surface irregularities. The characteristic length which describes a distribution of capacitance is the period of the distribution. In all of these cases, the characteristic length is small, leading to frequency dispersions that occur at the upper limit or outside the measurable frequency range.

Brug derived a formula which relates the parameters of a constant–phase element to an effective capacitance under the premise the constant–phase element was due to a surface distribution of time constants. While the Brug formula has been used to explain the correlation between CPE parameters α and Q, the results presented here suggest a surface distribution of ohmic resistance, capacitance or reactivity will not cause constant–phase element behavior over a wide range of frequencies.

CHAPTER 10
INFLUENCE OF NONUNIFORM REACTION RATES ASSOCIATED WITH REACTIONS COUPLED BY AN ADSORBED INTERMEDIATE ON IMPEDANCE

The influence of reactions coupled by an adsorbed intermediate on impedance measurements of disk electrodes was explored to determine how a surface distribution of rate constants for reactions coupled by an adsorbed intermediate influence the impedance. Finite element models were used to simulate the impedance of disk and recessed disk electrodes with and without surface heterogeneity of reaction rates. Results from finite–element simulations on disk and recessed disk electrodes show that there are two components that give rise to frequency dispersion. Frequency dispersion occurs due to nonuniform current distributions which leads to a complex ohmic impedance. Frequency dispersion also occurs due to the potential dependence of the faradaic impedance. Simulation results show that for disk electrodes embedded within an insulated plane, the interfacial frequency dispersion may be reduced with the use of small electrodes.

10.1 Mathematical Development

The system under consideration involves two reactions coupled by an adsorbed ion. In the first step,

$$\mathrm{M} \rightarrow \mathrm{X_{ads}}^{+} + e^{-} \qquad (10\text{–}1)$$

where the metal reacts to form a adsorbed ion on the surface, an electron is released. In the second step,

$$\mathrm{X_{ads}}^{+} \rightarrow \mathrm{P}^{2+} + e^{-} \qquad (10\text{–}2)$$

where the adsorbed ion desorbs, another electron is released. The total faradaic current may be expressed as the sum of the currents associated with reactions (10–1) and (10–2)

$$i_{\mathrm{F}} = i_{\mathrm{M}} + i_{\mathrm{X}}. \qquad (10\text{–}3)$$

Under the assumption of Tafel kinetics, the current associated with the first step may be expressed as

$$i_{\mathrm{M}} = K_{\mathrm{M}}(1-\gamma)\exp[b_{\mathrm{M}}(V-\Phi_0)] \tag{10–4}$$

and is dependent on the available surface that is not covered by the adsorbed species. A similar expression may be expressed for the second step as

$$i_{\mathrm{X}} = K_{\mathrm{X}}\gamma\exp[b_{\mathrm{X}}(V-\Phi_0)] \tag{10–5}$$

where K_{M} and K_{X} are the effective rate constants with units of current density, γ is the fractional surface coverage of the adsorbed intermediate, b_{M} and b_{X} are constants which can be expressed in terms odd transfer functions, α_{M} and α_{X}, as

$$b = \frac{\alpha F}{RT}. \tag{10–6}$$

The electrode potential is represented by V and Φ_0 is the potential in solution adjacent to the electrode surface.

All oscillating variables may be expressed as a sum of a steady-state and time-dependent components as

$$X = \overline{X} + \mathrm{Re}\{\widetilde{X}\exp(\mathrm{j}\omega t)\} \tag{10–7}$$

in which $\widetilde{X}$ is a complex variable dependent on frequency. Therefore, the faradaic current may be expressed as

$$i_{\mathrm{F}} = \overline{i}_{\mathrm{F}} + \mathrm{Re}\{\widetilde{i_{\mathrm{F}}}\exp(\mathrm{j}\omega t)\} \tag{10–8}$$

in which $\widetilde{i_{\mathrm{F}}}$ is the oscillating component of the faradaic current. The total steady-state faradaic current may be expressed as

$$\overline{i}_{\mathrm{F}} = K_{\mathrm{M}}(1-\overline{\gamma})\exp[b_{\mathrm{M}}(\overline{V}-\overline{\Phi}_0)] + K_{\mathrm{X}}\overline{\gamma}\exp[b_{\mathrm{X}}(\overline{V}-\overline{\Phi}_0)] \tag{10–9}$$

and is dependent on the steady-state surface coverage $\overline{\gamma}$. The steady-state surface coverage may be derived by taking the rate of change in surface coverage over time expressed as

$$\frac{\partial \gamma}{\partial t} = \frac{\overline{i}_{\mathrm{M}} - \overline{i}_{\mathrm{X}}}{\Gamma F} = 0 \tag{10–10}$$

yielding

$$\overline{\gamma} = \frac{K_{\mathrm{M}} \exp[b_{\mathrm{M}}(\overline{V} - \overline{\Phi}_0)]}{K_{\mathrm{M}} \exp[b_{\mathrm{M}}(\overline{V} - \overline{\Phi}_0)] + K_{\mathrm{X}} \exp[b_{\mathrm{X}}(\overline{V} - \overline{\Phi}_0)]} \tag{10–11}$$

The charge-transfer resistance associated with each reaction step is inversely related to the steady state current as

$$R_{\mathrm{t,M}} = \frac{1}{b_{\mathrm{M}} \overline{i}_{\mathrm{M}}} \tag{10–12}$$

and

$$R_{\mathrm{t,X}} = \frac{1}{b_{\mathrm{X}} \overline{i}_{\mathrm{X}}} \tag{10–13}$$

respectively. The total charge-transfer resistance is the parallel combination of the charge-transfer resistances of each reaction expressed as

$$\frac{1}{R_{\mathrm{t}}} = \frac{1}{R_{\mathrm{t,M}}} + \frac{1}{R_{\mathrm{t,X}}} \tag{10–14}$$

The oscillating faradaic current density is derived by differentiating the steady current with respect to potential and surface concentration as

$$\widetilde{i}_{\mathrm{F}} = \left(\frac{\partial \overline{i}_{\mathrm{F}}}{\partial V}\right)_{\overline{\gamma}} \widetilde{V} + \left(\frac{\partial \overline{i}_{\mathrm{F}}}{\partial \gamma}\right)_{\overline{V}} \widetilde{\gamma} \tag{10–15}$$

or

$$\widetilde{i}_{\mathrm{F}} = \left(\frac{1}{R_{\mathrm{t}}}\right) (\widetilde{V} - \widetilde{\Phi_0}) + \left[K_{\mathrm{X}} \exp[b_{\mathrm{X}}(\overline{V} - \overline{\Phi}_0)] - K_{\mathrm{M}} \exp[b_{\mathrm{M}}(\overline{V} - \overline{\Phi}_0)]\right] \widetilde{\gamma} \tag{10–16}$$

Following

$$\Gamma \frac{\mathrm{d}\gamma}{\mathrm{d}t} = \frac{i_{\mathrm{M}}}{\mathrm{F}} - \frac{i_{\mathrm{X}}}{\mathrm{F}} \tag{10–17}$$

the oscillating component of the surface coverage can be expressed as

$$\Gamma F \, \mathrm{j}\omega \widetilde{\gamma} = \left(\frac{1}{R_{\mathrm{t,M}}} - \frac{1}{R_{\mathrm{t,X}}}\right) \widetilde{V} - \left(K_{\mathrm{X}} \exp\left(b_{\mathrm{X}} \overline{V}\right) + K_{\mathrm{M}} \exp\left(b_{\mathrm{M}} \overline{V}\right)\right) \widetilde{\gamma} \tag{10–18}$$

yielding

$$\widetilde{\gamma} = \left(\frac{\dfrac{1}{R_{\mathrm{t,M}}} - \dfrac{1}{R_{\mathrm{t,X}}}}{\Gamma F \mathrm{j}\omega + \left(K_{\mathrm{X}} \exp\left(b_{\mathrm{X}}\overline{V}\right) + K_{\mathrm{M}} \exp\left(b_{\mathrm{M}}\overline{V}\right)\right)} \right) \widetilde{V} \tag{10–19}$$

The faradaic admittance may be derived by taking the ratio of the oscillating faradaic current and the electrode potential, i.e., ,

$$Y_{\mathrm{F}} = \frac{\widetilde{i}_{\mathrm{F}}}{\widetilde{V}} \frac{1}{Rt} + \frac{\left(R_{\mathrm{t,M}}^{-1} - R_{\mathrm{t,X}}^{-1}\right)\left(K_{\mathrm{X}} \exp[b_{\mathrm{X}}(\overline{V} - \overline{\Phi}_0)] - K_{\mathrm{M}} \exp[b_{\mathrm{M}}(\overline{V} - \overline{\Phi}_0)]\right)}{\Gamma F \mathrm{j}\omega + K_{\mathrm{X}} \exp[b_{\mathrm{X}}(\overline{V} - \overline{\Phi}_0)] + K_{\mathrm{M}} \exp[b_{\mathrm{M}}(\overline{V} - \overline{\Phi}_0)} \tag{10–20}$$

Equation (10–20) may be expressed as to a faradaic impedance expressed as

$$Z_{\mathrm{F}} = \left(\frac{1}{R_{\mathrm{t}}} + \frac{A}{\mathrm{j}\omega + B} \right)^{-1} \tag{10–21}$$

in which variables A and B are expressed as

$$A = \frac{\left(R_{\mathrm{t,M}}^{-1} - R_{\mathrm{t,X}}^{-1}\right)\left(K_{\mathrm{X}} \exp[b_{\mathrm{X}}(\overline{V} - \overline{\Phi}_0)] - K_{\mathrm{M}} \exp[b_{\mathrm{M}}(\overline{V} - \overline{\Phi}_0)]\right)}{\Gamma F} \tag{10–22}$$

and

$$B = \frac{K_{\mathrm{X}} \exp[b_{\mathrm{X}}(\overline{V} - \overline{\Phi}_0)] + K_{\mathrm{M}} \exp[b_{\mathrm{M}}(\overline{V} - \overline{\Phi}_0)}{\Gamma F} \tag{10–23}$$

respectively. The impedance of a recessed disk electrode for this system would include an ohmic resistance in series with a double layer capacitance and the faradaic impedance in parallel, as shown in Figure 10-1. Equation (10–21) appears as the parallel combination of R_{t} and an adsorption impedance expressed as

$$Z_{\mathrm{ads}} = \frac{B + \mathrm{j}\omega}{A} \tag{10–24}$$

Equation (10–24) is a mathematical expression that cannot be expressed as an equivalent circuit with defined passive elements when $A < 0$.

The calculated impedance for a recessed electrode is shown in Figure 10-2 for cases where $A = 0$, $A < 0$, and when $A > 0$. When $A = 0$, the faradaic impedance reduces to $Z_{\mathrm{F}} = R_{\mathrm{t}}$ and the interfacial impedance only exhibits one time constant. When $A < 0$, the interfacial impedance shows two capacitive semicircles and when

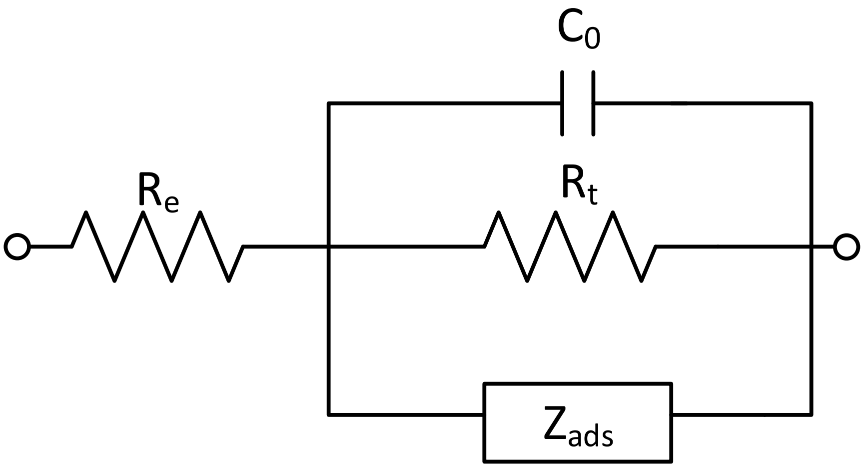

Figure 10-1. Equivalent circuit diagram for a recessed electrode with reactions coupled by an adsorbed intermediate.

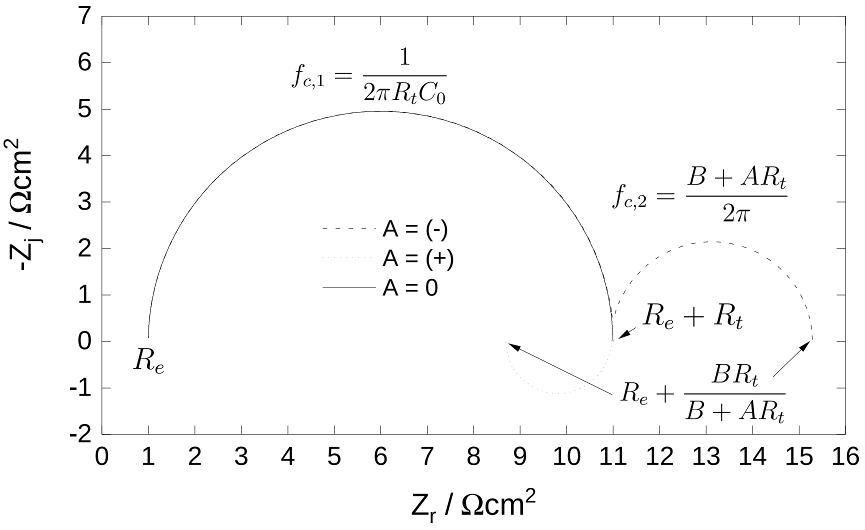

Figure 10-2. Calculated impedance based on an equivalent circuit with the ohmic resistance in series with a double layer capacitor in parallel with the faradaic impedance calculated from Equation (10–21).

$A > 0$, the interfacial impedance has a high-frequency capacitive loop and low-frequency inductive loop such that the low-frequency limit for the capacitive loop is $R_\mathrm{e} + R_\mathrm{t}$. The characteristic frequency of the high-frequency loop is based on the $R_t C_0$ time constant. The characteristic frequency of the low-frequency loop is based on the time constant $\tau = 1/(B + AR_t)$. For all values of A, the same expression provides the low-frequency limit for the impedance.

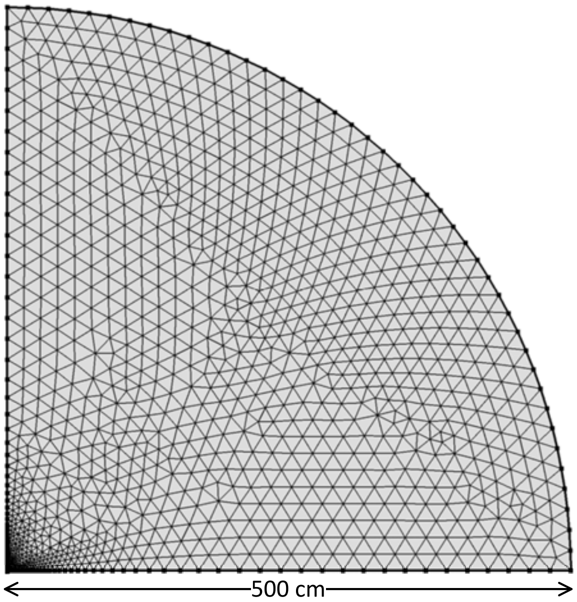

Figure 10-3. The domain for the finite element simulations.

10.2 Finite-Element Model

The impedance was simulated by solving Laplace's equation for the potential distribution in the electrolyte domain, expressed as

$$\nabla^2 \Phi = 0. \tag{10–25}$$

Recalling equation (10–7), the potential may be expressed as

$$\Phi = \overline{\Phi} + \mathrm{Re}\{\widetilde{\Phi} \exp(\mathrm{j}\omega t)\}. \tag{10–26}$$

The electrolyte domain comprised a 2-D axisymmetric quarter of a circle domain, shown in Figure 10-3. The counter electrode was set as the curved boundary with the condition that $\overline{\Phi} = 0$ for the steady-state solution and $\widetilde{\Phi} = 0$ for the oscillating condition. The working electrode was placed on the r-axis centered at $r = 0$. The electrolyte domain was 2000 times larger than the radius of the disk. The boundary condition at the working electrode for the steady-state case was expressed as equation (10–9). The boundary condition at the working electrode for the oscillating case was expressed as

$$\widetilde{i} = (j\omega C_0 + R_{t,M}^{-1} + R_{t,X}^{-1})(\widetilde{V} - \widetilde{\Phi_0}) + K_X \exp(b_X \overline{V})\widetilde{\gamma} - K_M \exp(b_M \overline{V})\widetilde{\gamma} \tag{10–27}$$

where $\widetilde{\gamma}$ may be expressed as

$$\widetilde{\gamma} = \frac{R_{t,M}^{-1} + R_{t,X}^{-1}}{\Gamma F j\omega + (K_M \exp(b_M \overline{V}) + K_X \exp(b_X \overline{V}))(\widetilde{V} - \widetilde{\Phi_0})} \tag{10–28}$$

Equations 10–25, 10–27, and the boundary condition at the counter electrode were solved for a range of frequencies, and the global impedance was calculated as the ratio of the applied perturbation $\widetilde{V}$ and the total oscillating current at the disk electrode, $\widetilde{i}$. The local interfacial impedance may be calculated by probing the oscillating potential in the electrolyte at the disk surface $\widetilde{\Phi}_0$ and may be expressed as

$$z_0(r) = \frac{\widetilde{V} - \widetilde{\Phi_0}(r)}{\widetilde{i}(r)} \tag{10–29}$$

The global interfacial impedance may be found by integrating the local interfacial impedance across the surface of the whole disk. The global ohmic impedance may be calculated as the difference between the global impedance and the global interfacial impedance as $Z_e = Z - Z_0$.

The potential distribution for a disk is nonuniform such that the interfacial impedance, which includes potential-dependent parameters, may not represent the surface-averaged properties. Therefore, the global interfacial impedance is compared in the present work to the impedance calculated with surface averaged parameters where the surface–averaged interfacial impedance may be expressed as

$$\langle Z_0 \rangle = \left(j\omega C_0 + \frac{1}{\langle R_t \rangle} + \frac{\langle A \rangle}{j\omega + \langle B \rangle} \right)^{-1} \tag{10–30}$$

with the interfacial parameters A, B, and R_t calculated based on their local values and averaged over the surface of the disk.

Table 10-1. Simulation Parameters.

Symbol	Meaning	Value	units
b_{M}	$\alpha_{\mathrm{M}}\mathrm{F}/\mathrm{R}T$	40	V^{-1}
b_{X}	$\alpha_{\mathrm{X}}\mathrm{F}/\mathrm{R}T$	10	V^{-1}
K_{M}	Effective reaction constant for Reaction 2	77.2	A cm^{-2}
K_{X}	Effective reaction constant for Reaction 3	0.19	A cm^{-2}
$\overline{V}$	Steady-state electrode potential	-0.038	V
$\widetilde{V}$	Perturbation of electrode potential	10	mV
Γ	Maximum surface coverage of intermediate	2×10^{-6}	$\mathrm{mol/cm}^2$
κ	Electrolyte conductivity	0.0485	S/cm
C_0	Double-layer capacitance	20	$\mu\mathrm{F/cm}^2$

10.3 Results

Finite-element simulations were used to simulate the impedance of disk and recessed disk electrodes with reactions coupled by an adsorbed intermediate. The disk geometry produces a radial potential dependence which influences the impedance response. The recessed electrode was used to analyze the effect of heterogenous reaction rates on the impedance response without the effect of the disk geometry. Steady-state results are presented to show the variation of surface properties on the electrodes, and the impedance results are presented to show the effect of the surface distribution. For the sake of brevity, results are only shown for negative values of A.

10.3.1 Disk Electrode

The angle between the disk electrode surface and the insulating plane is 180° which leads to a greater current density and a lower potential at the edges of the disk than at the center of the disk. Finite-element simulations were performed to solve for the steady-state potential distribution throughout the electrolyte adjacent to the disk electrode. The parameters used in the simulations are presented in Table 10-1 and were chosen to maximize frequency dispersion due to the disk geometry. The surface-averaged current density is shown in Figure 10-4 as a function of the surface overpotential. The current approached zero at more negative potentials.

The surface-averaged value of $\langle A \rangle$ is presented in Figure 10-5 as a function of

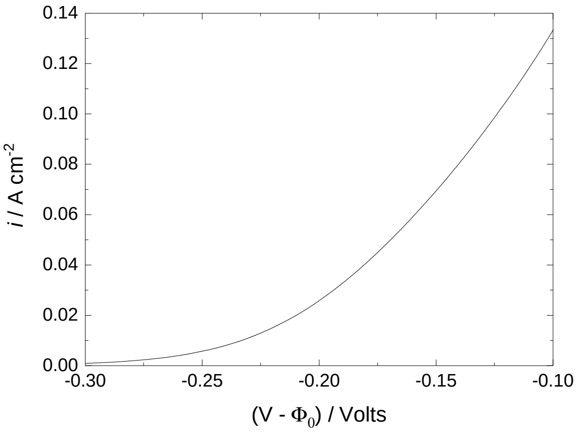

Figure 10-4. Steady state current density as a function of surface overpotential.

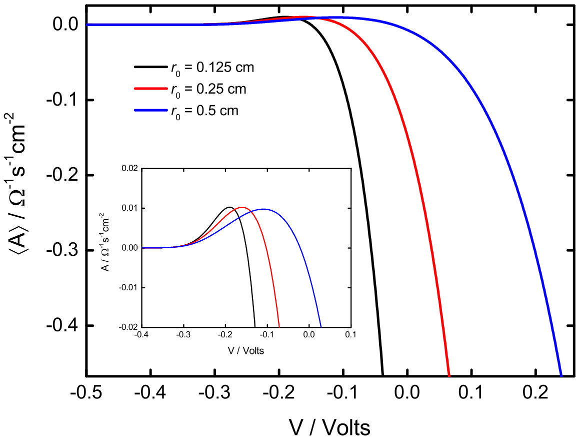

Figure 10-5. Surface-averaged A as a function of potential with disk radius as a parameter.

potential with electrode radius as a parameter. Increases in the disk radius caused the point at which $\langle A \rangle = 0$ to shift to more anodic potentials. The steady-state potential at the electrode surface for a disk electrode is shown in Figure 10-6. The potential at the edge of the disk is significantly lower than the center. The parameters associated with the interfacial impedance are potential dependent except for the double layer capacitance which was assumed to be independent of potential. Therefore, the interfacial parameters, shown in Figure 10-7 also vary along the disk surface. A decreases and becomes more negative at the edges of the disk, while B increases. The charge-transfer resistance also decreases at the edges of the disk.

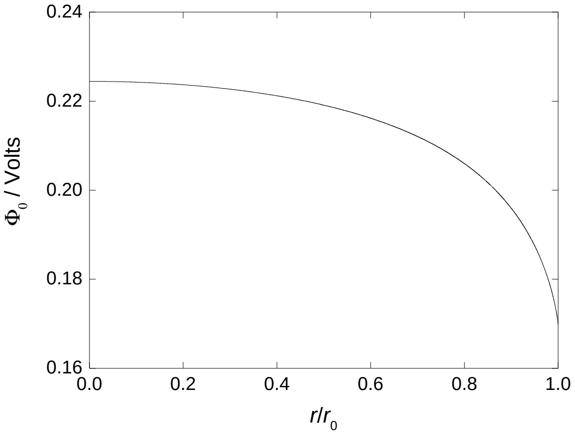

Figure 10-6. Surface potential as a function of radial position.

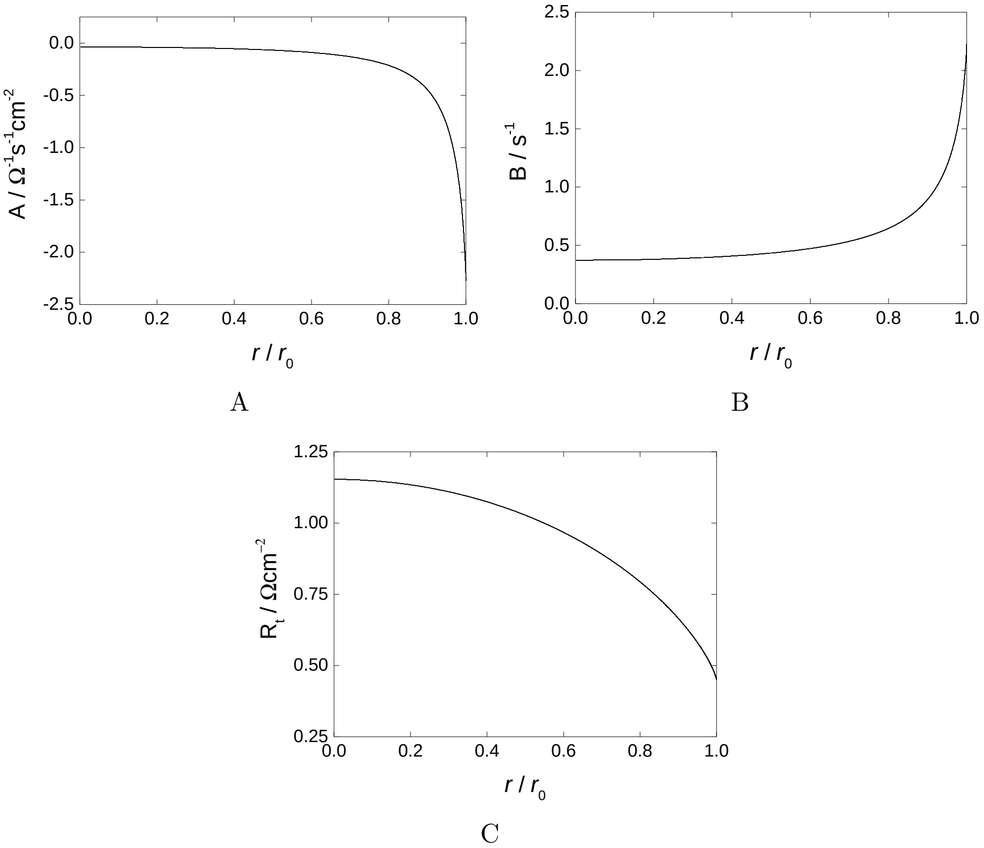

Figure 10-7. Steady-state interfacial parameters as a function of radial position: A)A; B)B; C)R_t

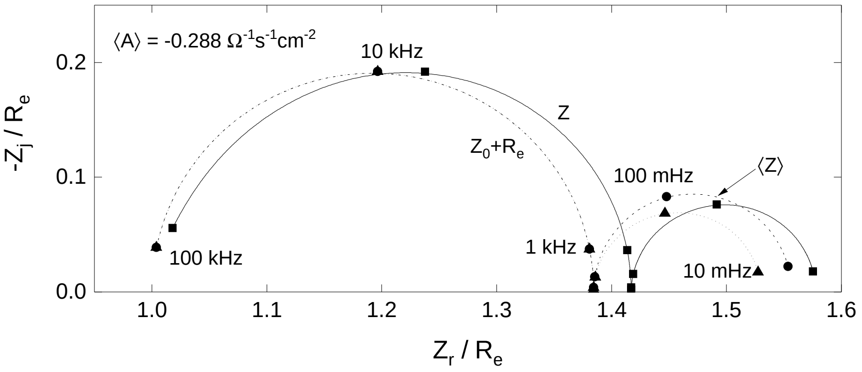

Figure 10-8. Simulated impedance response in Nyquist format of a disk electrode. The solid line represents the global impedance response. The Dashed line represents the surface-averaged interfacial impedance. The dotted line represents the interfacial impedance.

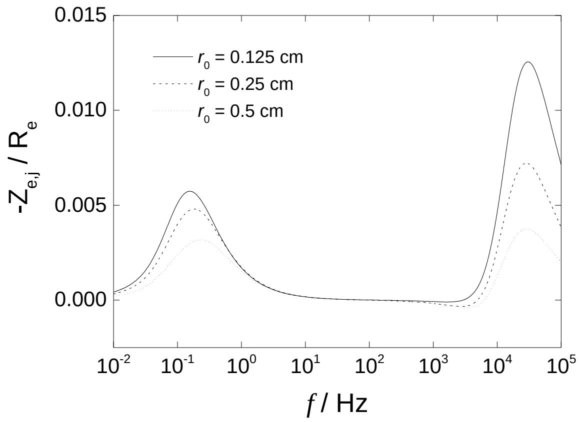

Figure 10-9. The imaginary part of the ohmic impedance scaled by the ohmic resistance as a function of frequency with radius as a parameter.

The simulated global impedance Z scaled by the ohmic resistance $R_\mathrm{e} = \frac{\pi r_0}{4\kappa}$ is shown in Figure 10-8 for $\langle A \rangle = -0.288$. The global impedance is compared to the summation of the interfacial impedance and the ohmic resistance $Z_0 + R_\mathrm{e}$ to show the frequency dispersion caused by the ohmic impedance. This term is compared to the surface-averaged interfacial impedance, equation (10–30), to show that the interfacial impedance also includes frequency dispersion due to the potential dependence of the interfacial parameters.

The imaginary part of the ohmic impedance scaled by the ohmic resistance is shown in Figure 10-9 as a function of frequency with the radius of the disk as a parameter. The

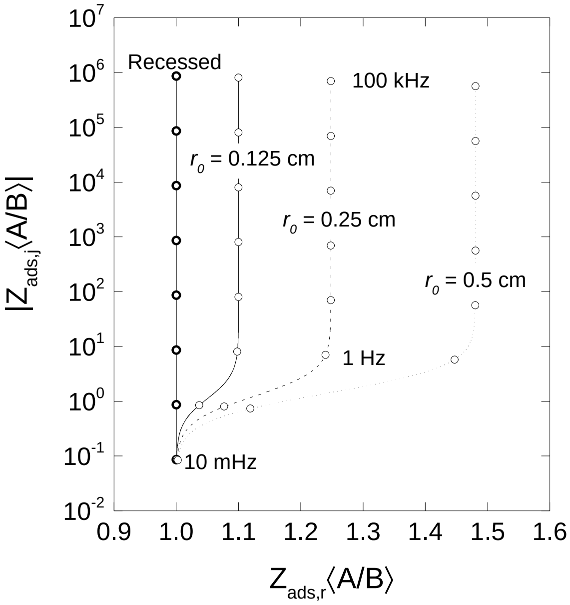

Figure 10-10. The adsorption impedance scaled by the B/A with disk radius as a parameter. The dashed line represents the results without the effect of disk geometry.

global impedance that is measured on a disk electrode includes the ohmic impedance, which does not have relevant physical meaning to the interfacial impedance. Therefore, presence of an ohmic impedance distorts the measured impedance and complicates interpretation. While the ohmic impedance increases with decreases in the size of the disk, the high- and low-frequency time constants are not significantly changed.

The frequency dispersion associated with the interfacial impedance is confined to the faradaic part. The amount of frequency dispersion may be revealed by analysis of the capacitive part of the faradaic impedance referred to in this paper as the adsorption impedance, equation (10–24). The absolute value of the imaginary part of the adsorption impedance scaled by the ratio B/A is presented in Figure 10-10 as a function of the real part of the adsorption impedance, also scaled by the B/A, with the radius of the disk as a parameter. The imaginary part of the impedance is shown in log-scale to reveal the variation in impedance at low frequencies, shown in the lower-left-hand corner of the figure. The frequency dispersion of the adsorption impedance increases as the disk radius increases.

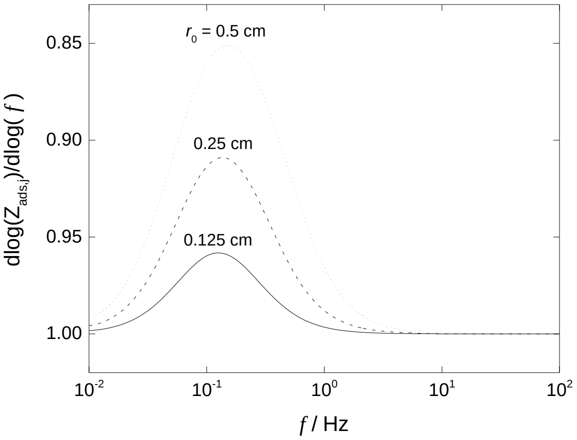

Figure 10-11. The derivative of the logarithm of the imaginary part of the adsorption impedance with respect to the logarithm of frequency as a function of frequency with the radius as a parameter.

The derivative of the logarithm of the imaginary part of the adsorption impedance with respect to the logarithm of frequency is shown as a function of frequency in Figure 10-11 with the radius of the disk as a parameter. Frequency dispersion is shown for values which deviate from unity. Therefore, as the radius of the disk electrode increases, the amount of frequency dispersion associated with the interfacial impedance increases. The total amount of frequency dispersion contained within the global impedance is a combination of the interfacial dispersion and the dispersion caused by the ohmic impedance. The ohmic impedance increases as the radius of the disk decreases and the interfacial dispersion decreases as the radius of the disk decreases. The overall frequency dispersion is minimized by using small disk electrodes but unlike the case for a blocking disk electrode, the characteristic frequency associated with the frequency dispersion is not dependent on the size of the disk.

10.3.2 Recessed Electrode

The rate constants associated with the reaction mechanism may vary along the surface of a polycrystalline electrode. To determine the effect of this form of surface heterogeneity, a recessed electrode was used to analyze the effect on the impedance response without the effect of the disk geometry. The rate constants associated with the

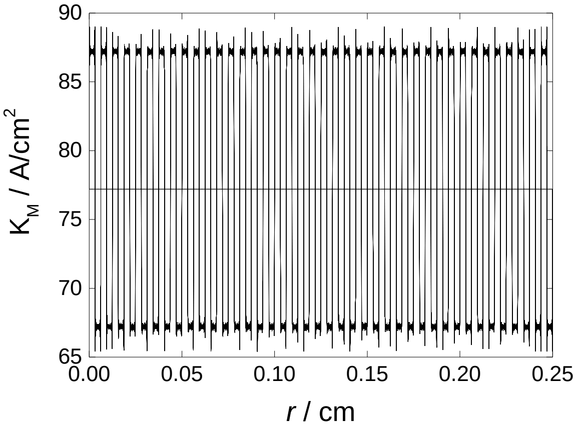

Figure 10-12. Effective rate constant for Reaction 10–1 as a function of radial position.

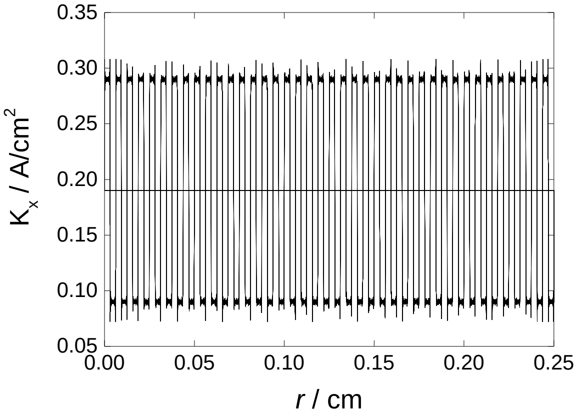

Figure 10-13. Effective rate constant for Reaction 10–2 as a function of radial position.

first and second elementary steps are shown in Figures 10-12 and 10-13 as a function of radial position. The rate constants were varied around a mean value following a square-wave distribution. The square wave form was calculated using a Fourier series with a specified period and amplitude.

The imaginary part of the ohmic impedance scaled by the ohmic resistance is shown in Figure 10-14 with the period of the heterogeneity as a parameter. The ohmic impedance increased as the period of the distribution increased, but the characteristic frequency was not changed. Therefore, the frequency at which the dispersion occurs must be dependent on some other parameter.

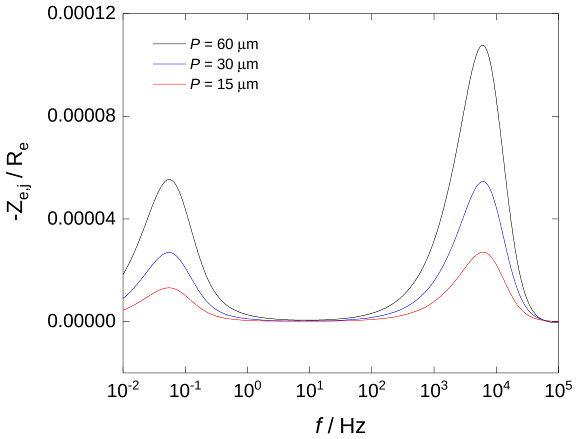

Figure 10-14. Imaginary ohmic impedance scaled by the ohmic resistance as a function of frequency with the period of the distribution as a parameter.

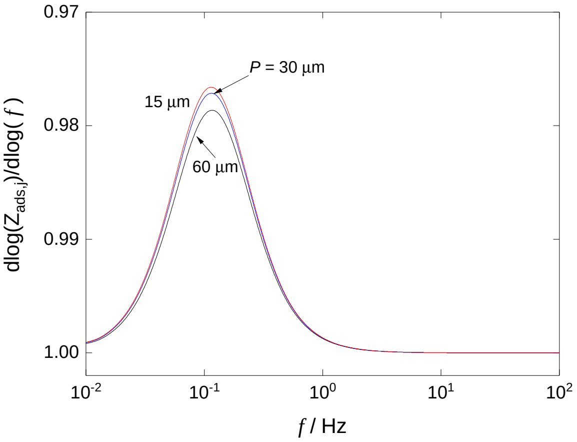

Figure 10-15. The derivative of the logarithm of the imaginary part of the adsorption impedance with respect to the logarithm of frequency as a function of frequency with the period as a parameter.

The derivative of the logarithm of the imaginary part of the adsorption impedance with respect to the derivative of the logarithm of frequency is shown as a function of frequency in Figure 10-15 with the period of the distribution as a parameter. The characteristic frequency associated with the interfacial frequency dispersion did not change with changes in the period of the distribution, and the amount of frequency dispersion increased slightly with decreases in the period of the distribution. The characteristic frequency associated with the surface heterogeneity must be based on the interfacial parameters.

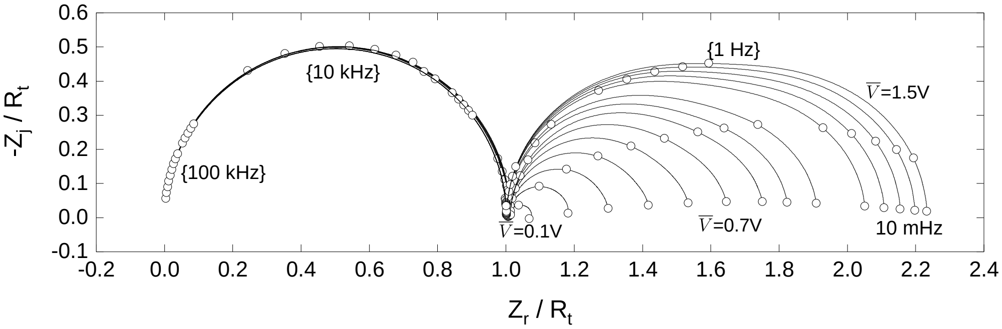

Figure 10-16. The simulated impedance in Nyquist format scaled by the charge transfer resistance R_t with steady state potential as a parameter.

To determine the validity of this concept, simulations were performed at different potentials, therefore, changing the values of the interfacial parameters. The simulated impedance is shown in Figure 10-16, scaled by the surface-averaged charge-transfer resistance. Most of the frequency dispersion is confined to the faradaic impedance which is represented by the low frequency capacitive loop. At $\overline{V} = 0.1$V, an inductive feature is observed that is associated with the variation of A along the surface between positive and negative values. As the potential increased, the frequency dispersion became more significant and the low-frequency loop broadened, reflecting the presence of two distinct time constants. There is minimal frequency dispersion associated with the high frequency time constant.

The derivative of the logarithm of the imaginary part of the adsorption impedance with respect to the derivative of the logarithm of frequency is shown as a function of frequency in Figure 10-17 with $\overline{V}$ as a parameter. As the potential is shifted in the anodic direction, the frequency dispersion occurs at higher frequencies and the magnitude of the dispersion increases.

The derivative of the logarithm of the imaginary part of the adsorption impedance with respect to the logarithm of frequency is shown in Figure 10-18 as a function of a dimensionless frequency based on the interfacial parameters A, B, and R_t with $\overline{V}$ as a parameter. The dimensionless frequency was derived by scaling the impedance by the

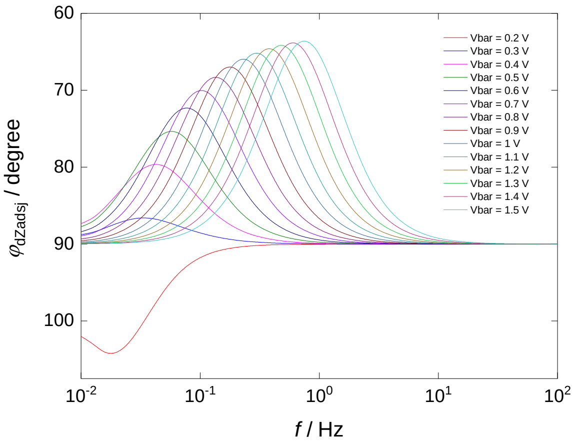

Figure 10-17. The derivative of the logarithm of the imaginary part of the adsorption impedance with respect to the logarithm of frequency as a function of frequency with steady-state potential as a parameter.

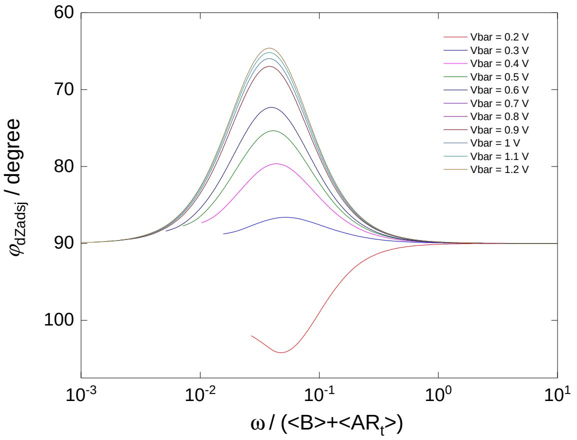

Figure 10-18. The derivative of the logarithm of the imaginary part of the adsorption impedance with respect to the logarithm of frequency as a function of dimensionless frequency with steady-state potential as a parameter.

characteristic frequency associated with the faradaic impedance. This shows that the characteristic frequency associated with the frequency dispersion is strongly dependent on the characteristic frequency of the faradaic impedance.

10.4 Discussion

For systems with a single-step reaction, surface heterogeneity of the rate constant did not induce frequency dispersion.[6] Interestingly, the frequency dispersion associated with the interfacial impedance for systems with reactions coupled by an adsorbed intermediate

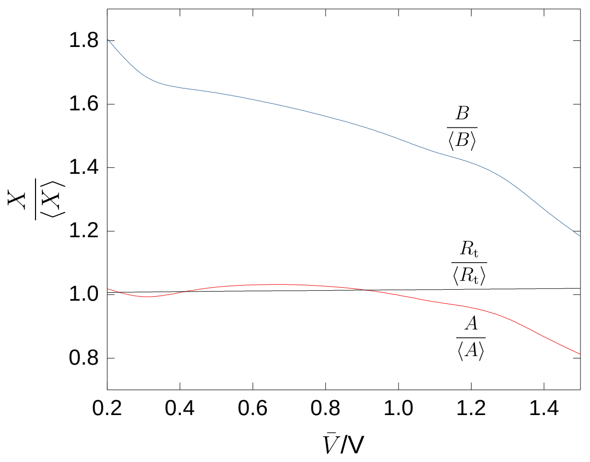

Figure 10-19. Parameters of the faradaic impedance determined from the impedance simulations scaled by the surface averaged parameters as a function of steady state potential.

only occurred at low frequencies where the faradaic impedance is seen. In order to reliably interpret the impedance results for systems with adsorbed intermediates, the characteristic frequencies and limits of the impedance should reflect the surface-averaged interfacial parameters. The characteristic frequencies and the high- and low- frequency limits of the impedance were determined using a measurement model in which a series of Voigt elements was used to fit the impedance. The characteristic frequency of the high-frequency time constant was used to calculate R_t. The adsorption parameters A and B were calculated from the low-frequency limit of the impedance as well as the characteristic frequency of the low-frequency loop.

Each parameter is shown in Figure 10-19 scaled by the surface average value as a function of steady state potential. The charge-transfer resistance scaled by the surface average value did not vary much from unity for all of the potentials simulated. At low potentials, the value of A extracted from the simulations was in agreement with the surface averaged value. However, at larger potentials the value determined from the simulated data was almost 20 percent less than the surface averaged value. The value of B from the simulated impedance cannot be reliably determined from the impedance as there was a range in error of 20–80 percent from the surface averaged value. Therefore, for the most reliable interpretation, the charge-transfer resistance may be determined from the high-frequency time constant. However, the faradaic impedance parameters A and B must be estimated with caution from the low-frequency time constant.

CHAPTER 11
CONCLUSIONS

11.1 Indirect Impedance Applied to External Post-Tensioned Tendons

Indirect impedance was shown to be capable of monitoring the corrosion activity in post-tensioned tendons. Through proof of concept experiments in which tendon sections were fabricated with one steel strand and forced to corrode, it was determined that the indirect impedance is qualitatively sensitive to the corrosion rate of the steel. Finite element models were used to simulate the indirect impedance response and determine that the resistivity of the grout contributes to the overall impedance in two ways. There is a series ohmic component associated with the current that enters the steel and there is also a parallel ohmic component representative of the current that flows parallel to the steel. Since the current distribution changes with frequency and is nonuniform throughout the grout the ohmic components must be expressed as complex variables.

A finite element model of a tendon containing one steel strand was used to gain an understanding of the components that contribute to the indirect impedance. It was shown that there is a parallel ohmic impedance component, as well as, a series ohmic impedance which fully accounts for the contribution of the grout resistivity to the impedance. The parallel ohmic impedance is much larger than the series ohmic impedance and is inductive while the series component is capacitive. If the ohmic impedances are expressed as resistors, the polarization resistance of the steel will be greatly overestimated and corrosion may go undetected. The series and parallel ohmic impedances change with steel location, resistivity of the grout, and the properties of the steel which makes it difficult to extract the interfacial impedance from the indirect impedance data.

Finite element simulations were also performed to determine how the ohmic impedance components change with variations in electrode spacing and steel polarization resistance. The results showed that when the electrodes are equally spaced apart at a distance relatively similar to the depth of the steel, frequency dispersion was minimized. Changes in the steel polarization resistance also influence the ohmic impedance components. As the polarization resistance increases and the interfacial impedance is more capacitive, the series ohmic impedance becomes more inductive. The parallel ohmic impedance is inductive for all polarization resistances but increases in magnitude as the polarization resistance increases.

Experiments performed on tendons with multiple steel strands including a tendon extracted from the Ringling bridge as well as tendons on the mock bridge section at Texas A&M brought up some challenges. Specifically, it was shown that corrosion could go undetected if it is not present directly under the working or counter electrodes. For example, if there are 10 steel strands and one of the strands in the center of the tendon is corroding, it would be extremely difficult to detect this from the indirect impedance measurement. Therefore, any adoption of indirect impedance as a suitable corrosion detection technique would require multiple measurements at multiple locations.

11.2 Influence of Surface Heterogeneity in Impedance Measurements

The presence of frequency dispersion in the form of a Constant Phase Element in impedance measurements has for a long time been attributed to variation of the impedance along the surface of the electrode. Finite element simulations on a disk electrode show that frequency dispersion occurs at frequencies greater than a characteristic frequency which is inversely related to the characteristic length of the disk, r_0. If the disk surface is rough the characteristic length becomes $f_r r_0$ and there is also a characteristic length associated with the roughness itself, which is $f_r^2 P$. The frequency dispersion associated with the roughness will only occur at lower frequencies than the influence of the disk geometry if $\ell_{c,rough} > \ell_{c,roughdisk}$. This will only occur for large roughness factors such as in the case of porous electrodes. Therefore, roughness cannot be used as a physical explanation of CPE behavior. The transition from a rough electrode to a porous electrode was shown through impedance simulations and the characteristic length used to describe roughness was also applicable to porous electrodes.

Brug[12] attributed the CPE response to a surface distribution of capacitance and used the parameters of the CPE to derive an expression for an effective capacitance. Finite element simulations for a disk electrode incorporating a periodic variation of capacitance along the radial axis showed that there is also a characteristic dimension associated with this form of heterogeneity which is the period, P, of the distribution. Therefore, a distribution of capacitance can not be a physical explanation of CPE behavior.

Similar simulations performed with a distribution of charge-transfer resistance for a single step reaction did not yield frequency dispersion. However, when the reaction mechanism was set to a two-step reaction coupled by an adsorbed intermediate, frequency dispersion occurred at high frequencies associated with the R_tC_0 time constant, as well as, at low frequencies associated with the faradaic impedance. This form of surface distribution was not dependent on a characteristic length but instead on the parameters of the faradaic impedance. The frequency dispersion at low frequency hinders the ability to extract physically significant parameters from the impedance. However, the use of small electrodes will minimize the influence of the heterogeneity.

CHAPTER 12
SUGGESTIONS FOR FUTURE WORK

While a full understanding of the components which contribute to the indirect impedance measurement has been achieved, it has not been clear how the corrosion rate of the steel may be estimated. Future work should be performed to develop ways of estimating, at least, the limits of the series and parallel ohmic impedances based on grout to steel volume ratio, relative position of steel strands, and the grout resistivity. If this can be achieved, the polarization resistance of the steel can be estimated.

The physical meaning of a CPE that is not associated with a normal distribution of time constants still eludes us. Future work should focus on understanding the influence of coupled faradaic and charging currents. A finite element model analysis of the influence of coupled charging and faradaic currents is presented by Wu et al. [77] on the impedance response of rotating disk electrodes. The analysis required the use of a simplified model of the double layer capacitance which was based on the Gouy-Chapman-Stern model. Ion-specific adsorption was neglected. The simulations performed showed that the coupling of charging and faradaic currents for a rotating disk electrode induce frequency dispersion in the high-frequency loop associated with the faradaic and charging processes. However, the rate constant used in her work were too large.

Preliminary finite element simulations for a rotating disk electrode were performed for two systems including the redox couple ferro/ferricyanide

$$\mathrm{Fe(CN)}_6^{4-} \leftrightharpoons \mathrm{Fe(CN)}_6^{3-} + (e)^- \tag{12–1}$$

and the silver redox couple,

$$\mathrm{Ag} \leftrightharpoons \mathrm{Ag}^+ + (e)^- \tag{12–2}$$

respectively. The solutions used in the simulations were 0.1 M $K_3Fe(CN)_6$ and 0.1 M $K_4Fe(CN)_6$ with a supporting electrolyte of 1M KCl. For the silver case, a 0.1M $AgNO_3$ with a supporting electrolyte of KNO_3 was considered.

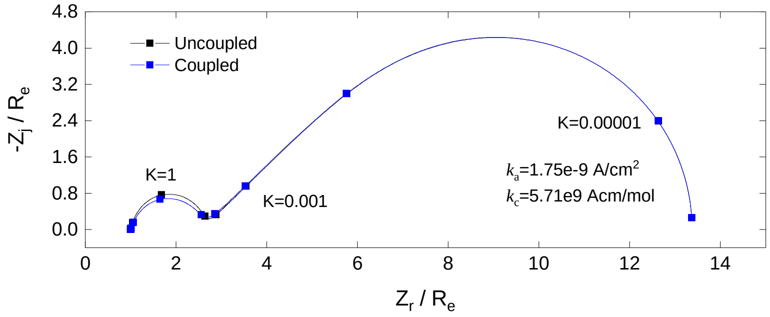

Figure 12-1. The simulated global impedance of a rotating disk electrode with a silver redox couple with and without coupled charging and faradaic currents. The rate constants of $k_a = 1.75 \times 10^{-9}$ A/cm^2 and $k_c = 5.71 \times 10^{9}$ Acm/mol were used.

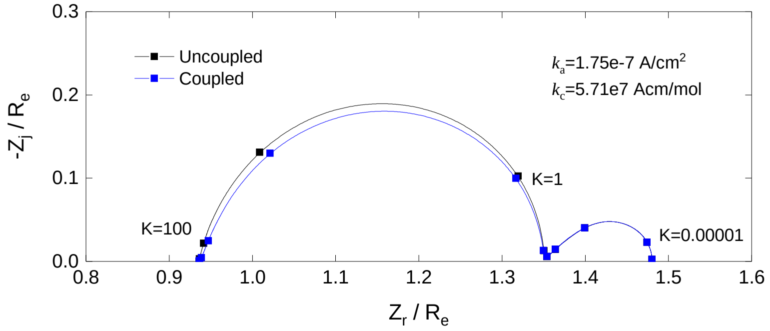

Figure 12-2. The simulated global impedance of a rotating disk electrode with a silver redox couple with and without coupled charging and faradaic currents. The rate constants of $k_a = 1.75 \times 10^{-7}$ A/cm^2 and $k_c = 5.71 \times 10^{7}$ Acm/mol were used.

The simulated global impedance for the silver case is shown in Figure 12-1 which compares the coupled and uncoupled cases of faradaic and charging currents for $k_a = 1.75 \times 10^{-9}$ A/cm^2 and $k_c = 5.71 \times 10^{9}$ Acm/mol. The coupling of charging and faradaic currents caused depression of the high frequency semi-circle.

Changing the rate constants to increase the size of the high-frequency loop, makes the frequency dispersion more visible. The simulated global impedance for rate constants $k_a = 1.75 \times 10^{-7}$ A/cm^2 and $k_c = 5.71 \times 10^{7}$ Acm/mol is shown in Figure 12-2. The frequency dispersion was still confined to the high frequency loop.

Similar simulations were performed for the ferro/ferricyanide case. The simulated global impedance is shown in Figure 12-3. In this case, the difference between the

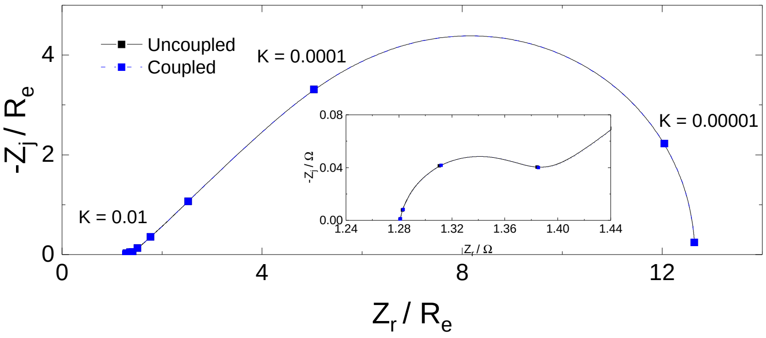

Figure 12-3. The simulated global impedance of a rotating disk electrode with a silver redox couple with and without coupled charging and faradaic currents. The rate constants of $k_a = 3.4$ Acm/mol and $k_c = 2.64 \times 10^4$ Acm/mol were used.

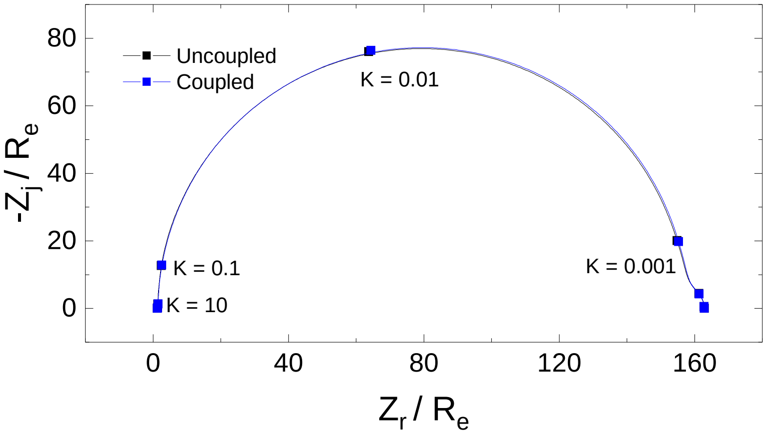

Figure 12-4. The simulated global impedance of a rotating disk electrode with a silver redox couple with and without coupled charging and faradaic currents. The rate constants of $k_a = 3 \times 10^{-5}$ Acm/mol and $k_c = 0.01$ Acm/mol were used.

coupled and the uncoupled cases is negligible. With larger rate constants, the effect is still very small as shown in Figure 12-4. Future work should be done to explore why coupled currents in the silver redox couple case induced frequency dispersion while it did not for the ferro/ferricyanide case. It may be useful to compare the components of oscillating current density for both the coupled and uncoupled cases. For example, the magnitude of the oscillating current density is shown in Figure 12-5 as a function of dimensionless frequency for the silver redox system. The total oscillating current density is shown as well as the faradaic and charging components for both the coupled and uncoupled cases. The faradaic current for the coupled case is much larger than the uncoupled case

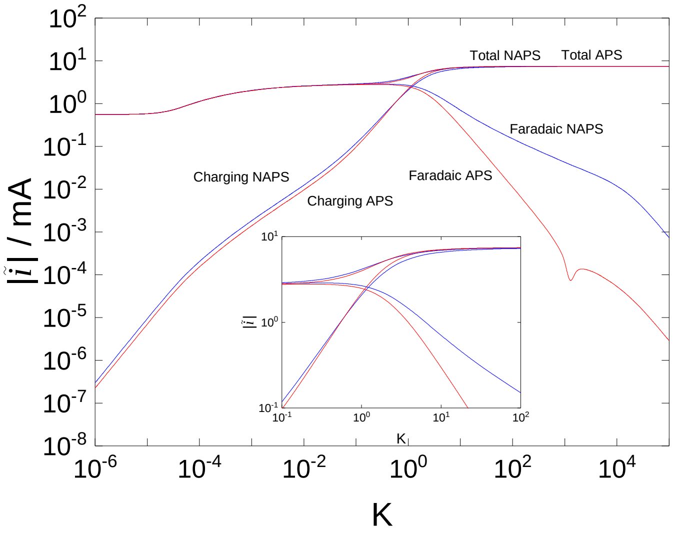

Figure 12-5. The magnitude of the oscillating current density obtained from the silver redox simulations as a function of dimensionless frequency for coupled and uncoupled cases. Also shown are the faradaic and charging components of the current density.

at high frequencies, while the charging current is only slightly larger in the coupled case than the uncoupled case at low frequencies. The figure inset shows a magnified view of the transition zone where the total current switches from faradaic controlled to charging controlled. There is a clear difference within the transition zone between the coupled and uncoupled cases. The magnitude of the oscillating current density for the ferro/ferricyanide simulation is shown in Figure 12-6 as a function of dimensionless frequency. In this case, despite the differences in the coupled and uncoupled charging and faradic currents at high and low frequencies, the total current of the coupled case matches the total current of the uncoupled case at all frequencies. A more in-depth analysis should be done to uncover the factors that contribute to both of these scenarios.

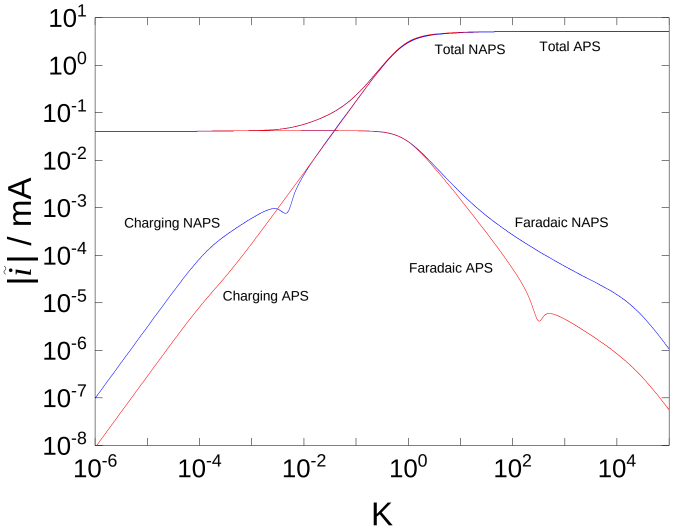

Figure 12-6. The magnitude of the oscillating current density obtained from the silver redox simulations as a function of dimensionless frequency for coupled and uncoupled cases. Also shown are the faradaic and charging components of the current density.

REFERENCES

[1] "Durable Post-tensioned Concrete Structures." Tech. Rep. 47, The Concrete Society, 1996.

[2] A. A. Sags, R. H. Hoehne, S.C. Kranc. "Initial Development of Methods for Assessing Condition of Post-tensioned Tendons of Segmental Bridges." Tech. rep., University of South Florida, 2000.

[3] Agarwal, Pankaj, Orazem, M. E., and García-Rubio, L. H. "Measurement Models for Electrochemical Impedance Spectroscopy: I. Demonstration of Applicability." *Journal of the Electrochemical Society* 139 (1992).7: 1917–1927.

[4] Alexander, Christopher L., Tribollet, Bernard, and Orazem, Mark E. "Contribution of Surface Distributions to Constant-Phase-Element (CPE) Behavior: 1. Influence of Roughness." *Electrochimica Acta* 173 (2015): 416–424.

[5] ———. "Contribution of Surface Distributions to Constant-Phase-Element (CPE) Behavior: 2. Capacitance." *Electrochimica Acta* (2015): submitted.

[6] ———. "Contribution of Surface Distributions to Constant-Phase-Element (CPE) Behavior: 2. Reactivity." *Electrochimica Acta* (2015): in preparation.

[7] Andrade, C. and Martinez, I. "Metal Corrosion Rate Determination of Different Solutions and Reinforced Concrete Specimens by Means of a Noncontacting Corrosion Method." *Nanostructured Materials and Nanotechnology Ii* 66 (2010).5: 056001–1–056001–10.

[8] Andrade, C., Martnez, I., and Castellote, M. "Feasibility of determining corrosion rates by means of stray current-induced polarisation." *Journal of Applied Electrochemistry* 38 (2008): 1467–1476.

[9] Andrade, C, Sanchez, J, Martinez, I, and Rebolledo, Nuria. "Analogue Circuit of the Inductive Polarization Resistance." *Electrochimica Acta* 56 (2011).4: 1874–1880.

[10] Blanc, C., Orazem, M.E., Pbre, N., Tribollet, B., Vivier, V., and Wu, S. "The Origin of the Complex Character of the Ohmic Impedance." *Electrochimica Acta* 55 (2010): 6313–6321.

[11] Borisova, T. and Ershler, B. "Determination of the Zero Voltage Points of Solid Metals from Measurements of the Capacity of the Double Layer." *Zhurnal Fizicheskoi Khimii* 24 (1950): 337–344.

[12] Brug, G. J., van den Eeden, A. L. G., Sluyters-Rehbach, M., and Sluyters, J. H. "The Analysis of Electrode Impedances Complicated by the Presence of a Constant Phase Element." *Journal of Electroanalytical Chemistry* 176 (1984): 275–295.

[13] Cederquist, Sally Cole. "Motor Speedway Bridge Collapse Caused by Corrosion." *Materials Performance* 39 (2000).7: 18–19.

[14] Chen, Yu-Min, Alexander, Christopher L, Cleveland, Christopher, and Orazem, Mark E. "Influence of Geometry-Induced Frequency Dispersion on the Impedance of Ring Electrodes." *Electrochimica Acta* (2017).

[15] Córdoba-Torres, P., Mesquita, T. J., Devos, O., Tribollet, B., Roche, V., and Nogueira, R. P. "On the Intrinsic Coupling between Constant-Phase Element Parameters α and Q in Electrochemical Impedance Spectroscopy." *Electrochimica Acta* 72 (2012): 172–178.

[16] Córdoba-Torres, Pedro, Mesquita, Thiago J., and Nogueira, Ricardo P. "Relationship between the Origin of Constant-Phase Element Behavior in Electrochemical Impedance Spectroscopy and Electrode Surface Structure." *The Journal of Physical Chemistry C* 119 (2015): 4136–4147.

[17] Corven, J. "Mid-Bay bridge post-tensioning evaluation." Tech. rep., Florida Department of Transportation, 2001.

[18] de Levie, R. "On Porous Electrodes in Electrolyte Solutions. IV." *Electrochimica Acta* 9 (1964).9: 1231–1245.

[19] de Levie, Robert. "Electrochemical Responses of Porous and Rough Electrodes." *Advances in Electrochemistry and Electrochemical Engineering*. ed. Paul Delahay, vol. 6. New York: Interscience, 1967. 329–397.

[20] Emmanuel, Bosco. "Computation of AC responses of Arbitrary Electrode Geometries from the Corresponding Secondary Current Distributions: A Method based on Analytic Continuation." *Journal of Electroanalytical Chemistry* 605 (2007): 89–97.

[21] Fong, C. F. Chan Man, Kee, D. De, and Kalomi, P. N. *Advanced Mathematics for Applied and Pure Sciences*. Amsterdam, The Netherlands: Gordon and Breach Science Publishers, 1997.

[22] Fricke, H. "The Theory of Electrolytic Polarization." *Philosophical Magazine* 14 (1932): 310–318.

[23] Ghorbanpoor, A. "Magnetic-Based NDE of Prestressed and Post-Tensioned Concrete MembersThe MFL System." Tech. rep., Univeristy of Wisconsin-Milwaukee, 2000.

[24] Hirschorn, Bryan, Orazem, Mark E., Tribollet, Bernard, Vivier, Vincent, Frateur, Isabelle, and Musiani, Marco. "Constant-Phase-Element Behavior Caused by Resistivity Distributions in Films: 1. Theory." *Journal of the Electrochemical Society* 157 (2010): C452–C457.

[25] ———. "Constant-Phase-Element Behavior Caused by Resistivity Distributions in Films: 2. Applications." *Journal of the Electrochemical Society* 157 (2010): C458–C463.

[26] ———. "Determination of Effective Capacitance and Film Thickness from CPE Parameters." *Electrochimica Acta* 55 (2010): 6218–6227.

[27] Huang, Vicky Mei-Wen, Vivier, Vincent, Orazem, Mark E., Pébère, Nadine, and Tribollet, Bernard. "The Apparent CPE Behavior of a Disk Electrode with Faradaic Reactions." *Journal of the Electrochemical Society* 154 (2007): C99–C107.

[28] ———. "The Apparent CPE Behavior of an Ideally Polarized Disk Electrode: A Global and Local Impedance Analysis." *Journal of the Electrochemical Society* 154 (2007): C81–C88.

[29] Jänsch, Thomas, Wallauer, Jens, and Roling, Bernhard. "Influence of Electrode Roughness on Double Layer Formation in Ionic Liquids." *The Journal of Physical Chemistry C* 119 (2015): 4620–4626.

[30] Jorcin, Jean-Baptiste, Orazem, Mark E., Pébère, Nadine, and Tribollet, Bernard. "CPE Analysis by Local Electrochemical Impedance Spectroscopy." *Electrochimica Acta* 51 (2006): 1473–1479.

[31] Kant, Rama, Kumar, Rajesh, and Yadav, Vivek K. "Theory of Anomalous Diffusion Impedance of Realistic Fractal Electrode." *Journal of Physical Chemistry C* 112 (2008): 4019 – 4023.

[32] Kant, Rama and Rangarajan, S.K. "Diffusion to Rough Interfaces: Finite Charge Transfer Rates." *Journal of Electroanalytical Chemistry* 396 (1995): 285–301.

[33] Keddam, M., Nóvoa, X. R., and Vivier, V. "The Concept of Floating Electrode for Contact-Less Electrochemical Measurements: Application to Reinforcing Steel-Bar Corrosion in Concrete." *Corrosion Science* 51 (2009): 17951801.

[34] Kelman, R.B. "Steady-State Diffusion Through a Finite Pore into an Infinite Reservoir: An Exact Solution." *The Bulletin of Mathematical Biophysics* 27 (1965).1: 57–65.

[35] Kerner, Zsolt and Pajkossy, Tamas. "Impedance of Rough Capacitive Electrodes: The Role of Surface Disorder." *Journal of Electroanalytical Chemistry* 448 (1998): 139–142.

[36] Kumar, Rajesh and Kant, Rama. "Generalized Warburg Impedance on Realistic Self-Affine Fractals: Comparative Study of Statistically Corrugated and Isotropic Roughness." *Journal of Chemical Sciences* 121 (2009): 579 – 588.

[37] ———. "Theory of Generalized Gerischer Admittance of Realistic Fractal Electrode." *Journal of Physical Chemistry C* 113 (2009): 19558 – 19567.

[38] ———. "Admittance of Diffusion Limited Adsorption Coupled to Reversible Charge Transfer on Rough and Finite Fractal Electrodes." *Electrochimica Acta* 95 (2013): 275 – 287.

[39] Kurtyka, Bogdan and de Levie, Robert. "Frequency dispersion associated with a non-homogeneous interfacial capacitance." *Journal of Electroanalytical Chemistry* 322 (1992).1: 63–77.

[40] Lasia, Andrzej. "Impedance of Porous Electrodes." *Journal of Electroanalytical Chemistry* 397 (1995): 27–33.

[41] Leek, Ralph and Hampson, Noel A. "The dispersion of double-layer capacitance with frequency I. Smooth solid electrodes." *Surface Technology* 7 (1978).2: 151–155.

[42] Lewis, A. "A Moratorium Lifted." *Concrete* 30 (1996).6: 25–27.

[43] Mandelbrot, Benoit B. *The Fractal Geometry of Nature.* Freeman, San Franscisco, 1982.

[44] Martin, J., Broughton, K.J., Giannopolous, A., Hardy, M.S.A., and Forde, M.C. "Ultrasonic tomography of grouted duct post-tensioned reinforced concrete bridge beams." *NDT&E International* 34 (2001): 107–103.

[45] Mehaute, A. Le and Crepy, G. "Introduction to Transfer and Motion in Fractal Media: The Geometry of Kinetics." *Solid State Ionics* 9 (1983): 17–30.

[46] Minchin Jr, R Edward. "Identification and Demonstration of a Technology Adaptable to Locating Water in Post-tensioned Bridge Tendons." Tech. rep., 2006.

[47] Monteiro, Paulo JM and Morrison, HF. "Non-destructive Method of Determining the Position and Condition of Reinforcing Steel in Concrete." 1999. US Patent 5,855,721.

[48] Musiani, M., Orazem, M.E., Pbre, N., Tribollet, B., and Vivier, V. "Determination of Resistivity Profiles in Anti-corrosion Coatings from Constant-Phase-Element Parameters." *Progress in Organic Coatings* 77 (2014): 2076–2083.

[49] Newman, John S. "Resistance for Flow of Current to a Disk." *Journal of the Electrochemical Society* 113 (1966).5: 501–502.

[50] ———. "Frequency Dispersion in Capacity Measurements at a Disk Electrode." *Journal of the Electrochemical Society* 117 (1970): 198–203.

[51] Nguyen, Anh Son, Musiani, Marco, Orazem, Mark E., Pbre, Nadine, Tribollet, Bernard, and Vivier, Vincent. "Impedance Analysis of the Distributed Resistivity of Coatings in Dry and Wet Conditions." *Electrochimica Acta* (2015).0: In Press.

[52] Nguyen, Anh Son, Musiani, Marco, Orazem, Mark E., Pébère, Nadine, Tribollet, Bernard, and Vivier, Vincent. "Impedance Analysis of the Distributed Resistivity of Coatings in Dry and Wet Conditions." *Electrochimica Acta* (2015): in press.

[53] Nisancioglu, K. "Theoretical Problems Related to Ohmic Resistance Compensation." *The Measurement and Correction of Electrolyte Resistance in Electrochemical Tests.* eds. L. L. Scribner and S. R. Taylor, STP 1056. Philadelphia, PA: American Society for Testing and Materials, 1990, 61–77.

[54] Nisancioglu, K., Gartland, P. O., Dahl, T., and Sander, E. "Role of Surface Structure and Flow Rate on the Polarization of Cathodically Protected Steel in Seawater." *Nanostructured Materials and Nanotechnology Ii* 43 (1987): 710–718.

[55] Nyikos, L. and Pajkossy, T. "fractal Dimension and Fractional Power Frequency-Dependent Impedance Of Blocking Electrodes." *Electrochimica Acta* 30 (1985).11: 1533–1540.

[56] Orazem, Mark E., Pébère, Nadine, and Tribollet, Bernard. "Enhanced Graphical Representation of Electrochemical Impedance Data." *Journal of the Electrochemical Society* 153 (2006): B129–B136.

[57] Orazem, Mark E. and Tribollet, Bernard. *Electrochemical Impedance Spectroscopy*. Hoboken, NJ: John Wiley & Sons, 2008.

[58] Orazem, Mark E., Tribollet, Bernard, Vivier, Vincent, Marcelin, Sabrina, Pébère, Nadine, Bunge, Annette L., White, Erick A., Riemer, Douglas P., Frateur, Isabelle, and Musiani, Marco. "Interpretation of Dielectric Properties for Materials showing Constant-Phase-Element (CPE) Impedance Response." *Journal of the Electrochemical Society* 160 (2013): C215–C225.

[59] Pajkossy, T. "Impedance of Rough Capacitive Electrodes." *Journal of Electroanalytic Chemistry* 364 (1994): 111–125.

[60] Pajkossy, Tamás. "Impedance Spectroscopy at Interfaces of Metals and Aqueous Solutions - Surface Roughness, CPE and Related Issues." *Solid State Ionics* 176 (2005): 1997–2003.

[61] Pajkossy, Tamás and Nyikos, Lajos. "Impedance of planar electrodes with scale-invariant capacitance distribution." *Journal of Electroanalytical Chemistry* 332 (1992).1: 55–61.

[62] Pajkossy, Tamas, Wandlowski, Thomas, and Kolb, Dieter M. "Impedance Aspects of Anion Adsorption on Gold Single Crystal Electrodes." *Journal of Electroanalytical Chemistry* 414 (1996): 209–220.

[63] Permeh, Samanbar, Vigneshwaran, KK, and Lau, Kingsley. "Corrosion of Post-Tensioned Tendons with Deficient Grout." (2016).

[64] Proverbio, E and Bonaccorsi, LM. "Failure of Prestressing Steel Induced by Crevice Corrosion in Prestressed Concrete Structures." *Proeedings of 9th International Conference on Durability of Materials and Components*. 2002.

[65] Proverbio, G., E. /Ricciardi. "Failure of a 40 Years Old Post Tensioned Bridge near Seaside." *Eurocorr: Past Success - Future Challenges*. 2000.

[66] Rodney G. Powers, Yash Paul Virman, Alberto A. Sags. "Corrosion of Post-tensioned Tendons in Florida Bridges." Tech. rep., Florida Department of Transportation, 1999.

[67] Singh, Maibam Birla and Kant, Rama. “Debye-Falkenhagen Dynamics of Electric Double Layer in Presence of Electrode Heterogeneities.” *Journal of Electroanalytical Chemistry* 704 (2013): 197 – 207.

[68] ———. “Theory of Anomalous Dynamics of Electric Double Layer at Heterogeneous and Rough Electrodes.” *J. Phys. Chem. C.* 118 (2014): 5122–5133.

[69] Song, H. K., Hwang, H. Y., Lee, K. H., and Dao, L. H. “The Effect of Pore Size Distribution on the Frequency Dispersion of Porous Electrodes.” *Electrochimica Acta* 45 (2000): 2241–2257.

[70] Srivastav, Shruti and Kant, Rama. “Anomalous warburg impedance: Influence of uncompensated solution resistance.” *Journal of Physical Chemistry C* 115 (2011): 12232 – 12242.

[71] Trassati, S. and Parsons, R. “Interphases in Systems of Conducting Phases.” *Pure and Applied Chemistry* 58 (1986): 437–454.

[72] Virmani, Paul Y. “Literature Review of Chloride Threshold Values for Grouted Post-Tensioned Tendons.” Tech. rep., Federal Highway Administration, 2012.

[73] West, Alan C. and Newman, John S. “Current Distributions on Recessed Electrodes.” *Journal of the Electrochemical Society* 138 (1991).6: 1620–1625.

[74] White, Erick A., Orazem, Mark E., and Bunge, Annette L. “Characterization of Damaged Skin by Impedance Spectroscopy: Chemical Damage by Dimethyl Sulfoxide.” *Pharmaceutical Research* 30 (2013): 2607–2624.

[75] Wiliam H. Hartt, Siva Venugopalan. “Corrosion Evaluation of Post-Tensioned Tendosn on the Mid Bay Bridge in Destin, Florida.” *FDOT* 1 (2002): 995–1006.

[76] Woodward, RJ and Williams, FW. “Collapse of Yns-Y-gwas Bridge,.” *Proceedings of the Institution of Civil Engineers* 84 (1988).4: 635–669.

[77] Wu, Shao-Ling, Orazem, Mark E., Tribollet, Bernard, and Vivier, Vincent. “The Influence of Coupled Faradaic and Charging Currents on Impedance Spectroscopy.” *Electrochimica Acta* 131 (2014): 3–12.

BIOGRAPHICAL SKETCH

Christopher Alexander graduated from the University of South Florida with a BS in Civil Engineering in 2010. During his time there he led a group of undergraduate researchers, worked directly with the president as an official student representative, and tutored students in math. He obtained a master's degree in Civil Engineering from the University of Florida in 2013 and a PhD in Chemical Engineering under Mark Orazem, a Distinguished Professor and expert on electrochemical engineering and impedance spectroscopy. His research was primarily focused on developing a device that can non-destructively detect corrosion in bridge tendons using Electrochemical Impedance Spectroscopy. He worked on several side projects including assessing the role of surface heterogeneity on impedance spectroscopy, simulating the impedance response of a continuous glucose monitor for diabetes patients, and determining the influence of coupled charging and faradic current on impedance spectroscopy. His work on the influence of surface heterogeneity was recognized as a novel contribution to the field and was published in a special issue of Electrochmica Acta.